Reviewed Preprint
v1 • December 22, 2025
Not revised

Reviewed Preprint
v2 • June 22, 2026
Revised by authors

For correspondence:
shigeo.okabe@riken.jp

Competing interests: No competing interests declared

Funding: See page 35

Reviewing editor: Jason P Lerch, University of Oxford, United Kingdom

Decoding spine nanostructure in cultured neurons derived from mouse models of mental disorder reveals a schizophrenia-linked role for Ecrg4

Yutaro Kashiwagi[1], Qingrui Liu[1], Yasuhiro Go[2,3,4], Ryo Saito[5], Atsu Aiba[5], Takanobu Nakazawa[6], Shigeo Okabe[1,7]

[1]Department of Cellular Neurobiology, Graduate School of Medicine, University of Tokyo, Tokyo, Japan • [2]Graduate School of Information Science, University of Hyogo, Kobe, Japan • [3]National Institute for Physiological Sciences (NIPS), National Institutes of Natural Sciences, Okazaki, Japan • [4]Exploratory Research Center on Life and Living Systems (ExCELLS), National Institutes of Natural Sciences, Okazaki, Japan • [5]Laboratory of Animal Resources, Center for Disease Biology and Integrated Medicine, Graduate School of Medicine, the University of Tokyo, Tokyo, Japan • [6]Department of Bioscience, Faculty of Life Sciences, Tokyo University of Agriculture, Tokyo, Japan • [7]Laboratory for Imaging Neural Dynamics, RIKEN Center for Brain Science, Saitama, Japan

eLife Assessment

By investigating spine nanostructure and dynamics across multiple genetic mouse models for neurodevelopmental disorders, this **important** study has the potential to uncover convergent or divergent synaptic phenotypes that may be specifically associated with autism versus schizophrenia risk. The imaging and overall breadth of the methods are **convincing**. The purely in vitro nature of the study slightly limits the generalisability of the findings.

https://doi.org/10.7554/eLife.109083.2.sa3

Abstract

Dendritic spine dysfunction may contribute to the etiology and symptom expression of neuropsychiatric disorders. The intimate relationship between spine morphology and function suggests that decoding disease-related abnormalities from spine morphology can aid in developing synapse-targeted interventions. Here, we describe a population analysis of dendritic spine nanostructure applied to the objective grouping of multiple mouse models of neuropsychiatric disorders. This method has identified two major groups of spine phenotypes linked to schizophrenia and autism spectrum disorder (ASD). An increase in spine subpopulation with small volumes characterized the spines of schizophrenia-associated mouse models, whereas a spine subset with large volumes increased in ASD models. Schizophrenia-associated mouse models showed higher similarity in spine morphology, driven by reduced size and growth of nascent spines. The expression of Ecrg4, a gene encoding small secretory peptides, was increased in schizophrenia-associated mouse models, and functional studies confirmed its critical involvement in impaired spine dynamics and shape. These results suggest that population-level spine analysis provides rich insights into heterogeneous spine pathology, facilitating the identification of new molecular targets related to core synaptic dysfunction.

Introduction

Information processing in the neocortex and hippocampus relies on fast excitatory synaptic transmission between pyramidal neurons. Many excitatory synapses that release glutamate project onto tiny structures protruding from dendritic shafts termed spines, and the morphological properties of these spines strongly influence synaptic transmission and function, including the activity-dependent synaptic plasticity implicated in learning and memory[1,2]. In general, larger spines contain a greater number of glutamate receptors and are functionally stronger[3]. The morphological parameters defining spine shape, such as length, radius, and volume, are also highly dynamic. For instance, small nascent spines can be enlarged by high-frequency stimuli, inducing long-term potentiation (LTP) of synaptic transmission[4,5]; alternatively, spine volume can be reduced by low-frequency stimuli that induce long-term depression (LTD)[5,6]. Due to these dynamic changes, spines on pyramidal neurons exhibit substantial morphological variation, even within the same dendritic branch. In addition to direct synaptic activation inducing LTP or LTD, spine morphology can be altered by cyclical hormonal changes, neuromodulators, and various activity-independent processes[7–10]. In turn, these changes in spine morphology are associated with marked changes in neural function and behavior.

Recent advances in super-resolution microscopy have provided new opportunities for the study of spine structural diversity and dynamics. An investigation using stimulated emission depletion (STED) imaging reported an increase in spine neck size after LTP, resulting in stronger electrical coupling between the spine head and the dendritic shaft[11]. A structured illumination microscopy (SIM) imaging study of cultured hippocampal neurons revealed expansion of the spine head convexity after LTP induction[12], and suggested that this structural transformation may increase the adhesion of presynaptic and postsynaptic membranes. SIM imaging has also been applied to record the dynamic properties of spinules[13], thin protrusions extending from existing spines that may function in secondary synapse formation. Collectively, these reports implicate spine nanostructural dynamics in multiple core synaptic properties and functions, including neurotransmission, mechanical stability, synaptogenesis, and plasticity.

Genetic mutations and variants that disrupt synaptic function are strongly implicated in the pathogenesis of neuropsychiatric disorders such as autism spectrum disorder (ASD) and schizophrenia[14–20]. Based on these genomic aberrations, numerous mouse models of ASD and schizophrenia have been established and subsequently shown to harbor abnormalities in both spine morphology and physiology[19,21–24]. Moreover, several studies have reported synaptic dysfunction in neurons differentiated from patient-derived pluripotent stem cells [25–28]. Schizophrenia and ASD share several clinical features, suggesting common genetic risk factors and etiology[29,30]. However, a diametrical model emphasizes the distinct social-cognitive properties of these two major psychiatric disorders[31,32]. Both ASD and schizophrenia also show highly heterogeneous clinical phenotypes, potentially stemming from distinct pathogenic processes within disease categories. Therefore, in addition to clinical features, comparative biological phenotyping of multiple ASD and schizophrenia models may reveal shared as well as disease-specific pathogenic processes.

Genetic studies on ASD and schizophrenia have identified copy-number variants and protein-disrupting single-nucleotide variants that confer higher disease risk, and mouse models harboring these genetic abnormalities frequently exhibit behavioral and neurological features resembling those of the clinical conditions (termed endophenotypes)[19,33]. However, only a limited number of studies objectively compare phenotypes related to synaptic structure and function across disease models. An *in vivo* two-photon imaging study reported accelerated spine turnover in three genetically distinct mouse models of ASD[34]. Also, multiple mouse models of ASD were found to exhibit a similar imbalance in the activity of excitatory and inhibitory neurons[35]. These studies support the idea that distinct genetic mutations may induce similar synaptic and circuit phenotypes in ASD-associated mouse models. However, differences in synaptic properties between ASD and schizophrenia have not yet been comprehensively examined.

In this study, we developed an objective method for identifying population-level differences in spine nanostructure. This method, which has been applied to multiple mouse models of psychiatric disorders, identified two distinct groups corresponding to ASD and schizophrenia. An increase in a specific spine subpopulation with small volumes characterized the spines of mouse models of schizophrenia. In turn, ASD-related mouse models showed an opposite spine phenotype. The schizophrenia-related phenotype was associated with reduced size and growth of nascent spines and enhanced spine turnover. Further gene expression analysis identified the overexpression of Ecrg4, a gene encoding a precursor of hormone-like peptides, as a candidate mediator of this schizophrenia-associated spine phenotype. Population-level analysis of spine nanostructures is a powerful approach for understanding heterogeneous synaptic impairments in psychiatric disorders.

Results

Spine nanostructure imaging and generation of the spine density plot

We have designed a method for objectively comparing spine properties among multiple mouse models of psychiatric disorders at the population level using SIM imaging. Previous results demonstrated that high-resolution SIM images of dendritic spines in cultured hippocampal neurons can provide reliable information about spine size and morphological properties[12]. In the current study, the analytical procedures for SIM images were further improved for quantitative comparisons. Three-dimensional SIM images of dendritic spines were captured in DiI-stained cultured neurons derived from control and disease-model mouse hippocampus (Figure 1A). This staining procedure provided a better image quality than fluorescent protein-based labeling because of the higher fluorescence signal from the plasma membrane. SIM images were processed using custom-made scripts to identify and segment the individual dendritic spines (Figure 1B–D). We previously reported a set of scripts designed to isolate dendritic spines automatically[12]. However, the segmentation accuracy still necessitated manual inspection. In the newly developed scripts, we introduced a step to readjust the spine–shaft boundary, enabling fully automated measurement of multiple morphological parameters, including length, surface area, and volume. In addition, the isolated spines were further divided into 160-nm-thick longitudinal segments, yielding a total of 64 shape descriptors.

Spine shape parameters measured by conventional methods are difficult to compare directly when images are obtained from multiple independent experiments. This problem is caused by several factors, but the main factors are variability in image intensity, signal-to-noise ratio, and image aberration introduced by unoptimized imaging conditions. To test the stability of SIM-based spine imaging, we compared the spine size distribution across four samples prepared at time points separated by >2 months (Supplementary Figure 1). The cumulative distribution curves of the four datasets showed extensive overlap, confirming the reproducibility of the SIM-based spine shape measurements using independent culture samples.

Another technical issue in comparing spine shape is the heterogeneity of spine shapes and the absence of defined subclasses. Population-level spine analysis, therefore, requires a new strategy that enables objective comparisons of large numbers of spines with a continuum of morphologic features. We previously demonstrated that principal component analysis (PCA) was effective for comparing high-dimensional spine shape features (descriptors) in a reduced-dimensional feature space[12]. Indeed, a PCA-based dimensional reduction of a large number of spines, based on their descriptors, generated a two-dimensional plot of spine shape that closely matched conventional spine subtypes, such as thin, mushroom, and stubby (Figure 1E). To objectively compare the two spine datasets (control and disease model), we first generated plots of relative spine densities (number per area in feature space) mapped to 80 × 80 square blocks (Figure 1F), and then subtracted the corresponding plot pairs defined by genotype (control vs. mutant) or culture conditions. The resulting subtracted density plots contain comprehensive information about the

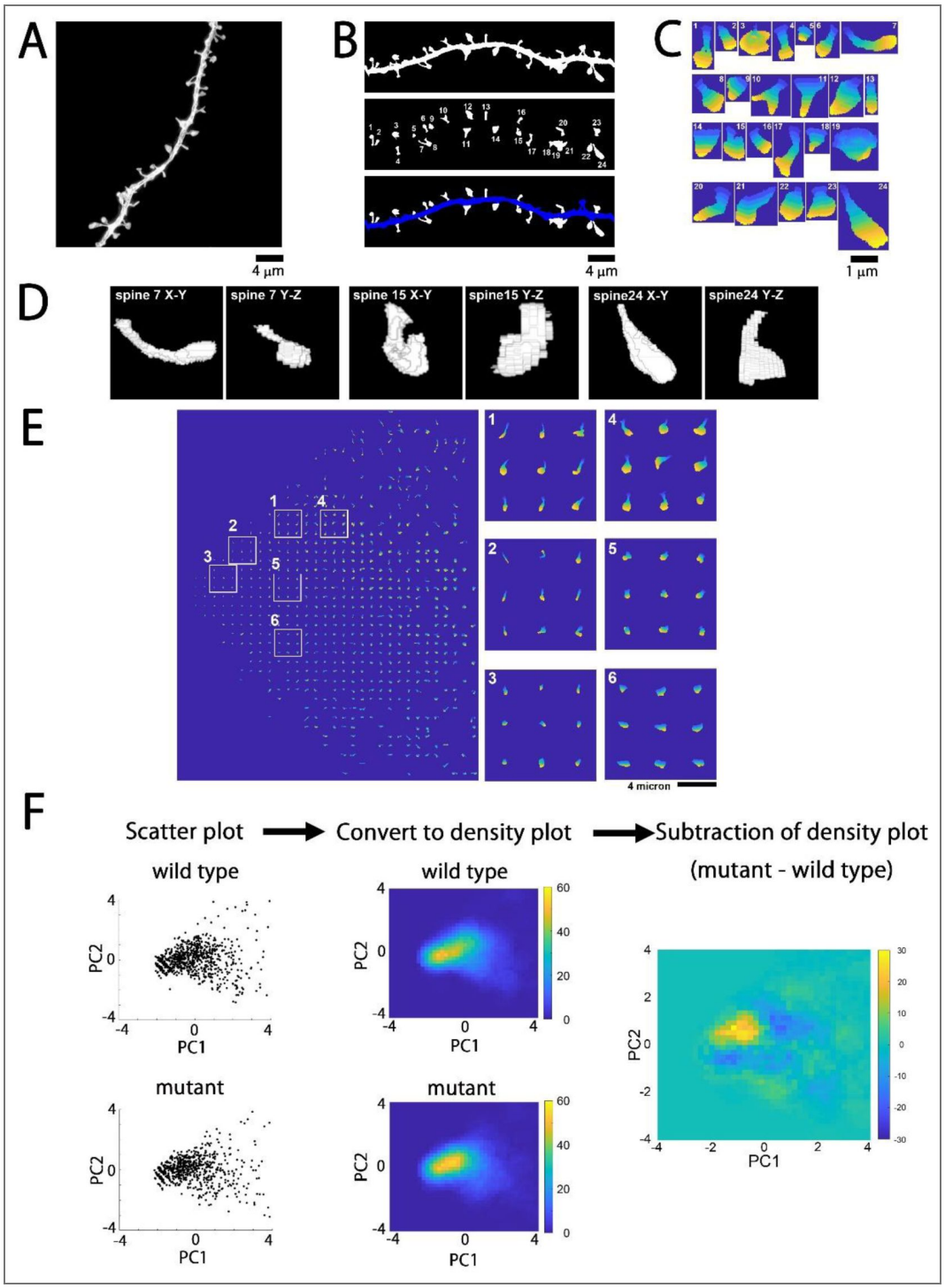

Figure 1. SIM imaging of dendritic spines, automated measurements of spine morphology, and generation of subtracted spine density plots for population-level analysis.

(A) Original SIM image of a dendritic shaft stained with lipophilic membrane dye DiI. (B) Binarized image of the same dendrite (top) and segmented spines numbered from 1 to 24 (middle). The bottom image shows segmented spines (white) and the dendritic shaft (blue). (C) Enlarged images of the individual spines shown in (B). The pseudocolor images indicating the relative positions of the spine segments from the base (blue) to the tip (yellow). (D) 3D views of three spines (No. 7, 15, and 24) viewed from different angles. (E) Principal component analysis (PCA)-based dimensional reduction of spine characteristics plotted in the plane of principal components (PC)1 and PC2. (F) Process of generating a subtracted density plot. The scatter plot of spine distribution in the PC1–PC2 plane based on morphological parameters was converted into a density plot for each culture source (genotype or treatment group), and the corresponding plots were subtracted to reveal differences in spine morphology at the population level. Bars, 4 µm for A, B, and E, 1 µm for C.

differences in relative spine numbers with similar shape properties. As expected, there was some variation in the density plot patterns across experiments. However, subtracting the distributional data from wild-type and mutant samples effectively canceled out these differences.

Moreover, the difference between the two wild-type samples was generally smaller than that between wild-type and mutant samples.

Comparison and grouping of multiple mouse models based on morphological spine similarity

The subtracted density plots contain rich information about the population-level differences in spine shape between samples. Therefore, the generation and comparison of the plots for both ASD- and schizophrenia-associated mouse models will be useful for their unbiased grouping. We selected the following eight representative mouse models harboring either copy-number variation or single gene mutations associated with psychiatric disorders: male hemizygous or female homozygous mutant mice for neuroligin-3 R451C mutation (Nlgn3$^{R451C/(y\ or\ R451C)}$)[36,37], heterozygous Syngap1 mutant mice (Syngap1$^{+/-}$)[38], heterozygous POGZ mutant mice (POGZ$^{Q1038R/+}$)[39], mice paternal duplication of chromosome 7C (15q11-13$^{dup/+}$) corresponding to human 15q11-13 duplication[40], mice with heterozygous deletion of chromosome 16B2,3 (3q29$^{del/+}$) corresponding to human 3q29 deletion[41], mice heterozygous for deletion on chromosome 16qA13 (22q11.2$^{del/+}$) corresponding to 1.5 Mb deletion on human 22q11.2[42], mice heterozygous for Setd1a mutation (Setd1a$^{+/-}$)[43], and Ca^{2+}/calmodulin-dependent protein kinase IIα kinase-dead mutant mice (CaMKIIα$^{K42R/K42R}$)[44]. Previous studies on these mouse models confirmed the presence of multiple sensory, memory, and social endophenotypes of psychiatric disorders compared to controls. Of these, Nlgn3$^{R451C/(y\ or\ R451C)}$, POGZ$^{Q1038R/+}$, and 15q11-13$^{dup/+}$ models mimic genetic variations found in ASD. Human mutations in the SYNGAP1 gene are associated with intellectual disability and autistic behaviors. The 3q29$^{del/+}$, 22q11.2$^{del/+}$, and Setd1a$^{+/-}$ models harbor genetic mutations associated with higher schizophrenia risk. CaMKII-related signaling pathway disruption has been implicated in the working memory deficits found in schizophrenia patients[45,46]. CAMK2A mutations in humans are linked to multiple mental disorders, including developmental disorders, ASD, and schizophrenia[47]. The K42R mutation of CAMK2A does not correspond to any known human genetic variant, but the CAMK2A R8H mutation is linked to schizophrenia[48]. Both R8H and K42R mutations in the N-terminal domain of CaMKIIα eliminate kinase activity; these mutations may have a similar impact on human mental disorders. Taken together, these mouse models cover a broad spectrum of human genetic aberrations associated with psychiatric disorders. Direct comparison of spine phenotypes could therefore provide important clues to underlying shared and disease-specific synaptic pathologies.

For these comparisons, we prepared three independent cultures of embryonic hippocampi from each control–mutant pair and obtained 700–1,500 3D-SIM spine images 3 weeks after plating for both mutant and control samples (Nlgn3$^{R451C/(y\ or\ R451C)}$, n = 1,134 and 1,204; Syngap1$^{+/-}$, n = 991 and 1,371; POGZ$^{Q1038R/+}$, n = 1,341 and 1,271; 15q11-13$^{dup/+}$, n = 1,208 and 1,099; 3q29$^{del/+}$, n = 1,429 and 1,408; 22q11.2$^{del/+}$, n = 1,143 and 914; Setd1a$^{+/-}$, n = 1,381 and 1,405; CaMKIIα$^{K42R/K42R}$; n = 880 and 763, control and mutant, respectively, Supplementary Table 1). Initial comparison of the cumulative frequency plots for spine length, spine surface area, and spine volume alone did not provide sufficient information to infer their structural similarity (Supplementary Figure 2), indicating that simple structural parameters are not effective in identifying disease-specific spine shape characteristics. We next generated subtracted density plots from 8 mouse models. These plots were variable, but there were certain similarities between the specific mutants (Figure 2A). We evaluated pairwise similarities by calculating the 2D cross-correlations of the subtracted density plots. The matrix of these 2D cross-correlation values yielded two major groups with high within-group similarity (Figure 2B), and this grouping was further confirmed by unbiased clustering analysis (Figure 2C). The ASD models Nlgn3$^{R451C/(y\ or\ R451C)}$, Syngap1$^{+/-}$, and POGZ$^{Q1038R/+}$ were in the first group, while the second group contained the schizophrenia models 3q29$^{del/+}$, 22q11.2$^{del/+}$, and Setd1a$^{+/-}$. This result is striking, as it indicates that information about spine shape alone can distinguish whether the culture preparation is derived from ASD- or

schizophrenia-associated mouse models. It is also of note that there were greater similarities among the schizophrenia-associated mouse models than among the ASD-associated mouse models. This finding suggests convergence in spine pathophysiology across schizophrenia-associated mouse models.

In addition to the eight mouse models of psychiatric disorders, we generated subtracted density plots for three additional conditions: immature culture samples (13 days in vitro, DIV), treatment with the AMPA subtype glutamate receptor blocker CNQX, and treatment with the $GABA_A$ receptor blocker bicuculline (Figure 2A). The subtracted density plots from the 13 DIV culture and the CNQX treatment were similar to those of schizophrenia-associated mouse models. This finding suggests that the hippocampal synapses in mouse models of schizophrenia are immature and inactive. In contrast, the subtracted density plot of the bicuculline-treated sample was distinct from that of both the schizophrenia and ASD-associated mouse models.

Distinct spine shapes between ASD- and schizophrenia-associated mouse models

The subtracted density plots provide information on the structural properties of specific spine subsets that either increased or decreased in disease mouse models. We first defined the four areas within the PC1-PC2 plane with distinct shapes: (1) small and short, (2) small and long, (3) large and short, and (4) large and long (Figure 3A and B). We also identified the wildtype-enriched area (blue areas in Figure 3C and D) and the mutant-enriched area (yellow areas in Figure 3C and D) in the same projection plane. The comparison of these two types of areas suggests that larger spines are enriched in the $Nlgn3^{R451C/(y\ or\ R451C)}$ mouse model, while small spines are enriched in the $22q11.2^{del/+}$ mouse model. Next, we calculated the normalized spine counts in the four areas for both wild-type and mutant samples and obtained the relative abundance (mutant/wild-type) for each area (Figure 3E and F). The average of three independent culture preparations confirmed the opposite trend between $Nlgn3^{R451C/(y\ or\ R451C)}$ and $22q11.2^{del/+}$.

Figure 3G-J summarizes the relative abundance of mutant spines in four areas with distinct spine shapes. We found that the relative abundance of mutant spines in area 2 (small and long spines) differed significantly between genotypes (ANOVA, $p < 0.001$). Group comparisons by Tukey's post hoc test indicate significant differences between $Nlgn3^{R451C/(y\ or\ R451C)}$ mutant and three schizophrenia-related mutants; $3q29^{del/+}$, $22q11.2^{del/+}$, and $Setd1a^{+/-}$ (Figure 3G). The opposite trend between areas 2 (small and long spines) and 3 (large and short spines) further confirms distinct spine-shape properties in ASD- and schizophrenia-related mouse models. The areas within the subtracted density plots with enriched control or mutant spines illustrate the characteristics of spine populations across mouse models (Supplementary Figures 3 and 4). The shape profiles of spines confirmed smaller spine volume of schizophrenia-related mouse models (Supplementary Figure 5).

Altered initial growth of dendritic spines in mouse models of schizophrenia

The subtracted density plots reveal common changes in the spine population across schizophrenia-associated mouse models. The mutant-spine-enriched areas also contain small, elongated spines, suggesting dysfunction in either the generation of nascent spines or the shrinkage of existing spines. To examine potential abnormalities in spine dynamics, we performed time-lapse imaging of hippocampal neuron cultures derived from two schizophrenia-associated mouse models, $22q11.2^{del/+}$ and $Setd1a^{+/-}$, and the $Nlgn3^{R451C/(y\ or\ R451C)}$ mouse model as a reference (Figure 4).

A linear mixed-effects model indicated significant effects of genotype in spine turnover rate in both $22q11.2^{del/+}$ and $Setd1a^{+/-}$ models ($F(1,25) = 5.79$, $p = 0.024$ for $22q11.2^{del/+}$ and $F(1,22) = 7.33$, $p = 0.013$ for $Setd1a^{+/-}$). In contrast, no significant effects were observed in the $Nlgn3^{R451C/(y\ or\ R451C)}$ model (Figure 5A-C). There was a significant effect of genotype in both $22q11.2^{del/+}$ and

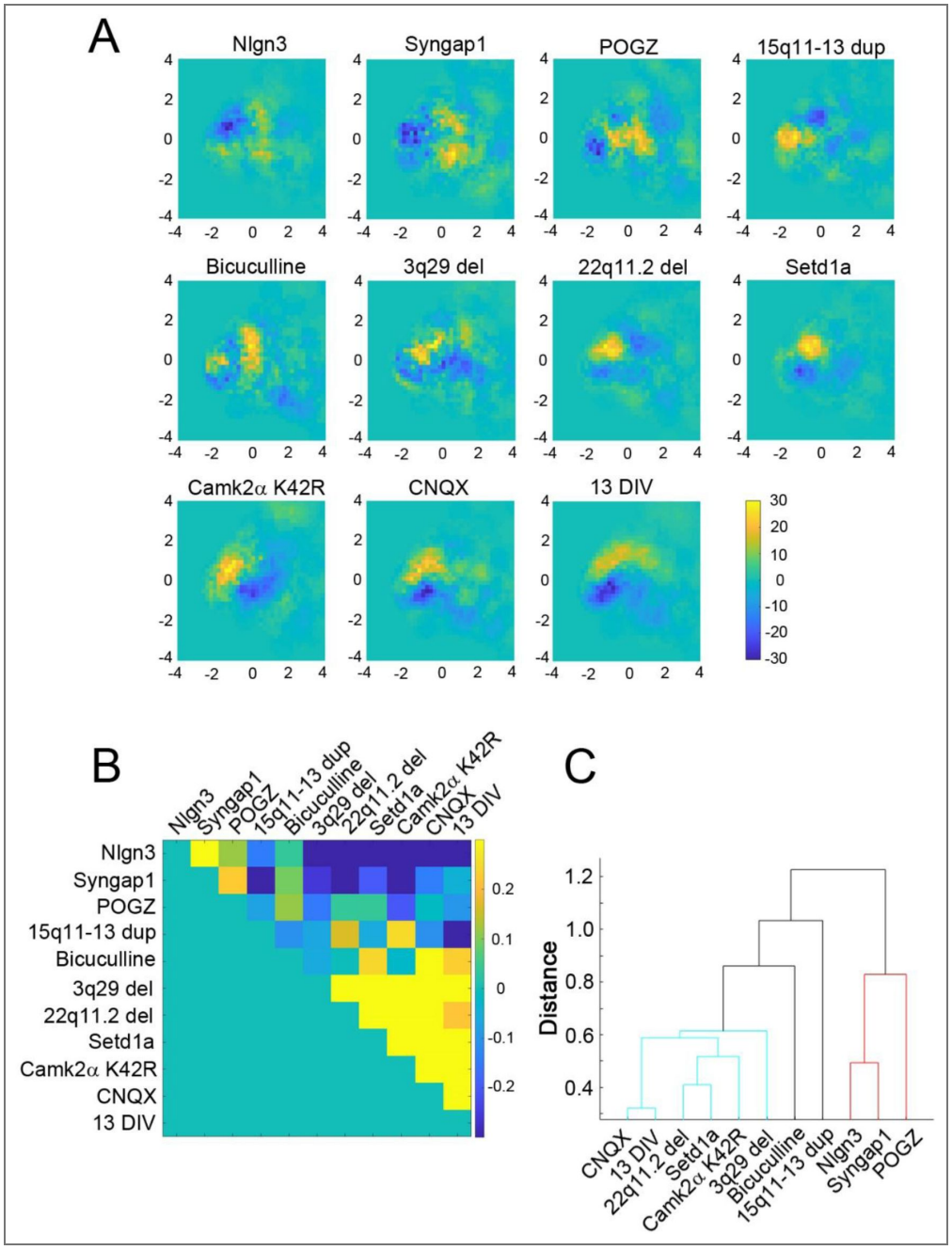

Figure 2. Spine population profiles for each model and corresponding control mouse line presented as subtracted density plots.

(A) The subtracted density plots for eight disease mouse models (Nlgn3$^{R451C/(y\ or\ R451C)}$, Syngap1$^{+/-}$, POGZ$^{Q1038R/+}$, 15q11-13$^{dup/+}$, 3q29$^{del/+}$, 22q11.2$^{del/+}$, Setd1a$^{+/-}$, and CaMKIIα$^{K42R/K42R}$) and three different culture conditions (immature culture at 13 DIV, AMPA glutamate receptor blocker CNQX treatment, and $GABA_A$ receptor blocker bicuculine treatment). The areas with a higher density of spines from mutant disease model mice are shown in yellow, and the areas with reduced density are shown in blue. The total number of spines (first number, n) analyzed from control and mutant mouse neurons and the corresponding number of dendrites (number in parentheses) are as follows: Nlgn3$^{R451C/(y\ or\ R451C)}$; n = 1,134 (58) and 1,204 (59), Syngap1$^{+/-}$; n = 991 (65) and 1,371 (83), POGZ$^{Q1038R/+}$; n = 1,341 (72) and 1,271 (72), 15q11-13$^{dup/+}$; n = 1, 208 (68) and 1,099 (63), 3q29$^{del/+}$; n = 1,429 (66) and 1,408 (66), 22q11.2$^{del/+}$; n = 1,143 (66) and 914 (63), Setd1a$^{+/-}$; n = 1,381 (71) and 1,405 (71), CaMKIIα$^{K42R/K42R}$; n = 880 (58) and 763 (54). All data are from three independent culture preparations. (B) Matrix of the 2D cross-correlations among subtracted density plots. In the lower right area, a spine group showing similar morphological changes can be identified. This group corresponded to the mouse models of schizophrenia. (C) Unbiased clustering of spine samples showing two distinct groups corresponding to schizophrenia (cyan) and ASD (red).

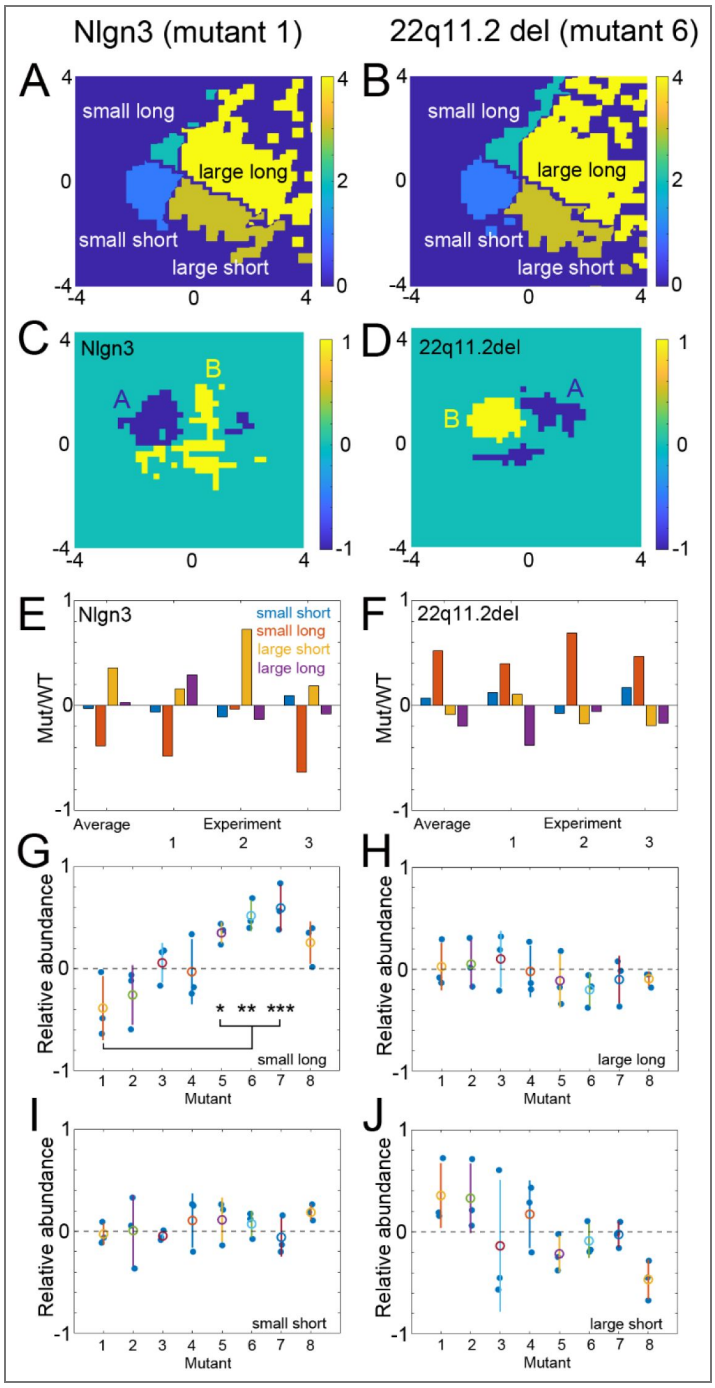

Figure 3. Distinct morphological properties of spines in cultured neurons derived from schizophrenia model mice compared with ASD model mice.

(A, C, and E) Relative enrichment of four different subgroups of spines in Nlgn3$^{R451C/(y\ or\ R451C)}$ neurons compared with wild-type neurons. In the projection plane of PC1 and PC2, four areas with distinct structural properties, namely (1) small and short, (2) small and long, (3) large and short, and (4) large and long, were defined (A). The map of areas with large differences (> 3 × SD) between control and mutant mice in spine number per area in the feature space (C) indicates that the area enriched with wild-type spines (area B, yellow region) overlaps with the area of large spines. The area enriched with the mutant spines overlaps with the area of small spines (area A, blue region). The relative enrichment of mutant spines was summarized in (E). (B, D, and F) Similar analysis of mutant spine enrichment in 22q11.2$^{del/+}$ neurons. The map of spine distribution with four different properties (B), the map of areas enriched with wild-type or mutant spines (D), and the graph of relative enrichment of mutant spines (F) show that the mutant neurons were enriched with small and long spines. (G-J) Relative abundance of the four subgroups of spines in 8 mutant mouse models (1: Nlgn3$^{R451C/(y\ or\ R451C)}$, 2: Syngap1$^{+/-}$, 3: POGZ$^{Q1038R/+}$, 4: 15q11-13$^{dup/+}$, 5: 3q29$^{del/+}$, 6: 22q11.2$^{del/+}$, 7: Setd1a$^{+/-}$, 8: CaMKIIα$^{K42R/K42R}$). Three independent culture experiments with paired wild-type and mutant samples were performed. Group comparisons were performed using one-way ANOVA followed by Tukey's post hoc test. (* $p < 0.05$, ** $p < 0.01$, *** $p < 0.005$).

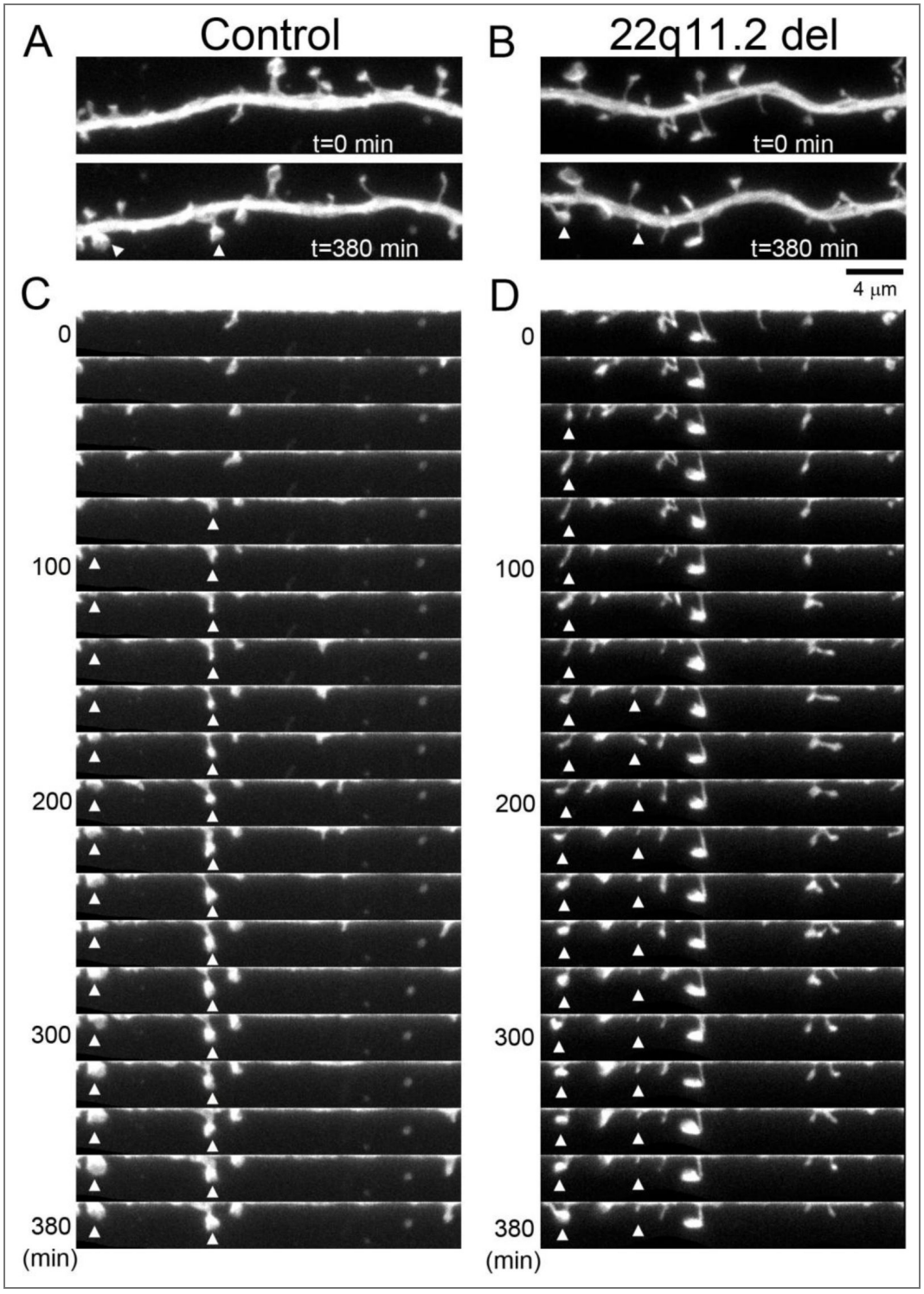

Figure 4. Time-lapse imaging of neurons derived from 22q11.2$^{del/+}$ mice and corresponding control mice.

(A and B) Images of dendritic segments from control neurons (A) and 22q11.2$^{del/+}$ neurons (B) at two different time points. (C and D) Montages of time-lapse images from control neurons (C) and 22q11.2$^{del/+}$ neurons (D). The curved dendrites were straightened, revealing newly formed spines (arrowheads) as fluorescent objects appearing at the edge of the dendritic shafts. Bar, 4 μm.

Setd1a$^{+/-}$ models also for the prolonged lifetime of transient spines (a linear mixed-effects model: 22q11.2$^{del/+}$; F(1,336)=5.33, p=0.022, Setd1a$^{+/-}$; F(1,282)=6.38, p=0.012), with no significant difference in Nlgn3$^{R451C/(y\ or\ R451C)}$ model (Figure 5D-F).

We further compared the initial increase in spine volume between genotypes (Figure 5G-I). Linear mixed-effects models incorporating nested random effects revealed significantly smaller initial spine volumes in both 22q11.2$^{del/+}$ and Setd1a$^{+/-}$models (genotype effect: $p < 0.001$ for 22q11.2$^{del/+}$ and $p < 10^{-7}$ for Setd1a$^{+/-}$). The spines in both mutants also displayed a significant reduction in spine volume increase ($p < 0.001$). In contrast, newly formed spines in the Nlgn3$^{R451C/(y\ or\ R451C)}$ neurons were significantly larger than those in wild-type neurons ($p < 10^{-4}$) with preserved time-course of spine growth.

Similar analyses of spine volume reduction before spine loss using linear mixed-effects models identified significantly smaller initial spine size in the 22q11.2$^{del/+}$ model ($p < 10^{-6}$), while no significant differences in the initial spine volume were found for the Setd1a$^{+/-}$ model (Figure 5J-L). The temporal trajectories of spine shrinkage before their loss were not significantly altered in both 22q11.2$^{del/+}$ and Setd1a$^{+/-}$ models. The Nlgn3$^{R451C/(y\ or\ R451C)}$ model showed a significantly different time-course of spine shrinkage ($p < 0.05$), while the initial spine size was not altered. Taken together, these results suggest that the smaller size of the initial spine, slower growth of nascent spines, and enhanced spine turnover contribute to the development of schizophrenia-related spine phenotypes.

To further examine the relationship between the spine growth rate and lifetime, we performed simulations using the computational model shown in Figure 6A. In this model, new spines appear randomly along the dendritic shaft according to a density-dependent probability function, then increase in volume with speed V1 (phase 1), are eliminated with probability P1 (phase 2), and are converted to stable spines upon reaching a volume threshold (phase 3). These stable spines are subsequently destabilized with low probability P2 (phase 4) and start to shrink with speed V2 (phase 5). When these shrinking spines reach a threshold, they are permanently removed. We did not incorporate the initial spine size as a model parameter because of its large variability, which made parameter optimization difficult. This model was run over 10 days of neuronal differentiation in culture (corresponding to the period of spine density increase from 8 to 17 DIV) with 625 different combinations of V1, V2, P1, and P2 to identify the combination with the best fit to the experimental data for spine turnover of 15–18 DIV neurons derived from mutants 22q11.2$^{del/+}$, Setd1a$^{+/-}$, and Nlgn3$^{R451C/(y\ or\ R451C)}$ over 24 h (Figure 6B and Supplementary Figure 6A). The best-fitted models all yielded spine lifespan distributions matching observations of the three mouse mutants (Figure 6C). The two characteristics of the spines in 22q11.2$^{del/+}$ and Setd1a$^{+/-}$ were also preserved in the best-fitted model. First, spine density in the schizophrenia-associated mouse models was lower in both the simulation and experimental data (simulation: 0.57 ± 0.029 /μm and 0.40 ± 0.027 /μm for the control and the best-fitted for schizophrenia models, shown in Supplementary Figure 6B, experiment; 0.69 ± 0.17 /μm and 0.56 ± 0.20 /μm for the control and 22q11.2$^{del/+}$, 0.70 ± 0.15 /μm and 0.64 ± 0.16 /μm for the control and Setd1a$^{+/-}$). Second, the size of transient spines was smaller in schizophrenia-associated mouse models in the simulation (0.33 ± 0.033 and 0.20 ± 0.024 (a.u.) for the control and the best-fitted schizophrenia, Supplementary Figure 6C), consistent with data on spine nanostructure (Figure 3G and J).

After the selection of the best-fitted parameters for three mouse models, we compared the optimal values of V1, V2, P1, and P2 between mouse models (Figure 6D). The nascent spine volume increase (V1) was slower in schizophrenia models than in corresponding controls. In turn, the probability of nascent spine loss (P1) was higher in the ASD model. In all three disease models, the probability of spine destabilization (P2) was moderately higher than that in the corresponding controls. Additional simulation results with different P2 values indicate that P2 has a small effect on the overall pattern of spine dynamics. These results suggest that a slow spine volume increase in schizophrenia model mice results in the accumulation of nascent spines with smaller volumes. On the other hand, the spines of ASD model mice grow at a rate similar to that of control spines, but are more likely to be eliminated both in the nascent stage and after maturation.

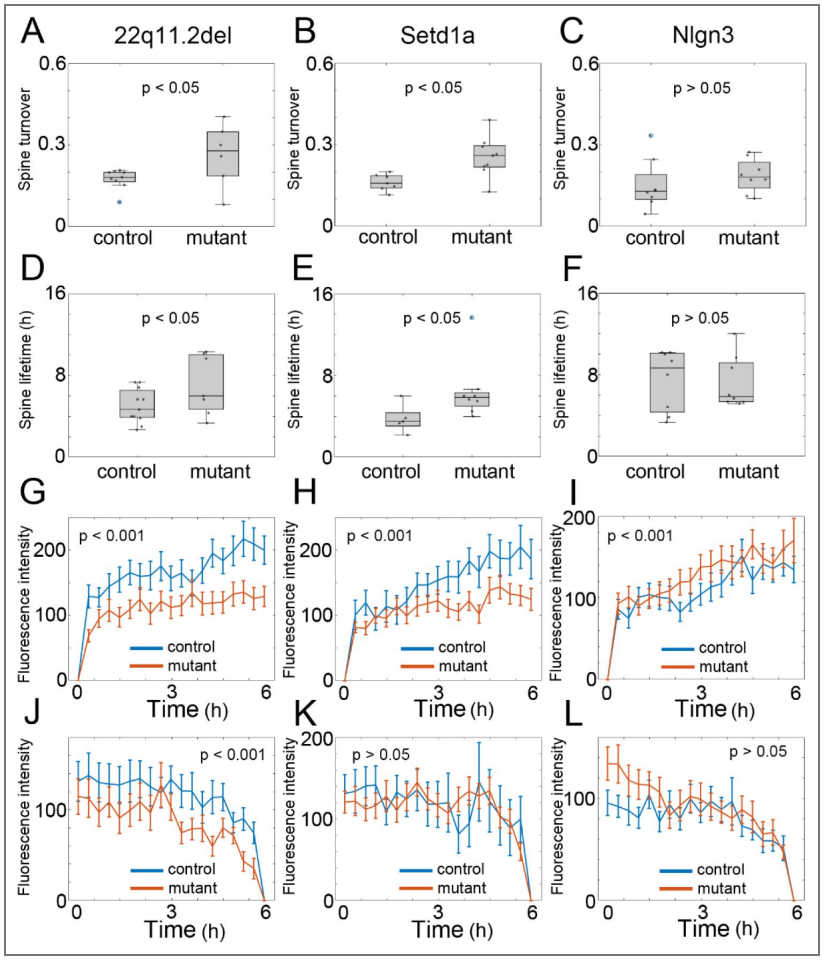

Figure 5. Turnover rate, lifetime, and growth/shrinkage profiles of dendritic spines in cultured neurons derived from 22q11.2$^{del/+}$, Setd1a$^{+/-}$, and Nlgn3$^{R451C/(y\ or\ R451C)}$ mice, as well as the corresponding controls.

(A-C) Spine turnover rates in the three mutant mouse models compared to the controls. Spine turnover rates were analyzed using a linear mixed-effects model with genotype as a fixed effect and plate, cell, and dendrite as nested random effects, showing a significant effect of genotype only in 22q11.2$^{del/+}$ and Setd1a$^{+/-}$ mice (n = 16 dendrites/9 cells/5 plates in control and 11 dendrites/6 cells/4 plates in 22q11.2$^{del/+}$, n = 10 dendrites/7 cells/4 plates in control and n = 14 dendrites/9 cells/6 plates in Setd1a$^{+/-}$, n = 8 dendrites/8 cells/3 plates in control and n = 8 dendrites/8 cells/3 plates in Nlgn3$^{R451C/(y\ or\ R451C)}$). (D-F) Lifetimes of transient spines for the three mutant mouse models compared with corresponding controls. Spine lifetime was analyzed using a linear mixed-effects model accounting for the hierarchical structure of the data (spines nested within dendrites, cells, and culture plates). The analysis revealed a significant effect of genotype only in 22q11.2$^{del/+}$ and Setd1a$^{+/-}$neurons (n = 186 spines/11 dendrites/7 cells/5 plates in control and n = 166 spines/7 dendrites/4 cells/4 plates in 22q11.2$^{del/+}$, n = 82 spines/5 dendrites/5 cells/4 plates in control and n = 202 spines/8 dendrites/8 cells/5 plates in Setd1a$^{+/-}$, n = 98 spines/8 dendrites/8 cells/3 plates in control and n = 125 spines/8 dendrites/8 cells/3 platess in Nlgn3$^{R451C/(y\ or\ R451C)}$). (G-I) Temporal patterns of spine growth (n = 60 spines/11 neurons/7 cells/5 plates in control and n = 50 spines/7 dendrites/4 cells/4 plates in 22q11.2$^{del/+}$, n = 25 spines/5 dendrites/5 cells/4 plates in control and n = 65 spines /8 dendrites/8 cells/5 plates in Setd1a$^{+/-}$, n = 43 spines/8 dendrites/8 cells/3 plates in control and n = 41 spines/7 dendrites/7 cells/2 plates in Nlgn3$^{R451C/(y\ or\ R451C)}$). Spine volume trajectories were analyzed using linear mixed-effects models incorporating nested random effects (spine within dendrite within cell within culture plate) to account for the hierarchical structure of the data. Newly formed spines in both 22q11.2$^{del/+}$ and Setd1a$^{+/-}$ neurons were significantly smaller than those in wild-type neurons. In contrast, newly formed spines in Nlgn3$^{R451C/(y\ or\ R451C)}$ neurons were significantly larger than those in wild-type neurons. (J-L) Temporal patterns of spine shrinkage (n = 39 spines/10 dendrites/6 cells/5 plates in control and n = 37 spines/7 dendrites/4 cells/4 plates in 22q11.2$^{del/+}$, n = 15 spines/5 dendrites/5 cells/4 plates in control and n = 55 spines/8 dendrites/8 cells/5 plates in Setd1a$^{+/-}$, n = 28 spines/8 dendrites/8 cells/3 plates in control and n = 35 spines/8 dendrites/8 cells/3 plates Nlgn3$^{R451C/(y\ or\ R451C)}$ neurons). Spine volume trajectories were analyzed using linear mixed-effects models as in (G-I). In the 22q11.2$^{del/+}$ neurons, spines undergoing elimination were significantly smaller than those in wild-type neurons. This effect was not detected in Setd1a$^{+/-}$ and Nlgn3$^{R451C/(y\ or\ R451C)}$ neurons.

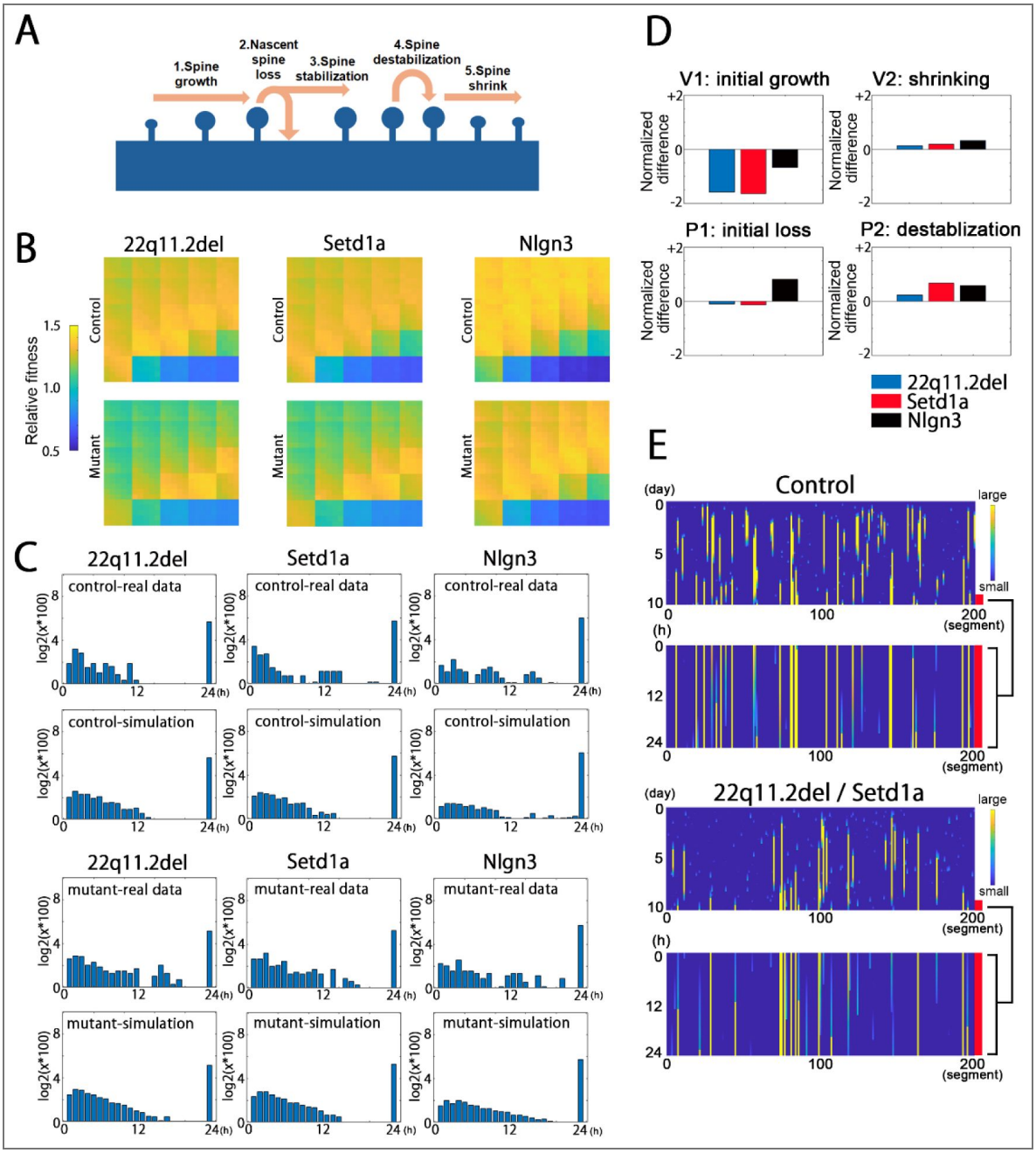

Figure 6. Simulations of long-term spine turnover.

(A) The model of spine dynamics. Five successive phases of spine state transitions were defined. Phase 1: newly formed spines grow at speed V1. Phase 2: nascent spines are eliminated with probability P1. Phase 3: nascent spines are stabilized when volume reaches an upper threshold. Phase 4: stable spines are destabilized with probability P2. Phase 5: spines shrinking at a rate V2 are lost after reaching a lower threshold. (B) Pseudocolor maps of 625 different combinations of these parameters to identify those best fitting the experimental data. The color-coded values indicate the fitness of the simulation results to both the spine lifetime distribution profile and the turnover rate. (C) Frequency histograms of spine lifetimes for the three mouse models and controls (experimental data), and the results of simulations. The bin with a lifetime of 24 h corresponds to the spines that persisted throughout the imaging period. (D) Differences in V1, V2, P1, and P2 between mutant mice and controls, expressed as differences in the four parameters normalized by the control condition values. (E) Plots of individual spine turnover simulated using parameters that best fit the experimental data from control and schizophrenia-associated mouse models. The upper plots show the progression of spine formation along 200 dendritic segments (50 μm) over 10 days. The lower plots show the enlargement of the last 24 h of spine turnover. Color indicates spine size.

Simulated trajectory plots of individual spines along the dendritic shaft, using the best-fit parameters, also reflected the differential patterns of spine turnover in culture preparations derived from control and schizophrenia model mice (Figure 6E). In culture preparations derived from schizophrenia-associated mouse models, there were fewer spines with a lifetime longer than 2 or 3 days, while there was a greater number of spines formed and eliminated within 24 h. This increase in the number of less stable spines explains the pattern of spine lifetimes shown in Figure 5D-E. In summary, these simulations suggest that a reduced spine maturation rate can account for three key properties of schizophrenia-related spines: the greater number of small-volume spines, enhanced turnover, and reduced spine density.

Screening of molecules responsible for altered spine properties in schizophrenia-associated mouse models

Both SIM-based imaging and time-lapse imaging suggest that the initial growth phase of spines is slower in schizophrenia model mice. To identify candidate genes that may contribute to this growth impairment, we performed RNA sequencing of libraries derived from the cultured neurons of eight psychiatric disorder mouse models and corresponding controls, and filtered the results for differentially expressed genes (DEGs) (Supplementary Table 2 and 3). The DEGs specific to more than two schizophrenia-related mouse models are listed in Supplementary Figure 7. In the hippocampi of schizophrenia model mice, the expression levels of Met, Osr1, Arhgap15, and Rnf170-ps were downregulated, whereas those of Cip4, Ecrg4, and Npas4 were upregulated. The majority of these DEGs have been previously implicated in the pathology of schizophrenia (Met)[49], synaptic plasticity (Npas4)[50,51], or signaling pathways in the nervous system (Arhgap15[52], Cip4[53], and Ecrg4[54]).

If these genes do regulate spines in schizophrenia-associated mouse models, manipulation of these genes in wild-type neurons may induce a spine phenotype similar to that observed in these models. To test this possibility, we downregulated Met and Arhgap15, and upregulated Cip4, Ecrg4, and Npas4 in separate wild-type hippocampal neuron cultures and measured spine dynamics using time-lapse imaging (Figure 7A and B, Supplementary Figure 8). The application of a linear mixed-effects model to knockdown experiments revealed no significant effect of treatment ($F(2,6) = 0.29$, $p = 0.76$). In the overexpression experiment, the analysis using a linear mixed-effects model showed a significant main effect of treatment ($F(3,8) = 4.59$, $p = 0.038$), with a significant increase in spine turnover rate by Ecrg4 overexpression ($\beta = 0.49 \pm 0.16$ SE, $t(8) = 3.16$, $p = 0.013$). Thus, the aberrant expression of Ecrg4 may be related to the spine phenotype of schizophrenia model mice.

Ecrg4 encodes a precursor protein that yields several short hormone-like peptides via multiple cleavage sites[55]. Ecrg4 has been reported to function in cell proliferation, inflammation, and tumor suppression. However, there is limited information on the neuronal functions of Ecrg4. Therefore, we further analyzed the cellular distribution of Ecrg4 in wild-type hippocampal neurons to assess its potential synaptic functions. The Ecrg4 protein was detected in the membrane fraction of cultured hippocampal neurons (Supplementary Figure 9A). In addition, HA-tagged Ecrg4 showed punctate localization patterns within the neuronal cytoplasm (Figure 7C). A fraction of HA-tagged Ecrg4 puncta localized at axonal varicosities (arrowheads) or dendritic spines (arrows), together with some extracellular clusters (asterisks). HA-tagged Ecrg4 also colocalized with GFP-tagged neuropeptide Y (NPY) (Supplementary Figure 9B and C), suggesting transport in dense-core vesicles. Surface labeling of live cells also revealed clusters of Ecrg4 on axonal boutons and dendritic spines (Supplementary Figure 9D and E), supporting active exocytosis and tethering via its binding partners to the plasma membrane. Exogenous application of the synthetic Ecrg4 peptide enhanced spine turnover (Supplementary Figure 9F and G). Collectively, these observations suggest that the intracellular machinery for transporting and releasing Ecrg4 may be actively involved in regulating synapse formation and maturation.

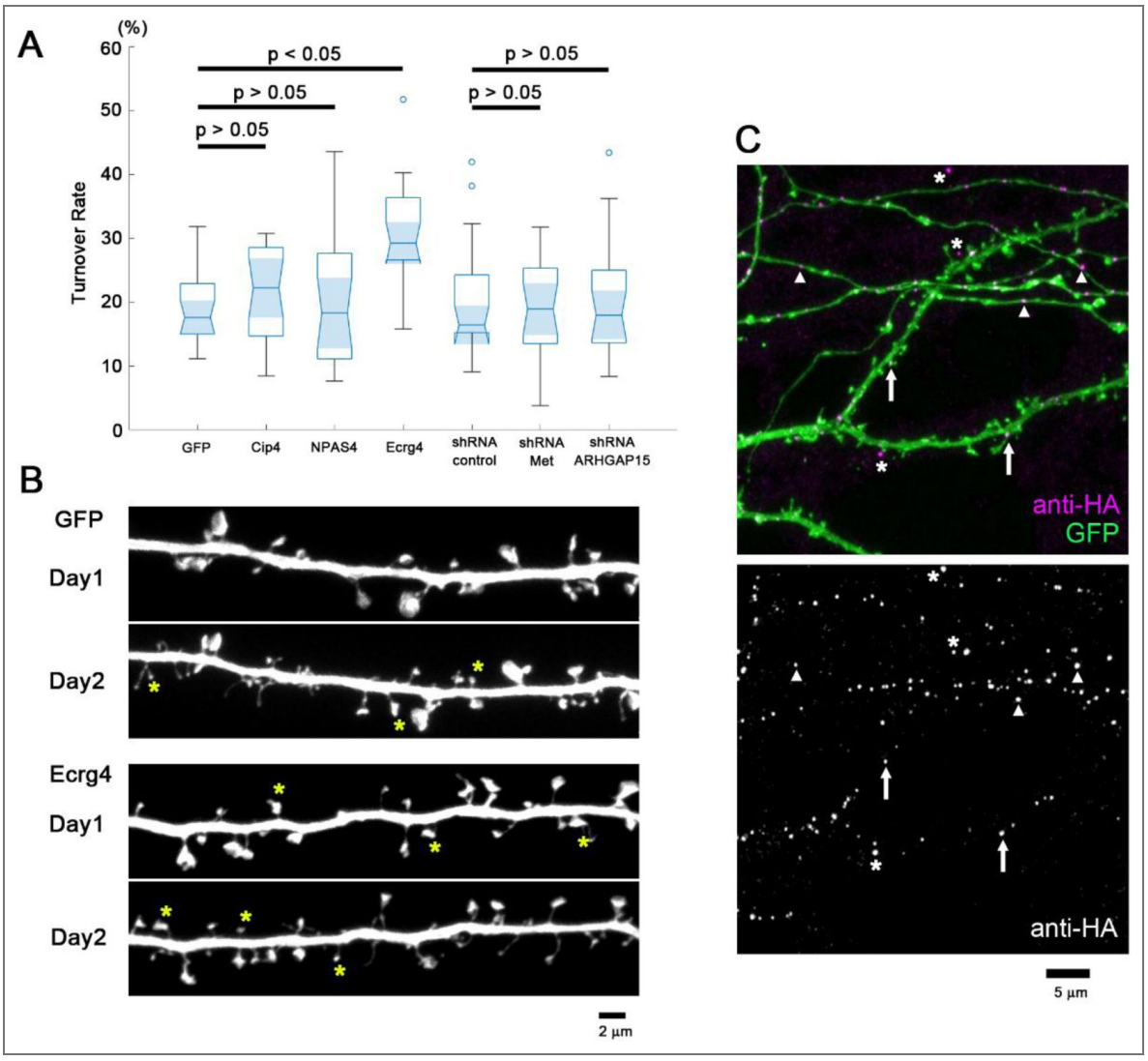

Figure 7. Manipulation of candidate gene expression in wild-type hippocampal neurons and its effects on spine turnover.

(A) Turnover rates of dendritic spines in neurons transfected with an overexpression plasmid encoding Cip4, Npas4, or Ecrg4, or a plasmid encoding an shRNA targeting Met or Arhgap15, together with a GFP expression plasmid. Spine turnover rates were calculated from the images of GFP-expressing dendrites taken at an interval of 24 h. Among the five DEGs, only the upregulation of Ecrg4 selectively increased the spine turnover rate. Linear mixed-effects modeling with experiment as a random factor revealed a significant effect of overexpression treatment ($F(3,8)=4.59$, $p=0.038$), driven by Ecrg4 ($p=0.013$), whereas shRNA manipulations showed no significant effect ($F(2,6)=0.29$, $p=0.76$). (results from n = 22 dendrites/11 neurons/3 culture plates derived from independent primary culture for all conditions except the Met shRNA groups, where n = 21 dendrites from 11 neurons were included in the analysis). (B) Fluorescence images of dendritic segments expressing GFP or GFP plus Ecrg4 on days 1 and 2. Newly formed spines are marked by asterisks. Bar, 2 µm. (C) Images of dendrites and axons expressing HA-tagged Ecrg4 together with GFP. Anti-HA immunocytochemistry revealed the presence of immunopositive puncta both in the dendrites (arrows) and axons (arrowheads). Some clusters could be detected in the extracellular space (asterisks). The upper image is the overlay of the anti-HA signal (magenta) and GFP (green). The lower image shows the distribution of the anti-HA signals. Bar, 5 µm.

Rescue of the synaptic phenotype in schizophrenia-associated mouse models by Ecrg4 suppression

The spatial localization of Ecrg4 protein in wild-type neurons and upregulated gene expression in the hippocampus of schizophrenia model mice strongly suggest a contribution to the observed spine abnormalities. To examine this possibility, we tested whether Ecrg4 suppression by Ecrg4-shRNA rescues the synaptic phenotype of neurons derived from schizophrenia-associated mouse models (Supplementary Figure 8H and I). We introduced a GFP expression plasmid along with the Ecrg4-shRNA plasmid or the control shRNA plasmid into neurons derived from 22q11.2$^{del/+}$ and Setd1a$^{+/-}$ mice (Supplementary Table 1). The spine density plots generated from GFP-expressing neurons differed from those generated from DiI-labeled neurons. This difference may be due to the properties of SIM images obtained from either cell-surface DiI labeling or cytoplasmic GFP expression. Nevertheless, the subtracted (differential) distribution patterns between mutant and wild-type spines under the control shRNA condition indicate the enrichment of small spines (Figure 8A and J). From these plots, we identified the area showing enrichment of mutant spines (Figure 8B and K) and that of wild-type spines (Figure 8C and L). The pattern of small spine enrichment in mutant neurons shown in Figure 8A and J was no longer present in the plots generated by the subtraction of the wild-type spines under control shRNA from the mutant spines under Ecrg4 shRNA, indicating the possible rescue of the phenotype (Figure 8D and M). Consistent with this interpretation, enrichment in both the mutant- and wild-type–dominant regions was attenuated (Figure 8E, F, N, and O).

To determine whether the effect of Ecrg4 shRNA exceeded that expected from random variation in spine counts, we performed a permutation analysis. Spine identities were randomly reassigned between the two conditions while preserving the total number of spines in each dataset, and the differential density maps were recalculated for each permutation. This procedure generated a null distribution of enrichment values expected under random assignment (Figure 8H, I, Q, and R). The level of attenuation observed in both 22q11.2$^{del/+}$ and Setd1a$^{+/-}$ neurons exceeded the 95th percentile of the permuted distributions ($p < 0.05$), indicating that the obtained data were unlikely to be explained by stochastic variation alone (Figure 8G and P). This analysis supports the idea that Ecrg4 downregulation can rescue the spine-shape impairment observed in schizophrenia-related mouse models.

Discussion

We developed an objective method for identifying population-level differences in spine nanostructures and applied it to cultured hippocampal neurons derived from multiple mouse models of psychiatric disorders. We identified two distinct groups of mouse models based on population-level spine properties. Notably, these two objectively identified groups correspond to mouse models with ASD-related gene mutations and schizophrenia-related gene mutations. A higher fraction of the small spine population was a common characteristic of schizophrenia-associated mouse models. Time-lapse imaging of spine dynamics revealed that this smaller spine phenotype is associated with a reduced initial size and growth of spines and their enhanced turnover. Screening for genes differentially expressed between mutant and control mice identified Ecrg4 overexpression as a potential molecular mechanism contributing to the schizophrenia spine phenotype. Indeed, suppression of Ecrg4 expression normalized the spine phenotype in neurons derived from schizophrenia-associated mouse models. These findings support the use of population-level analysis of spine nanostructures as a powerful approach to elucidating the heterogeneous synaptic impairments underlying psychiatric disorders.

Spine nanostructures provide information about developmental history, prior activity, and current functional properties, but these fine structural details were not accessible by conventional light microscopy. However, recent advances in super-resolution microscopy allow for the study of nanoscale spine morphology, including in living preparations, and have revealed new structural features related to important synaptic functions[11–13]. Another challenge to spine nanoscale imaging is the structural heterogeneity across large spine populations, which may obscure

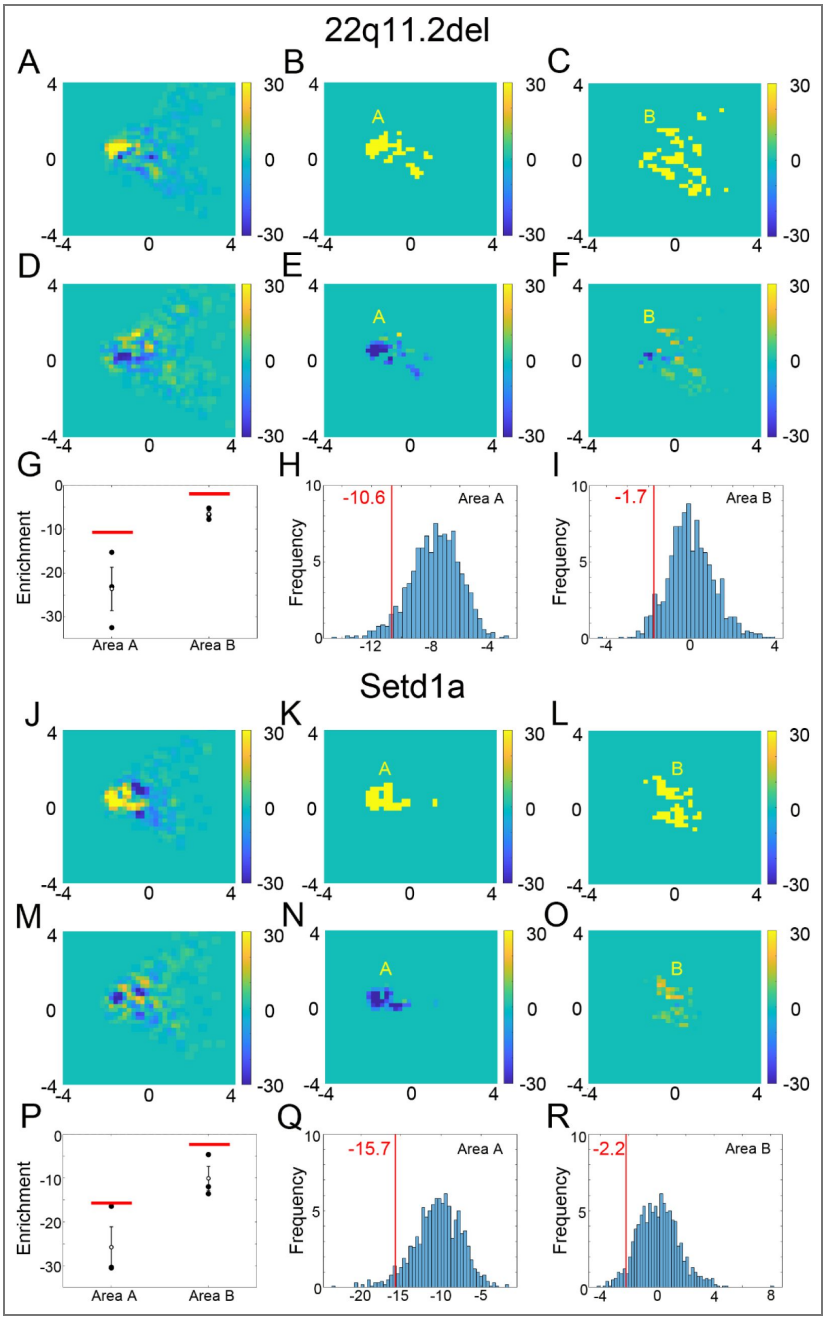

Figure 8. Altered spine population profiles after suppression of Ecrg4 expression in neurons derived from two schizophrenia-associated mouse models: the 22q11.2$^{del/+}$ mouse model (A-I) and Setd1a$^{+/-}$ mouse model (J-R).

(A and J) Density plot obtained by subtracting wild-type spines from mutant spines. Both wild-type and mutant neurons expressed control shRNA. (B and K) Area enriched with the mutant spines under the control shRNA condition. (C and L) Area depleted of the mutant spines under the control shRNA condition. (D and M) Density plot obtained by subtraction of the wild-type spines under control shRNA from the mutant spines under Ecrg4 shRNA. This subtraction illustrates the normalizing effect of Ecrg4 shRNA. (E and N) Reduction of mutant spines in area A by Ecrg4 shRNA. The density plot, obtained by subtracting the mutant spines under control shRNA from those under Ecrg4 shRNA, shows the extent of normalization by Ecrg4 shRNA. (F and O) The increase of mutant spines in area B by Ecrg4 shRNA using the same subtraction method. (G and P) The extent of rescue by Ecrg4 shRNA in Area A and B for three independent culture experiments using either 22q11.2$^{del/+}$ or Setd1a$^{+/-}$ mouse models. The red lines show the values corresponding to statistical significance (p = 0.05), estimated from permutation analyses shown in (H, I, Q, and R). (H and Q) Permutation analysis for Area A to estimate the 95th percentile of the shuffled data. (I and R) Permutation analysis for Area B.

important population-level differences. Nonetheless, to understand the physiology and pathology of neural networks, it is essential to obtain comprehensive information about a large number of spines within a single neuron and across local neuronal networks. We previously reported a dimensional reduction technique coupled with machine learning for evaluating spine properties at the population level [12], and have further refined this method for the current investigation to extract population-level nanostructural features of spines in multiple mouse models of psychiatric disorders. This method enabled us to compare spine phenotypes across different mouse models objectively and group disease models based on similarities and differences in the spine population. Notably, the two identified groups corresponded to ASD- and schizophrenia-related gene mutations, supporting the idea that population-level analyses of spine nanostructures provide meaningful information on synaptic abnormalities and dysfunction.

Population-level spine properties were more homogeneous in schizophrenia models (those with gene mutations implicated in schizophrenia) than in the other 4 models studied, in part due to a shared tendency for smaller spines. This observation is consistent with previous studies on Setd1a mutant mice, which showed reduced spine width, decreased mushroom-type spines, and lower spine density in the prefrontal cortex[43,56,57]. In contrast to these findings, several previous studies reported reduced numbers of small spines in the postmortem cortical tissues of schizophrenia patients[22,58]. However, this discrepancy may be attributed to the developmental period, as we examined fetal neuronal spines after 3 weeks of in vitro differentiation, whereas the aforementioned studies included postmortem samples from patients over 40 years of age. One possible scenario that may help unify these observations is that spine density is reduced in the early postnatal period, and that this reduction triggers homeostatic plasticity, which, in turn, reduces the fraction of small spines in later life. Another potential explanation is that schizophrenia differentially affects regional spine properties (e.g., hippocampus versus cortex). Previous *in vivo* two-photon imaging studies reported higher spine turnover in the hippocampus than the cortex[59,60].

Therefore, the spine phenotype identified in this study may be specific to hippocampal pyramidal neurons. Finally, while the spine phenotype identified in the human postmortem brain undoubtedly resulted from complex interactions among genetic background, environmental influences, and regulation by non-neuronal cells, data from pure neuronal cultures are more likely to reflect the direct effects of schizophrenia-related gene mutations on synaptic functions. This property may be advantageous for identifying synaptic molecules that regulate synapse phenotypes in schizophrenia-related mouse models. However, the phenotype observed in the culture system requires confirmation using in vivo experiments of mouse models or human tissue samples. Efficient in vitro screening combined with reliable in vivo evaluation of synapses will facilitate translational research on mental disorders.

In addition to Ecrg4, these analyses identified several other DEGs common to mice harboring schizophrenia-related mutations. However, time-lapse imaging identified Ecrg4 as the most effective spine regulator, and we also found that Ecrg4 suppression reversed the abnormal spine phenotype in neurons derived from schizophrenia model mice. Ecrg4 encodes a precursor protein of hormone-like peptides [61]. Exogenously expressed Ecrg4 exhibited a punctate pattern in both axonal and dendritic compartments, with a fraction of clusters present on the cell surface. This observation indicates that Ecrg4 may be secreted locally by axons or dendrites, thereby influencing synapses and adjacent neurons. Several signaling pathways act downstream of Ecrg4, including the stress-related NF-κB pathway and PI3K/Akt/mTOR pathway[55]. Ecrg4-derived peptides may also act through Toll-like receptor 4 (TLR4) or multiple scavenger receptors, such as LOX1[61]. While Ecrg4-related signaling pathways have been studied primarily in the context of inflammation and infection, there are few studies on Ecrg4-related signaling pathways in neurons. However, an Ecrg4-deficient mouse model demonstrated enhancements in neural stem cell proliferation and spatial learning, suggesting that overexpression may disrupt hippocampal function[54]. We suggest that Ecrg4 may be a critical regulator of neural development and

synaptogenesis in the hippocampus. Further studies are warranted to identify Ecrg4 receptors and downstream signaling pathways and to investigate the potential dysfunction of these pathways in schizophrenia-associated mouse models.

The nanoscale features of dendritic spines in ASD-associated mouse models were more variable than those in schizophrenia-associated mouse models. This difference may be related to the broader clinical spectrum of ASD, which ranges from mild impairments in social skills to severe intellectual disability. The four ASD-associated mouse models examined in this study, Nlgn3$^{R451C/(y\ or\ R451C)}$, Syngap1$^{+/-}$, POGZ$^{Q1038R/+}$, and 15q11-13$^{dup/+}$, may represent subgroups with different levels of hippocampal dysfunction. Among the four ASD-associated mouse models, 15q11-13$^{dup/+}$ showed population-level spine properties closer to those of the schizophrenia models. To understand this similarity, further analysis of neural circuit changes in both ASD- and schizophrenia-associated mouse models will be necessary. Analysis of the relationships between rare genetic variants and synapse phenotypes in mouse models may contribute to their eventual categorization. This information should be useful to understand the underlying mechanisms of the broader clinical spectrum of ASD.

The most important advantage of our analytical method is reproducibility, despite the substantial heterogeneity in genotype and phenotype among these mouse models. Thus, we are confident that the spine population analysis described here will help researchers in different laboratories obtain reliable and comprehensive information on spine properties. Further, this method could facilitate comparisons across a large number of mouse models harboring mutations associated with mental disorders. Spine morphology as measured in a reduced culture system can also demonstrate direct effects of gene mutations on neuronal phenotypes in the absence of indirect influences from nonneuronal cells or specific environments. Ultimately, these studies may identify the shared and specific pathogenic mechanisms of psychiatric disorders and lead to improved diagnosis and treatments.

Materials and Methods

Neuronal culture and genotyping of tissue samples from genetically modified mice

The following mouse models of psychiatric disorders were examined for spine nanostructural characteristics: male hemizygous or female homozygous neuroligin-3 R451C mutant (Nlgn3$^{R451C/(y\ or\ R451C)}$), heterozygous Syngap1 mutant mice (Syngap1$^{+/-}$), heterozygous POGZ mutant mice (POGZ$^{Q1038R/+}$), mice with duplication of chromosome 7C (15q11-13$^{dup/+}$; corresponding to human 15q11-13 duplication), mice heterozygous for deletion on chromosome 16B2,3 (3q29$^{del/+}$; corresponding to human 3q29 deletion), mice heterozygous for deletion on chromosome 16qA13 (22q11.2$^{del/+}$; corresponding to 1.5 Mb deletion on human 22q11.2), mice heterozygous for Setd1a mutantion (Setd1a$^{+/-}$), and Ca^{2+}/calmodulin-dependent protein kinase IIα kinase-dead mutant mice (CaMKIIα$^{K42R/K42R}$). All animal experiments were reviewed and approved by the Institutional Animal Care and Use Committee of the University of Tokyo (permission number A2023M031-02).

For the production of embryos harboring heterozygous mutations, male heterozygous mutants were bred with wild-type female C57BL/6J or C57BL/6N mice (Japan SLC). Because neuronal cultures were prepared from wild-type and mutant littermates sharing the same genetic background, differences between the C57BL/6J and C57BL/6N sub-strains are unlikely to have affected the analysis. For the production of Nlgn3$^{R451C/(y\ or\ R451C)}$ embryos, Nlgn3$^{R451C/y}$ males and Nlgn3$^{R451C/+}$ females were crossed. Embryos of CaMKIIα$^{K42R/K42R}$ mice were obtained by crossing heterozygous CaMKIIα$^{K42R/+}$ males and females. Both male and female embryos were used for the primary culture. Control cultures were prepared from embryos without disease-related mutations on the background of either C57BL/6J or C57BL/6N.

Genomic DNA was purified from E16 embryos prior to brain dissection using the QuickGene DNA tissue kit (WAKO), and genotypes were determined by PCR using either KapaTaq (Kapa Biosystems) or KOD FX Neo (TOYOBO) following the standard protocols provided by the

manufacturers. The primer sequences used for genotyping were as follows:

Nlgn3$^{R451C/(y\ or\ R451C)}$ genotyping:

Sense primer: 5'- GGTCAGAGCTGTCATTGTCAC-3'

Antisense primer: 5'- TGTACCAGGAATGGGAAGCAG-3'

Syngap1$^{+/-}$ genotyping:

Sense primer for WT: 5'-GTCAGTGGGACATGGAAGTAG-3'

Sense primer for mutant: 5'-CTTCCTCGTGCTTTACGGTATC-3'

Antisense primer (common): 5'-CTGATCAGCCTGTCAGCAATG-3'

POGZ$^{Q1038R/+}$genotyping:

Sense primer for WT: 5'- TCTGTGAAGAAGCTTCGGGTAGTAC-3'

Antisense primer for WT: 5'-GTCTCCTCATTTACAGGGAGCT-3'

Sense primer for mutant: 5'- GCAGCGGCTCCCCGTTAAC-3'

Antisense primer for mutant: 5'- AGCGCACAGCCCACTCATAG-3'

15q11-13$^{dup/+}$ genotyping:

Sense primer: 5'- AGAGGAGGGCCTTACTAATTACTTA-3'

Antisense primer: 5'-ATATGTACTTTTGCATATAGTATAC −3'

3q29$^{del/+}$ genotyping:

Sense primer for WT: 5'- TTGGCACCACTCGCCCAAGTTATATCCACC-3'

Sense primer for mutant: 5'- CAAGGGGGAGGATTGGGAAGACAATAGCAG-3'

Antisense primer (common): 5'- GGTCATGCAAATTCTAGCAGTGAGTCATGAC-3'

22q11.2$^{del/+}$ genotyping:

Sense primer for WT: 5'- GAGAAAGTGGGTGGGAAGGC −3'

Antisense primer for WT: 5'- GTCCCTCGCCACAGTCATAA −3'

Sense primer for mutant: 5'- CTAAGGAATGGTTCCGGCCA −3'

Antisense primer for mutant: 5'- TTTCACGGAGGCGGTATTCA-3'

Setd1a$^{+/-}$ genotyping:

Sense primer: 5'-CTCGCCGCCATTTCTCTACATC-3'

Antisense primer: 5'-GTTCTGGAGGTTCTGGAGGTG-3'

CaMKIIα$^{K42R/K42R}$ genotyping:

Sense primer: 5'-GGTCTTGAAGACTGTCTGGTGTGAGA-3'

Antisense primer: 5'-CACAGGCCAGTTTAGGTCTTGCTAGG-3'

After genotyping, primary hippocampal neuron cultures were prepared from mutant and corresponding control embryonic samples as described previously[12,62]. In brief, E16 hippocampi were dissected, minced, treated with trypsin (Gibco) and DNase (SIGMA), and dissociated mechanically into a cell suspension. Cells were resuspended in minimum essential medium supplemented with B18 supplement, L-glutamine (Gibco), and 5% fetal calf serum (Equitech-Bio), and plated onto glass-bottom dishes (MatTek, #1.5) precoated with poly-L-lysine (SIGMA). Glial proliferation was prevented by adding 5 μM Ara-C (SIGMA) 2 days after plating. For the comparison of spine nanostructure between wild-type and mutant neurons, culture samples were processed for imaging at 18-22 DIV. For comparison of 8 mutant mouse models using SIM imaging, all imaging data were obtained from the samples fixed at 19 DIV. For pharmacological treatment, 10 μM CNQX or 20 μM bicuculline was applied to the culture medium at 13 DIV, and samples were processed for imaging at 19 DIV.

Transfection and fluorescence labeling of primary hippocampal neurons

Primary neurons were transfected with the indicated vectors using the calcium phosphate precipitation method at 8–9 DIV according to a previously described procedure[63]. All fluorescent proteins were expressed under the control of the β-actin promoter.

The expression of the shRNA constructs was induced using the pSilencer vector system. Briefly, the 19-nt target sequence and the reverse complement sequence of the target were ligated into the shRNA expression vector separated by a 9-nt spacer loop (TCTCTTGAA) (pSilencer 2.0-U6; Invitrogen). Stealth RNAi Negative Control Duplexes (Invitrogen) were used as control shRNAs. The targeting sequences for mouse Met, Arhgap15, and Ecrg4 are as follows:

Met RNAi sequence:

5'-GCAGTGAATTAGTTCGCTA-3

Arhgap15 RNAi sequence:

5'-AAGACAGATGTGAACATAC-3

Ecrg4 RNAi sequence:

5'- GAGGCTAAATTTGAAGAT-3'

The suppression of target protein expression by these transfected shRNAs was tested by immunoblotting lysates of COS-7 cells co-transfected with a target gene construct fused to a sequence encoding amino acids 98–106 of human influenza hemagglutinin (HA), all under the control of the β-actin promoter. Overexpression of Cip4, Ecrg4, and Npas4, genes upregulated in cultures derived from mouse models of schizophrenia, was induced by transfection of plasmids containing the corresponding HA-fused cDNA under the control of the β-actin promoter. Briefly, mouse Trip10 transcript variant 4 (Cip4; NM_001242391) and mouse Ecrg4 (NM_024283) were cloned, and an HA tag was inserted into the C-termini. Mouse Npas4 (NM_153553) was cloned according to a previous report[64] and fused with a Flag-HA tag at its C-terminus. Human neuropeptide Y (NPY) tagged with green fluorescent protein (GFP, a kind gift from Dr. J. Takaska, NIH) was expressed under the control of the β-actin promoter.

For cell surface labeling of individual neurons in culture, cells were fixed and stained with 1,1'-dioctadecyl-3,3,3',3'-tetramethylindocarbocyanine perchlorate (DiI; Molecular Probes) as described previously[12].

Immunocytochemistry

Cultured hippocampal neurons expressing HA-tagged constructs were fixed with 2% paraformaldehyde in PBS, permeabilized with 0.2% Triton X-100 in PBS, blocked with 5% normal goat serum, and reacted with rabbit anti-HA antibody (1:500; MBL), mouse anti-HA antibody (1:100; Biolegend), mouse anti-β-galactosidase antibody (1:500, SIGMA), rabbit anti-Ecrg4 (1:100, SIGMA), mouse anti-GM130 antibody (1:100, BD Biosciences), rabbit anti-Cip4/TRIP10 antibody (1:100, Proteintech), rabbit anti-NPAS4 antibody (1:100, Activity Signaling), and chicken anti-MAP2 antibody (1:500, PhosphoSolutions). After washing with PBS, samples were reacted with Alexa Fluor 546-labeled goat anti-rabbit IgG antibody (1:500; Invitrogen) and Alexa Fluor 647-labeled goat anti-mouse IgG antibody or anti-chicken IgY antibodies (1:500; Invitrogen). For cell surface labeling with GFP, neurons expressing Ecrg4-HA-SEP (superecliptic pHluorin) were reacted with anti-GFP VHH/nanobody conjugated to Alexa Fluor 647 (1:4,000; Chromotek) in culture medium at 37°C.

Structured illumination microscopy (SIM) imaging

For 3D-SIM imaging, we used an inverted microscope (ECLIPSE Ti-E, NIKON) equipped with an N-SIM-E system, 405, 488, 561, and 640 nm diode lasers (LU-NV, NIKON), and an oil-immersion TIRF objective lens (SR Apo TIRF 100 ×, N.A. 1.49, NIKON). All SIM images were acquired under strictly controlled conditions, including a stage temperature of 28–29°C, to minimize the position and

aberration fluctuations. Spherical aberrations induced by refractive index mismatch were reduced by manually adjusting the objective lens correction collar. Images were acquired using an EMCCD camera (iXon3 DU-897E, Andor Technology) with 512 × 512 pixels (each pixel, 16 μm square) operated in the read-out mode at 1 MHz with 16-bit analog-to-digital conversion of the EM gain. All image-processing steps were performed in three dimensions. The acquired image datasets were computationally reconstructed using the reconstruction stack algorithm V2.10 of NIS-Elements AR (NIKON). An image stack consisted of 63 axial (z) planes of 512 × 512 pixels in the x- and y-dimensions, with a pixel size of 32 × 32 nm. All 3D images were reconstructed in 120-nm z-steps spanning 7.56 μm in the z-axis. The voxel size met the Nyquist criterion. Only dendritic segments spatially isolated from other fluorescent objects were selected for analysis because objects brighter than the targeted dendritic segments made image thresholding unreliable. Quality checks of the acquired SIM images were performed as described previously using the SIMcheck plugin for ImageJ[65].

Spine isolation and shape measurement

Spines were isolated by automated image thresholding using a previously described method[12]. Briefly, the reconstructed SIM image stacks were first processed by multilevel thresholding using the MATLAB built-in function [multithresh()] to produce binary images, which were further processed by geodesic active contours using the MATLAB built-in function [activecontour()]. The binary image stacks generated by thresholding the SIM images were then processed for the automated detection of spines. First, the dendritic shafts were fitted with elliptic cylinders and voxel clusters outside the best-fit elliptic cylinders were identified as spine candidates. Next, the spine candidates were classified by volume and shape. After selection, the junction between the dendritic shaft and spine was determined. Finally, the nanostructural parameters of isolated spines were measured. These steps are basically the same as those in our previous algorithm, but several points were improved, as described in the following sections (The original code for SIM image processing is available at *https://shigeookabe.github.io/download-page-SIM/* with a password of “simspineimage”).

(1) Dendritic shaft fitting

We first estimated the shaft volume using the custom-made function “SIM_Fitdendrite” as previously described. In the new algorithm, the candidate spines were subsequently evaluated to determine whether their bases were large and spread on the shaft surface. If the spine base was large, the basal voxels were removed using the function “SIM_Removevoxel.“

(2) Selection of the spines

Using the custom-made function “SIM_Position,” spines with volumes too small, too elongated, or located at the image edge were removed as previously described. Small spine candidates with volumes less than twice the volume of a rectangular cuboid with edge lengths equal to the theoretical resolutions of SIM images (<0.01 μm^3) were rejected.

(3) Adjustment of the spine–shaft junction

We determined the location of spine–shaft junction using the custom-made function “SIM_Junction.” This step was identical to our previous algorithm. Next, spines with more than one connection site to the shaft were detected using the function “SIM_Neck” and eliminated from further analysis.

(4) Measurement of nanostructural parameters

First, the angle of the spines was adjusted to be perpendicular to the long axis of the dendritic shaft and within the xy-plane using the function “SIM_Angle.” Next, nanostructural parameters were measured using the function “SIM_Shape.” In our previous spine shape measurement study, a polygon mesh-based calculation was performed. In the current study, we took a different approach using voxel-based measurement. The calculation of structural parameters using voxel data was more straightforward and required fewer calculation steps than the method based on polygon mesh data. Spines were divided into 160-nm segments along the long axis using the

function “SIM_Shape.” These spine segments were used to calculate the following 64 nanostructural parameters: spine length, surface area, base surface area, total volume, volume of each spine segment (20 segments), convex hull volume of each spine segment (20 segments), and convex hull ratio of each spine segment (20 segments).

Analysis of the spine population data

Differences in spine phenotype among model mice were analyzed at the population level by PCA. We selected five parameters (spine length, base surface, total volume, and volumes of the fifth and fifteenth spine segments) for the PCA-based dimensional reduction. Two parameters that reflect the principal structural features (length and volume) were first selected. Second, three other parameters (base surface, volumes of the fifth and fifteenth spine segments) that were mutually independent and also independent from the first two parameters were chosen (pairwise correlation coefficients < 0.3). The initial 64 parameters included the volume of each spine segment (20 segments), the convex hull volume of each spine segment (20 segments), and the convex hull ratio of each spine segment (20 segments). These parameters showed higher correlation coefficients but did not improve PCA performance. We also confirmed that PCA using all 64 parameters yields a cross-correlation map similar to that shown in Fig. 2B. The first three principal components (PC1–PC3) covered approximately 90% of the variance in the data.

The 2D presentation of spine population data using PC1 and PC2 reflected the overall pattern of the spine shape distribution, with thin, mushroom, and stubby spines separated in the feature space. We found that the overall pattern of spine population data projected to the PC1-PC2 plane differs between DiI-labeled neurons and GFP-expressing neurons. This difference may be due to the properties of SIM images obtained from either cell-surface labeling or cytoplasmic GFP expression. To facilitate the direct comparison of the spine population data in Figure 3 (DiI-labeled neurons) and Figure 8 (GFP-expressing neurons), we transformed the raw data of GFP-expressing neurons using the weight matrix calculated from the data for DiI-labeled neurons.

After PCA, relative spine densities (spine number per area in the feature space) were mapped onto an 80 × 80 grid spanning ±4 standard deviations along PC1 and PC2. Using this procedure, two density plots were generated: one from culture samples of disease model mice and the other from corresponding control cultures. The two density plots were then subtracted to extract the local differences in spine numbers. Because each grid contains spines with similar structural parameters, the subtracted plot reveals regions of mutant-dominant and wild-type-dominant spine distributions in the PC1–PC2 plane.

The similarity between the two subtracted density plots was evaluated by calculating the 2D cross-correlation C using the following equation

$$C = \frac{\sum_{m=1}^{M}\sum_{n=1}^{N} X(m,n)Y(m,n)}{\sqrt{\sum_{m=1}^{M}\sum_{n=1}^{N} X(m,n)X(m,n)}\sqrt{\sum_{m=1}^{M}\sum_{n=1}^{N} Y(m,n)Y(m,n)}}$$

where X and Y correspond to the two subtracted density matrices. The 11 different subtracted density plots shown in Figure 2 were clustered using the MATLAB function “linkage,” and the average distance between all pairs of elements in the two samples was calculated using the cluster algorithm.

For Figure 3, the PC1–PC2 feature space was divided into four subareas with distinct shape properties: (1) small and short, (2) small and long, (3) large and short, and (4) large and long. The median spine volume and length were first calculated from the wild-type population, and spine samples were classified into four subgroups based on these median values. Each position of the 80 × 80 grid was then labeled according to the dominant subgroup of spines it contained, yielding a map of four subareas corresponding to the four spine shape categories.

In Figure 3, 8, and Supplementary Figure 3, areas in the feature space enriched with mutant or control spines were extracted by searching the 80 × 80 grid and identifying those where the difference in relative density was larger than the mean plus 3 × SD. Spine axial profiles in Supplementary Figure 5 were then analyzed within areas enriched with either mutant or control spines.

Time-lapse imaging of dendritic spines and image analysis

Live cell 3D imaging was performed using an A1 confocal laser scanning microscope (NIKON) equipped with 405, 488, 561, and 640 nm diode lasers (LU-NV, NIKON). Cells at 15–18 DIV were maintained at 37°C under a continuous flow of 5% CO_2 to maintain medium pH using a heater stage system (INUG2H-TIZSH, Tokai Hit) with a lid designed for a glass-bottom dish to minimize evaporation. Horizontal and vertical drifts were controlled by a motorized stage and a perfect focus system, respectively. Images were acquired with an oil immersion objective lens (60×, NA 1.4, NIKON) at a confocal aperture of 1 AU. The imaged volume was 30.7 × 30.7 × 7.56 µm in x, y, and z directions, respectively, and image stacks consisted of 17 planes separated by 500 nm. Time-lapse images were recorded either at short intervals (15 min intervals for 24 h) or long intervals (two time points separated by 24 h). Cultured neurons imaged at a 24-h interval were then fixed and immunostained with anti-HA to confirm the expression levels of the transfected genes. The effect of exogenously applied Ecrg4 peptide (CΔ16; the C-terminal ECRG4 fragment of 16 aa, 5.4 µM, BEX CO., LTD.) was evaluated by taking time-lapse images at 24 h intervals, with the first image taken just before the peptide application.

The image stacks obtained by time-lapse imaging were analyzed using custom-made MATLAB scripts. First, 2D images were generated by maximal intensity projection of z-stack images. These 2D images were processed to transform the outlines of dendritic shafts to be aligned with straight lines. Spines were subsequently identified as objects extending beyond the straight edges of the dendritic shafts. Identified spines were segmented, and total fluorescence intensities were measured as a proxy for spine volume. We classified the spines as stable (present throughout the imaging period), newly formed (appearing within 24 h imaging period), and eliminated (lost within 24 h imaging period). For newly formed and eliminated spines, we generated temporal profiles of growth and shrinkage using the total fluorescence intensity values.

RNA sequencing and gene expression analysis

Total RNA was isolated from cultured hippocampal neurons at 19 DIV using the RNeasy Mini Kit (QIAGEN) with the RNase-Free DNase Set (QIAGEN) according to the manufacturer's protocols. The quality of the extracted RNA was initially assessed using a NanoDrop spectrophotometer, and the RNA integrity number (RIN) score was calculated for each sample using a Bioanalyzer (Agilent Technologies). The yields were quantified using a Qubit Fluorometer (Thermo Fisher Scientific). Sequencing libraries were prepared using the NEBNext Ultra Directional RNA Library Prep Kit for directional libraries (New England BioLabs) and the KAPA HTP Library Preparation Kit (KAPA Biosystems) according to the manufacturers' protocols. Paired-end RNA-seq libraries were sequenced using the Illumina HiSeq and MGI DNBSEQ-G400 platforms. Three independent culture preparations were used for RNA sequencing of each mouse model and control library. Following quality control, the reads were aligned with the mouse reference genome GRCm38/mm10 (GenBank assembly ID: GCA_000001635.2).

Expression levels of genes were analyzed based on the transcripts per million and differential expression analysis was conducted using the DESeq2 package in R[66]. Differentially expressed genes (DEGs) were selected according to an adjusted $P < 0.05$ and a (log2)-fold change greater than 0.5.

Simulation of spine development

Spine growth was simulated using a dendrite model consisting of 1,000 segments, each 0.25 µm in length (250 µm in total). The spine distribution was updated every 20 min over 10 days, covering the initial phase of spine development from 8 DIV to 17 DIV. The initial probability of new spine generation was set at 7.5×10^{-3} per segment per hour and decreased thereafter in proportion to the accrued spine density increase (by the final 24 h, the probability of spine generation [mean ± SD] was $3.2 \times 10^{-3} \pm 0.23 \times 10^{-3}$/segment/h). This probability function yielded an average of 1.2 ± 0.22 new spines per 10 µm of dendrite every 24 h, in good agreement with the spine dynamics measured by time-lapse imaging from 15–18 DIV (1.3 ± 0.63 new spines per 10 µm of dendrite

every 24 h). The model also set the increase in spine volume (V1) from 6.7×10^{-3} to 3.3×10^{-2} in 20 min. Spines in the early growth phase were treated as unstable, with loss probability P1 ranging from 9.0×10^{-3} to 0.1 every 20 min. Spines were modeled as stabilized when the individual volume reached a relative value of 1.0.

These stabilized spines then entered a shrinking phase with a probability P2 ranging from 2.9×10^{-3} to 4.0×10^{-3} in 20 min. The shrinking rate V2 was set from 6.7×10^{-3} to 3.3×10^{-2} per 20 min. In simulations, the four parameters V1, V2, P1, and P2 were varied within these indicated ranges to find the combination producing the best fit with experimental data on the difference in spine lifetime distribution profile and turnover rate at 24 h (the actual measurement interval). The simulation with the best-fit parameters yielded a spine density comparable to measured data (0.57 ± 0.029 vs. 0.70 ± 0.17 spines/μm of dendrite).

Western blotting

Total protein extracts from cultured hippocampal neurons were separated into cytosolic and membrane fractions using Trident Membrane Protein Extraction Kit (GeneTex) according to the manufacturer's protocol and separated on 10% sodium dodecyl sulfate (SDS)-polyacrylamide gels or 15%–20% Tricine-SDS-polyacrylamide gels. The separated proteins were then transferred onto nitrocellulose membranes (Millipore) or PVDF membranes (Bio-Rad) using a wet transfer system. Membranes were blocked with 5% bovine serum albumin in Tris-buffered saline plus Tween-20 (TBS-T, 20 mM Tris-HCl, 137 mM NaCl, 0.2% Tween-20) for 1 h at room temperature, then incubated overnight at 4°C with rabbit anti-Ecrg4 (1:1,000, SIGMA), rabbit anti-GluA1 (1:1,000, Nittobo Medical), rabbit anti-GFP (1:3,000, MBL), rabbit anti-dsRed2 (1:4,000, Nittobo Medical), mouse anti-α-tubulin (1:3,000, SIGMA) as indicated. The membranes were washed and incubated with HRP-conjugated secondary antibody against mouse or rabbit IgG (1:10,000, Amersham) for 2 h. Signals from the target protein bands were detected using a SuperSignal™ West Femto or Atto detection kit (Pierce) and imaged for quantitation (densitometry) using a ChemiDoc imaging system (Bio-Rad). We isolated the fraction of synaptosomes using Syn-PER™ Synaptic Protein Extraction Reagent (Thermo Scientific) in Supplementary Figure 9A, according to the manufacture's protocols.

Statistics

The statistical tests used for each experiment and the sample sizes (spines, dendrites, cells, and plates) are indicated in the corresponding text or figure legends. Statistical significance was determined as follows:

Figure 3G-J: One-way ANOVA followed by Tukey's post hoc test.

Figure 5A-C: A linear mixed-effects model with genotype as a fixed effect and plate, cell, and dendrite as nested random effects.

Figure 5D-F: A linear mixed-effects model with genotype as a fixed effect and plate, cell, dendrite, and spine as nested random effects.

Figure 5G-L: A linear mixed-effects model with genotype as a fixed effect and plate, cell, dendrite, spine, and time as nested random effects.

Figure 7A: A linear mixed-effects model with treatment as a fixed effect and plate, cell, and dendrite as nested random effects.

Figure 8: Three independent imaging datasets evaluated by permutation tests.

Statistical significance was set at $P < 0.05$.

Supplementary Figures

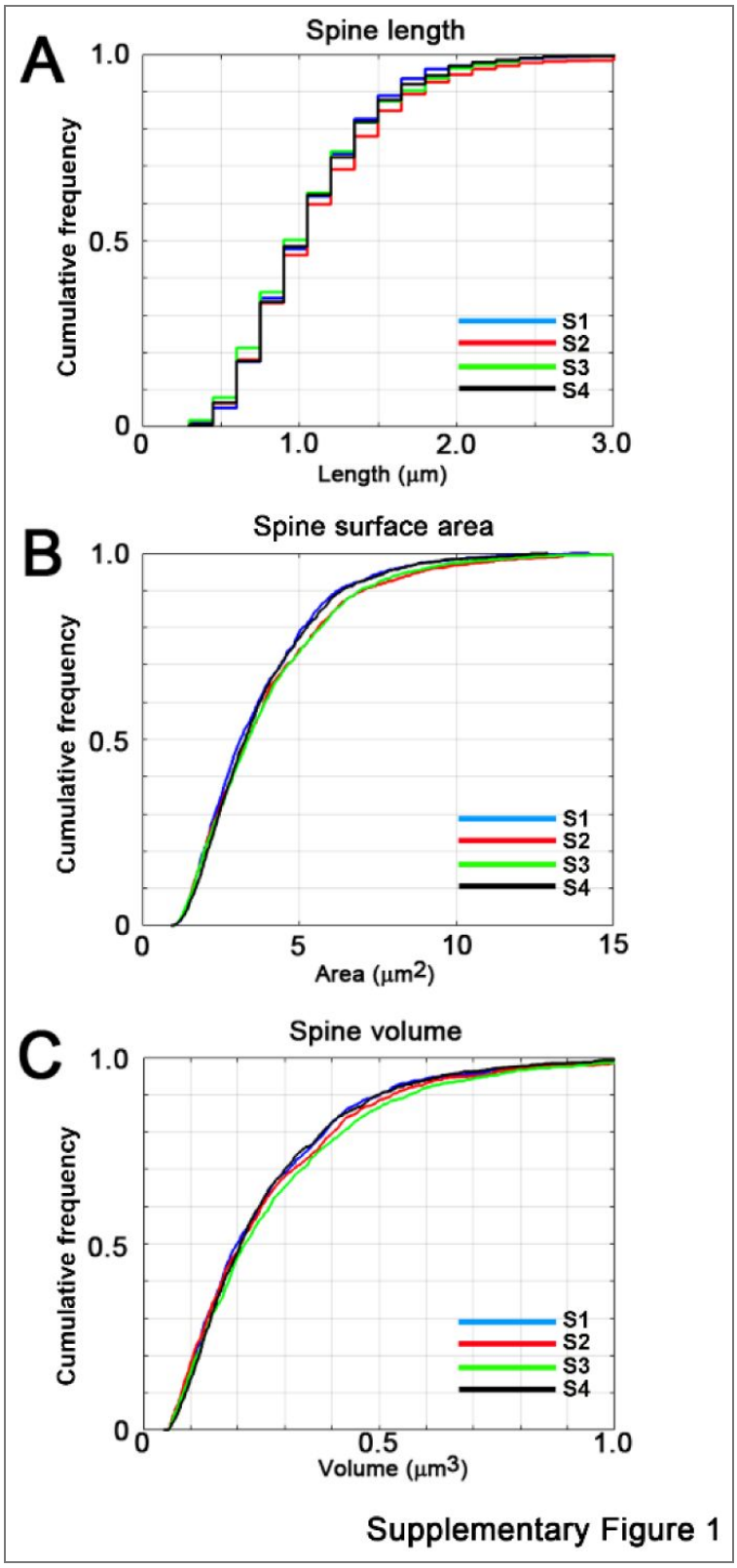

Supplementary Figure 1. Cumulative frequency plots of spine length, surface area, and volume measured in four independent experiments performed > 2 months apart. The cumulative frequency distributions of spine length (A), spine surface area (B), and spine volume (C) were obtained from wild-type data acquired by SIM imaging across four mouse models: Nlgn3$^{R451C/(y\ or\ R451C)}$ (S1), Syngap1$^{+/-}$ (S2), POGZ$^{Q1038R/+}$ (S3), and 15q11-

$13^{dup/+}$ (S4). The Kolmogorov–Smirnov test detected significant differences in only three of 18 possible pairwise comparisons: surface area of (S1) vs. (S3) ($p = 0.017$), volume of (S1) vs. (S3) ($p = 0.032$), and volume of (S3) vs. (S4) ($p = 0.038$).

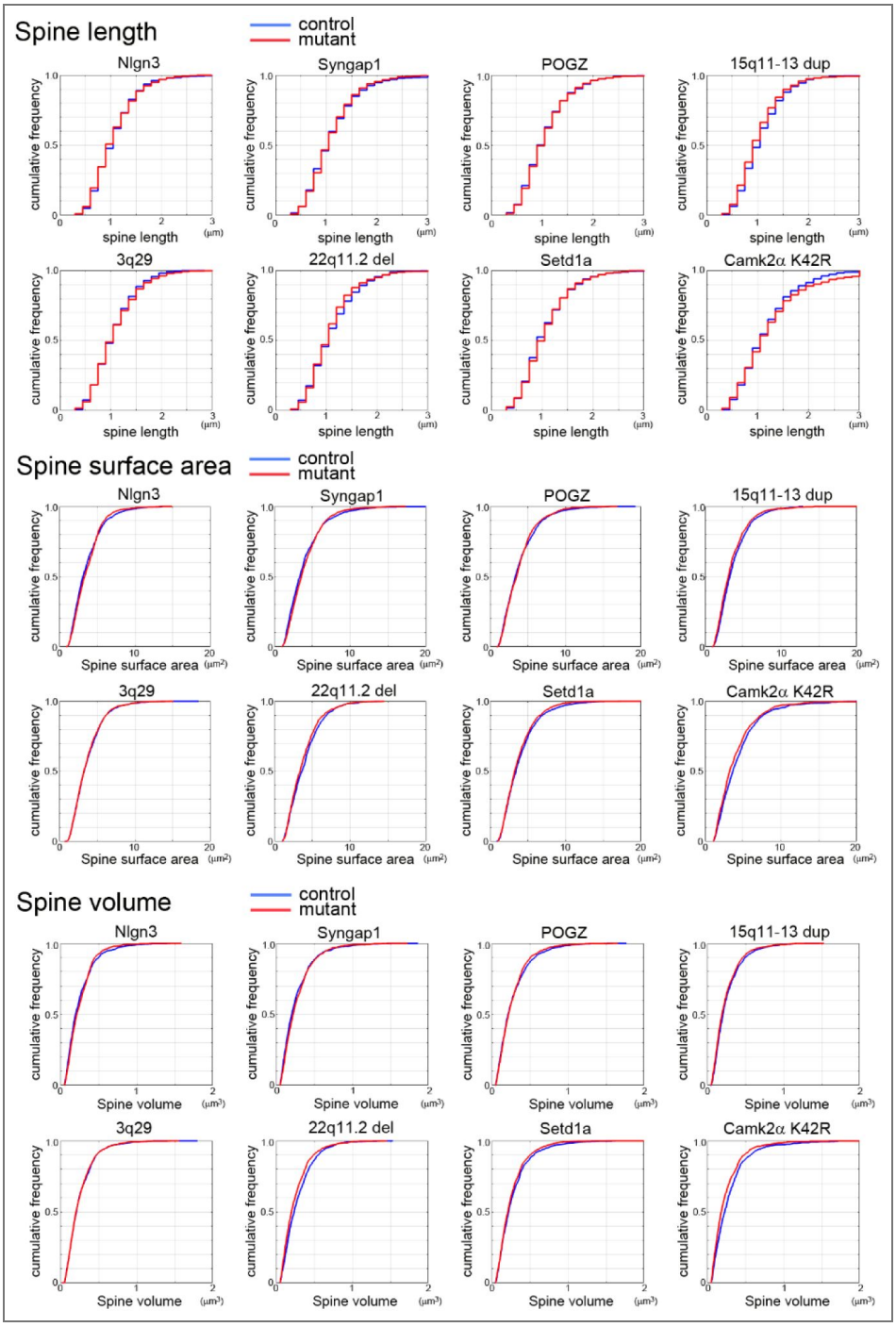

Supplementary Figure 2. Cumulative frequency plots of spine length, surface area, and volume for the eight mouse mutants: Nlgn3$^{R451C/(y\ or\ R451C)}$, Syngap1$^{+/-}$, POGZ$^{Q1038R/+}$, 15q11-13$^{dup/+}$, 3q29$^{del/+}$, 22q11.2$^{del/+}$, Setd1a$^{+/-}$, and CaMKIIα$^{K42R/K42R}$.

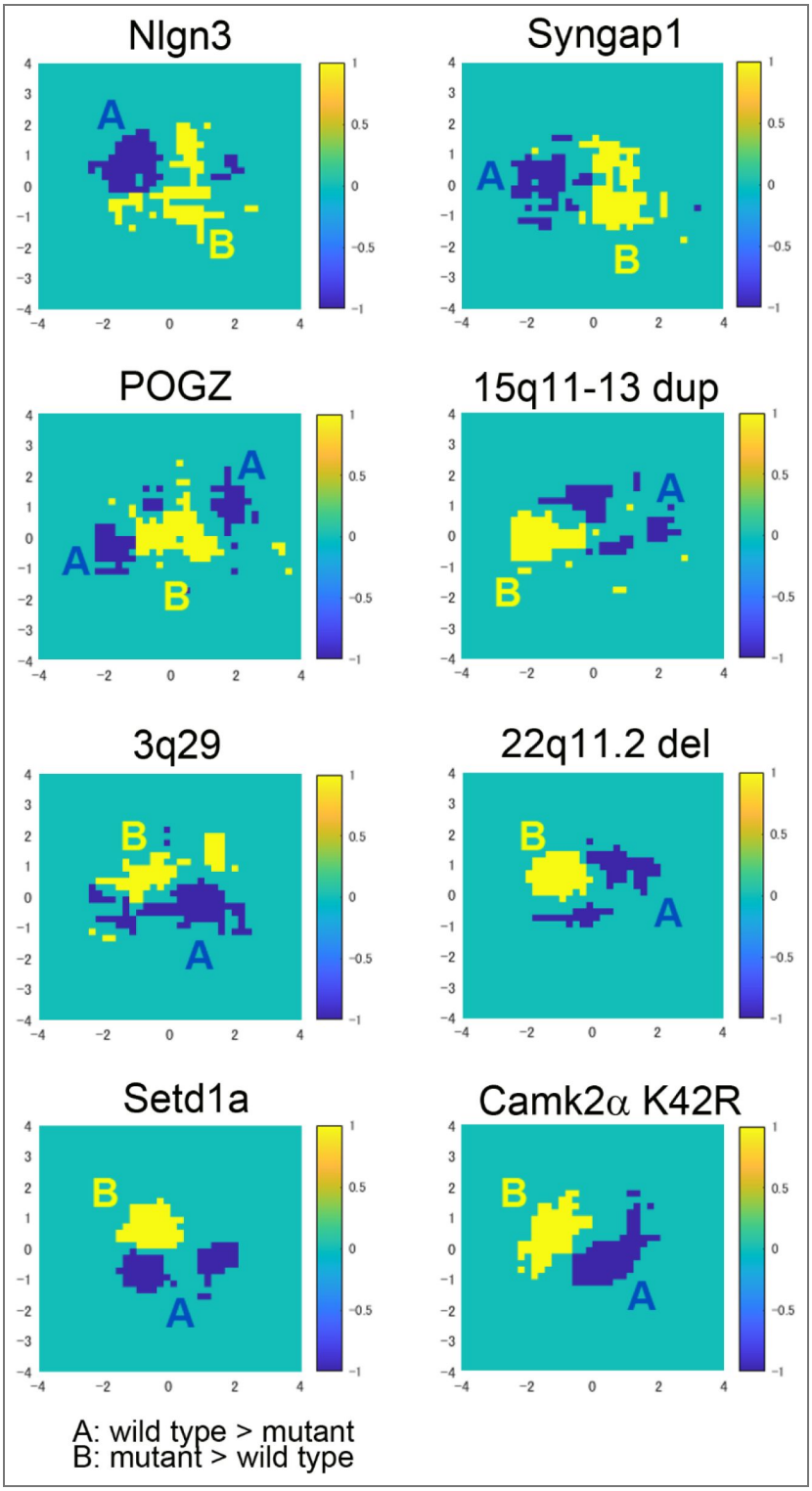

Supplementary Figure 3. Areas where control (A: blue) or mutant (B: yellow) spines show a higher density within the feature space of the PC1-PC2 plane.

The plots for all 8 mouse models are presented. The differences in population-level spine properties between ASD- and schizophrenia-associated mouse models were preserved within two groups. The areas enriched with mutant spines in Nlgn3$^{R451C/(y\ or\ R451C)}$, Syngap1$^{+/-}$, and POGZ$^{Q1038R/+}$ models were on the right side of the plot, suggesting the abundance of large spines in this group. In contrast, the areas enriched with mutant spines in 3q29$^{del/+}$, 22q11.2$^{del/+}$, Setd1a$^{+/-}$, and CaMKIIα$^{K42R/K42R}$ models were positioned on the left side of the plot, indicating the abundance of small spines.

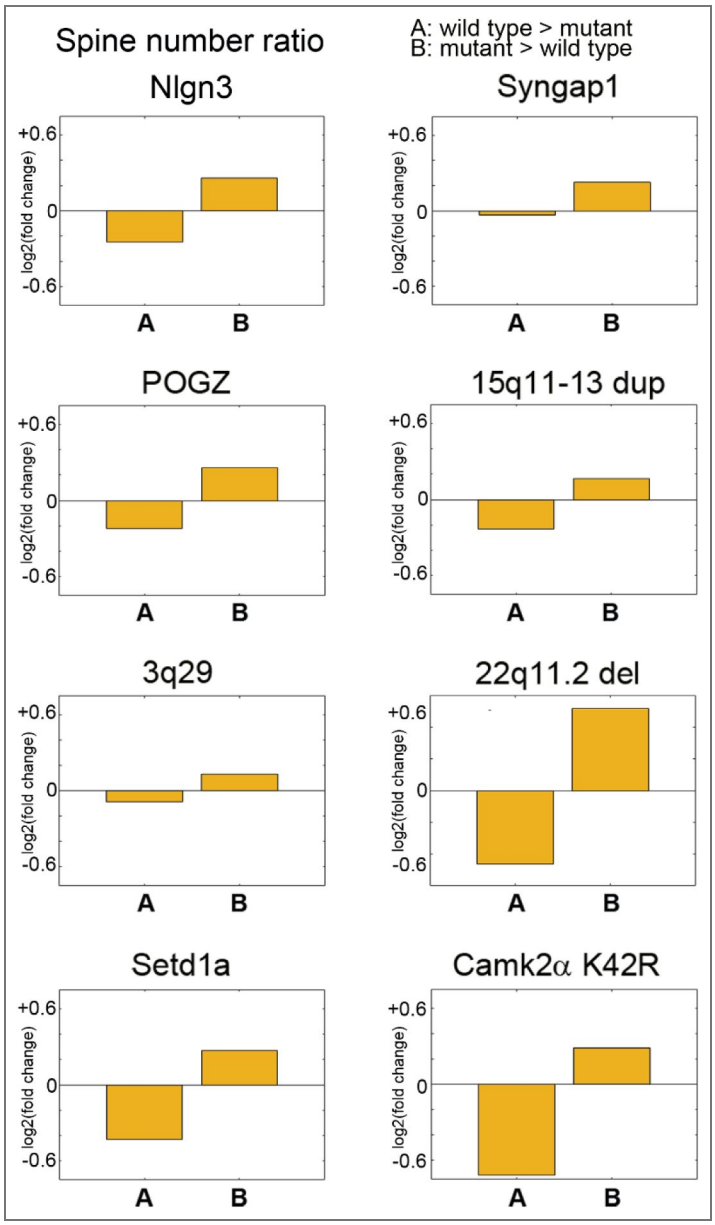

Supplementary Figure 4. The relative numbers of spines within areas A and B in the feature space from Supplementary Figure 3.

The densities of mutant spines were higher in area B than in area A.

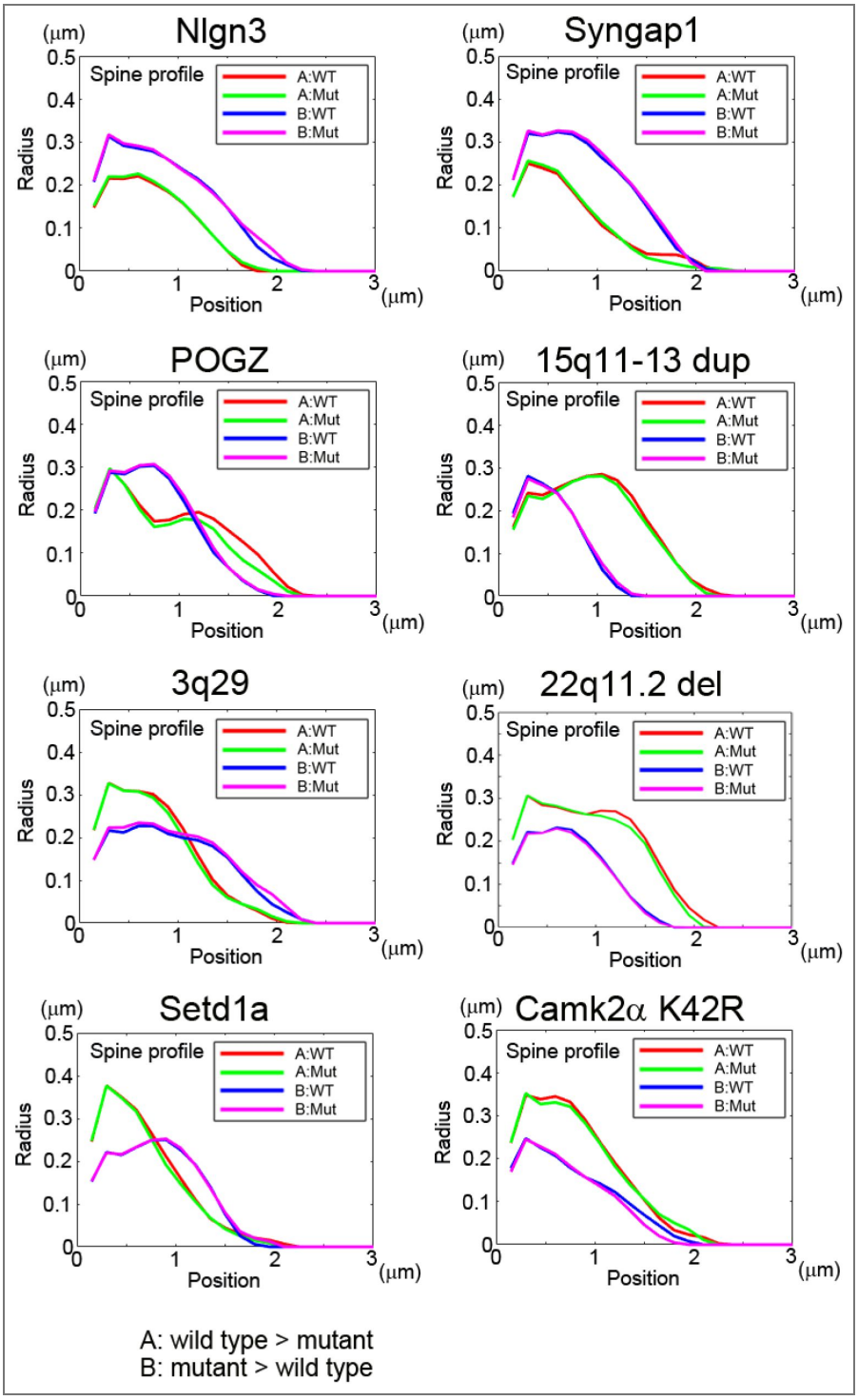

Supplementary Figure 5. Profiles of different spine populations (spines in the control-dominant area A and the mutant-dominant area B for both wild-type and mutant neurons) were visualized by plotting the radius along the long axis.

The numbers of control and mutant spines included in the analysis are as follows: Nlgn3$^{R451C/(y\ or\ R451C)}$, n = 775 in area A and n = 513 in area B; Syngap1$^{+/-}$, n = 668 in area A and n = 500 in area B; POGZ$^{Q1038R/+}$, n = 580 in area A and n = 815 in area B; 15q11-13$^{dup/+}$, n = 378 in area A and n = 797 in area B; 3q29$^{del/+}$, n = 627 in area A and n = 824 in area B; 22q11.2$^{del/+}$, n = 308 in area A and n = 575 in area B; Setd1a$^{+/-}$, n = 472 in area A and n = 808 in area B; CaMKIIα$^{K42R/K42R}$, n = 237 in area A and n = 634 in area B.

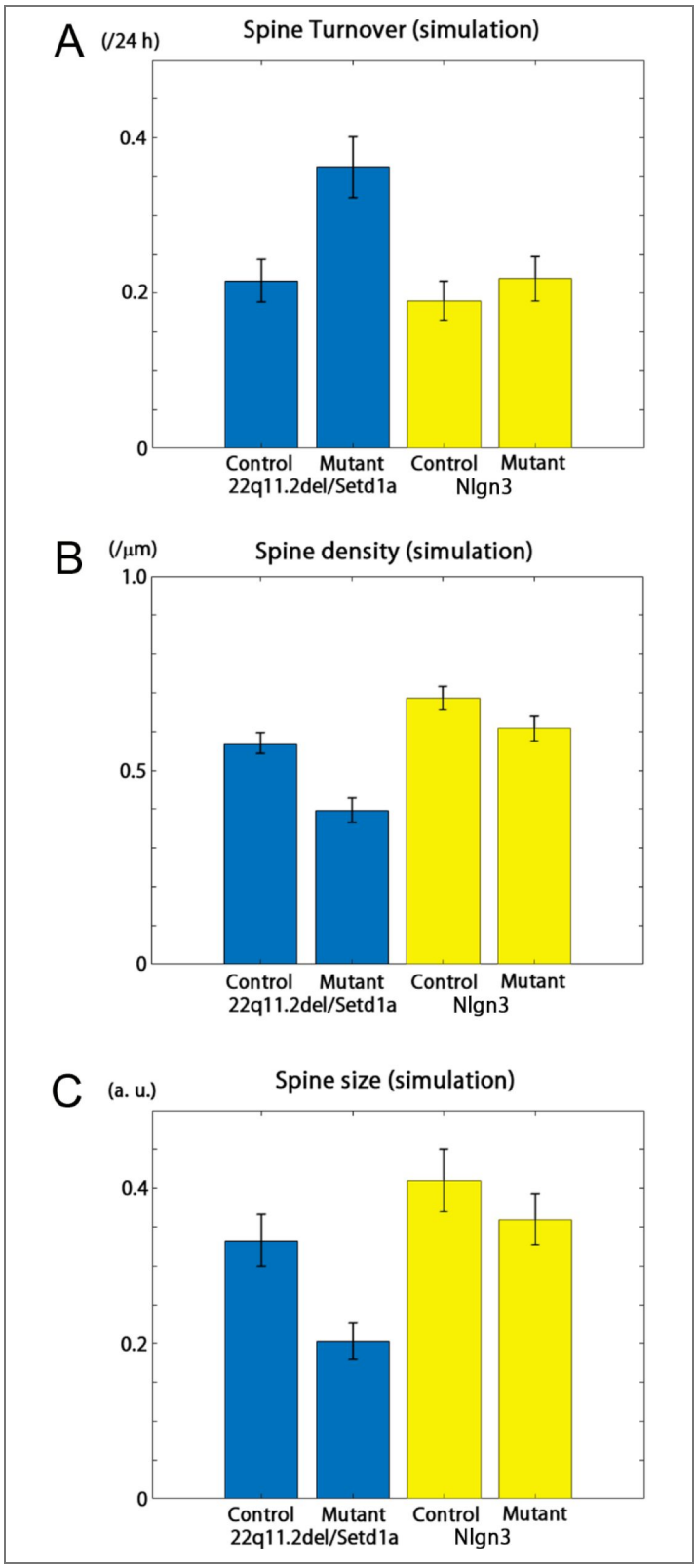

Supplementary Figure 6. Spine turnover (A), density (B), and size (C) from simulation data.

Simulation parameters were tuned to fit experimental results from control and mutant models. Means and standard deviations are shown.

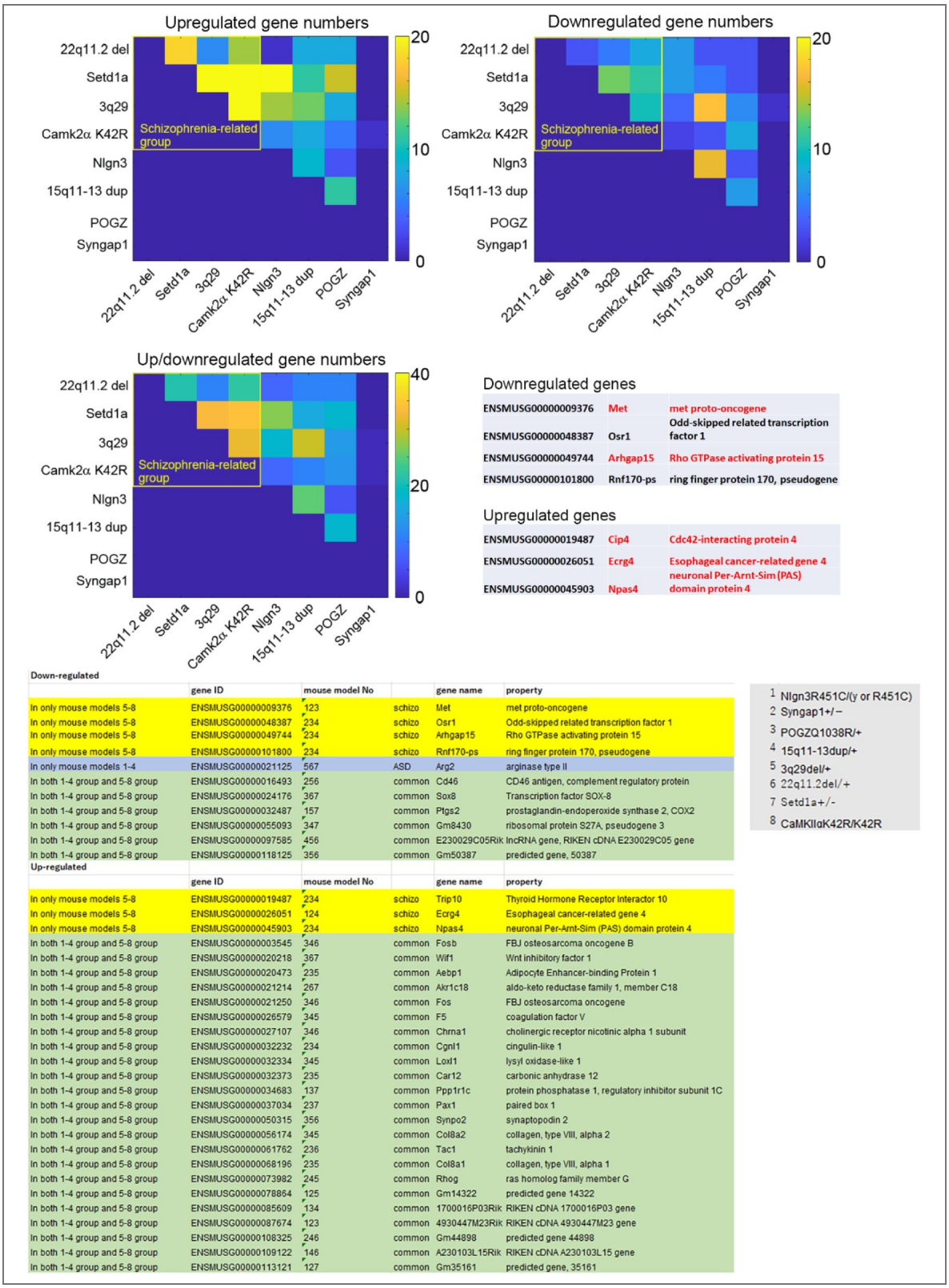

Downregulated genes

ENSMUSG00000009376	Met	met proto-oncogene
ENSMUSG00000048387	Osr1	Odd-skipped related transcription factor 1
ENSMUSG00000049744	Arhgap15	Rho GTPase activating protein 15
ENSMUSG00000101800	Rnf170-ps	ring finger protein 170, pseudogene

Upregulated genes

ENSMUSG00000019487	Cip4	Cdc42-interacting protein 4
ENSMUSG00000026051	Ecrg4	Esophageal cancer-related gene 4
ENSMUSG00000045903	Npas4	neuronal Per-Arnt-Sim (PAS) domain protein 4

Down-regulated

	gene ID	mouse model No		gene name	property
In only mouse models 5-8	ENSMUSG00000009376	123	schizo	Met	met proto-oncogene
In only mouse models 5-8	ENSMUSG00000048387	234	schizo	Osr1	Odd-skipped related transcription factor 1
In only mouse models 5-8	ENSMUSG00000049744	234	schizo	Arhgap15	Rho GTPase activating protein 15
In only mouse models 5-8	ENSMUSG00000101800	234	schizo	Rnf170-ps	ring finger protein 170, pseudogene
In only mouse models 1-4	ENSMUSG00000021125	567	ASD	Arg2	arginase type II
In both 1-4 group and 5-8 group	ENSMUSG00000016493	256	common	Cd46	CD46 antigen, complement regulatory protein
In both 1-4 group and 5-8 group	ENSMUSG00000024176	367	common	Sox8	Transcription factor SOX-8
In both 1-4 group and 5-8 group	ENSMUSG00000032487	157	common	Ptgs2	prostaglandin-endoperoxide synthase 2, COX2
In both 1-4 group and 5-8 group	ENSMUSG00000055093	347	common	Gm8430	ribosomal protein S27A, pseudogene 3
In both 1-4 group and 5-8 group	ENSMUSG00000097585	456	common	E230029C05Rik	lncRNA gene, RIKEN cDNA E230029C05 gene
In both 1-4 group and 5-8 group	ENSMUSG00000118125	356	common	Gm50387	predicted gene, 50387

Up-regulated

	gene ID	mouse model No		gene name	property
In only mouse models 5-8	ENSMUSG00000019487	234	schizo	Trip10	Thyroid Hormone Receptor Interactor 10
In only mouse models 5-8	ENSMUSG00000026051	124	schizo	Ecrg4	Esophageal cancer-related gene 4
In only mouse models 5-8	ENSMUSG00000045903	234	schizo	Npas4	neuronal Per-Arnt-Sim (PAS) domain protein 4
In both 1-4 group and 5-8 group	ENSMUSG00000003545	346	common	Fosb	FBJ osteosarcoma oncogene B
In both 1-4 group and 5-8 group	ENSMUSG00000020218	367	common	Wif1	Wnt inhibitory factor 1
In both 1-4 group and 5-8 group	ENSMUSG00000020473	235	common	Aebp1	Adipocyte Enhancer-binding Protein 1
In both 1-4 group and 5-8 group	ENSMUSG00000021214	267	common	Akr1c18	aldo-keto reductase family 1, member C18
In both 1-4 group and 5-8 group	ENSMUSG00000021250	346	common	Fos	FBJ osteosarcoma oncogene
In both 1-4 group and 5-8 group	ENSMUSG00000026579	345	common	F5	coagulation factor V
In both 1-4 group and 5-8 group	ENSMUSG00000027107	346	common	Chrna1	cholinergic receptor nicotinic alpha 1 subunit
In both 1-4 group and 5-8 group	ENSMUSG00000032232	234	common	Cgnl1	cingulin-like 1
In both 1-4 group and 5-8 group	ENSMUSG00000032334	345	common	Loxl1	lysyl oxidase-like 1
In both 1-4 group and 5-8 group	ENSMUSG00000032373	235	common	Car12	carbonic anhydrase 12
In both 1-4 group and 5-8 group	ENSMUSG00000034683	137	common	Ppp1r1c	protein phosphatase 1, regulatory inhibitor subunit 1C
In both 1-4 group and 5-8 group	ENSMUSG00000037034	237	common	Pax1	paired box 1
In both 1-4 group and 5-8 group	ENSMUSG00000050315	356	common	Synpo2	synaptopodin 2
In both 1-4 group and 5-8 group	ENSMUSG00000056174	345	common	Col8a2	collagen, type VIII, alpha 2
In both 1-4 group and 5-8 group	ENSMUSG00000061762	236	common	Tac1	tachykinin 1
In both 1-4 group and 5-8 group	ENSMUSG00000068196	235	common	Col8a1	collagen, type VIII, alpha 1
In both 1-4 group and 5-8 group	ENSMUSG00000073982	245	common	Rhog	ras homolog family member G
In both 1-4 group and 5-8 group	ENSMUSG00000078864	125	common	Gm14322	predicted gene 14322
In both 1-4 group and 5-8 group	ENSMUSG00000085609	134	common	1700016P03Rik	RIKEN cDNA 1700016P03 gene
In both 1-4 group and 5-8 group	ENSMUSG00000087674	123	common	4930447M23Rik	RIKEN cDNA 4930447M23 gene
In both 1-4 group and 5-8 group	ENSMUSG00000108325	246	common	Gm44898	predicted gene 44898
In both 1-4 group and 5-8 group	ENSMUSG00000109122	146	common	A230103L15Rik	RIKEN cDNA A230103L15 gene
In both 1-4 group and 5-8 group	ENSMUSG00000113121	127	common	Gm35161	predicted gene, 35161

1 Nlgn3R451C/(y or R451C)
2 Syngap1+/−
3 POGZQ1038R/+
4 15q11-13dup/+
5 3q29del/+
6 22q11.2del/+
7 Setd1a+/-
8 CaMKIIαK42R/K42R

Supplementary Figure 7. Pseudocolor presentation of differentially expressed genes (DEGs) between mutant and corresponding control mice.

The number of shared DEGs was higher in the schizophrenia-related mouse models than in the ASD-related mouse models. Mouse gene identifiers (ENSMUSG) and gene names for DEGs shared by three or four schizophrenia-associated mouse models and not differentially expressed in ASD-associated mouse models are presented. DEGs analyzed for their effects on spines are shown in red. Color indicates the number of DEGs. The lower table shows all DEGs shared by three or four mouse models, irrespective of their grouping as ASD-related or schizophrenia-related.

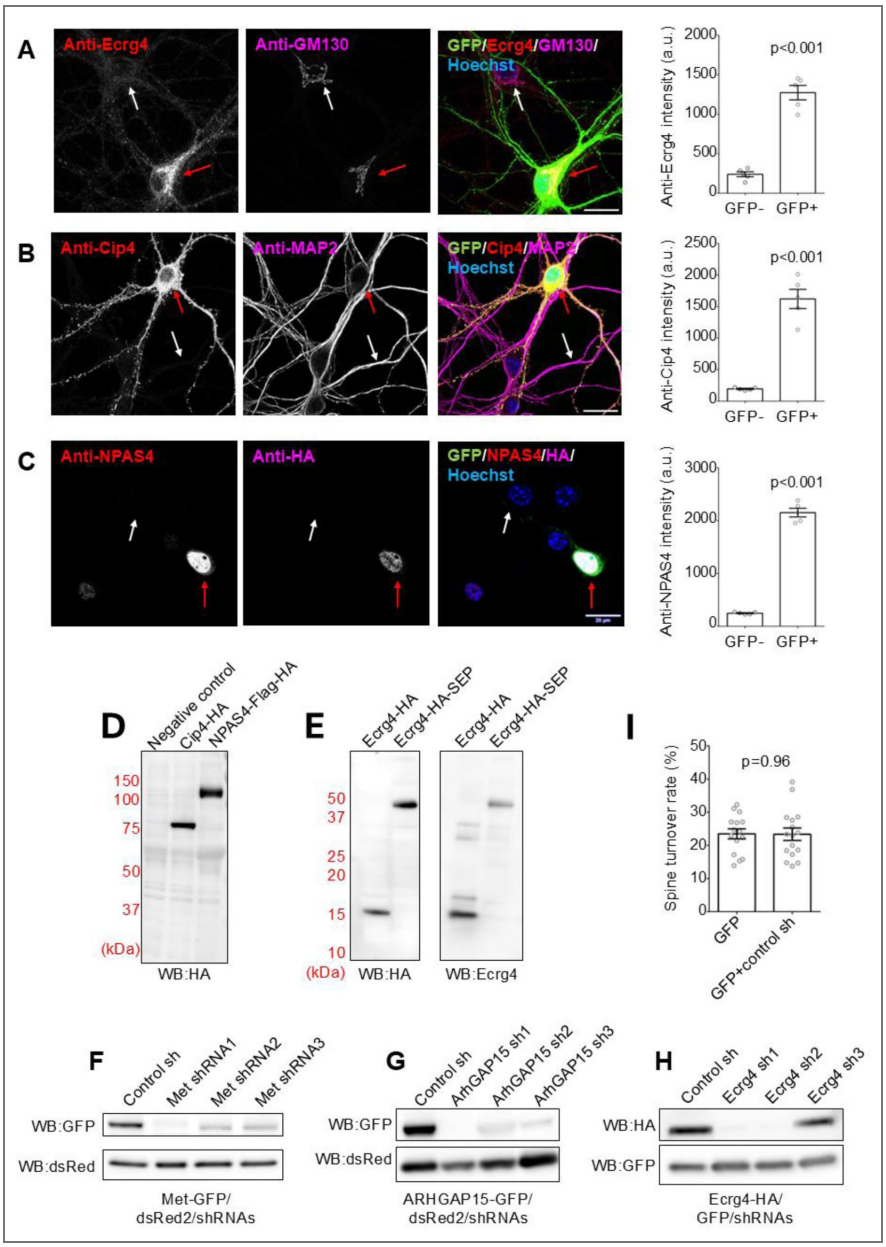

Supplementary Figure 8.

(A-C) Validation of overexpressed tagged constructs by immunocytochemistry in hippocampal neurons. Bar = 20 μm. The data are presented as mean ± SEM (N = 5 neurons each). Red allows; transfected neurons, white arrows; non-transfected neurons. (A) Immunocytochemistry of hippocampal neurons expressing Ecrg4-HA with GFP using anti-Ecrg4 antibody. Anti-GM130 antibody staining detected the Golgi apparatus. (B) Immunocytochemistry of hippocampal neurons expressing Cip4-HA with GFP using anti-Cip4 antibody. Anti-MAP2 antibody detected neuronal dendrites. (C) Anti-NPAS4 and anti-HA immunocytochemistry of hippocampal neurons expressing NPAS4-Flag-HA with GFP. (D-E) Immunoblot verification of tagged construct expression in COS-7 cells. (D) Immunoblotting in total cell lysate from COS-7 cells expressing Cip4-HA or NPAS4-Flag-HA. The estimated molecular weights of Cip4-HA and NPAS4-Flag-HA are 64 kDa and 89 kDa, respectively. (E) Immunoblotting using both anti-HA and anti-Ecrg4 in total cell lysate from COS-7 cells expressing Ecrg4-HA or Ecrg4-HA-SEP. The estimated molecular weights of Ecrg4, Ecrg4-HA, and Ecrg4-HA-SEP are 17 kDa, 18 kDa, and 45 kDa, respectively. (F-H) Verification of knock-down effects of shRNAs by immunoblotting of COS-7 cells. Immunoblotting in total cell lysates from COS-7 cells transfected with the expression vectors of either Met-GFP (F), ArhGAP15-GFP (G), or Ecrg4-HA (H), together with dsRed2 and shRNAs targeting the corresponding transcripts. (I) Measurement of spine turnover rate in neurons transfected with a control shRNA construct together with GFP expression vectors. For the experimental control, we used neurons transfected only with GFP. The data are presented as mean ± SEM (n = 15 dendrites from 9 neurons for GFP control, n = 16 dendrites from 8 neurons for GFP plus control shRNA).

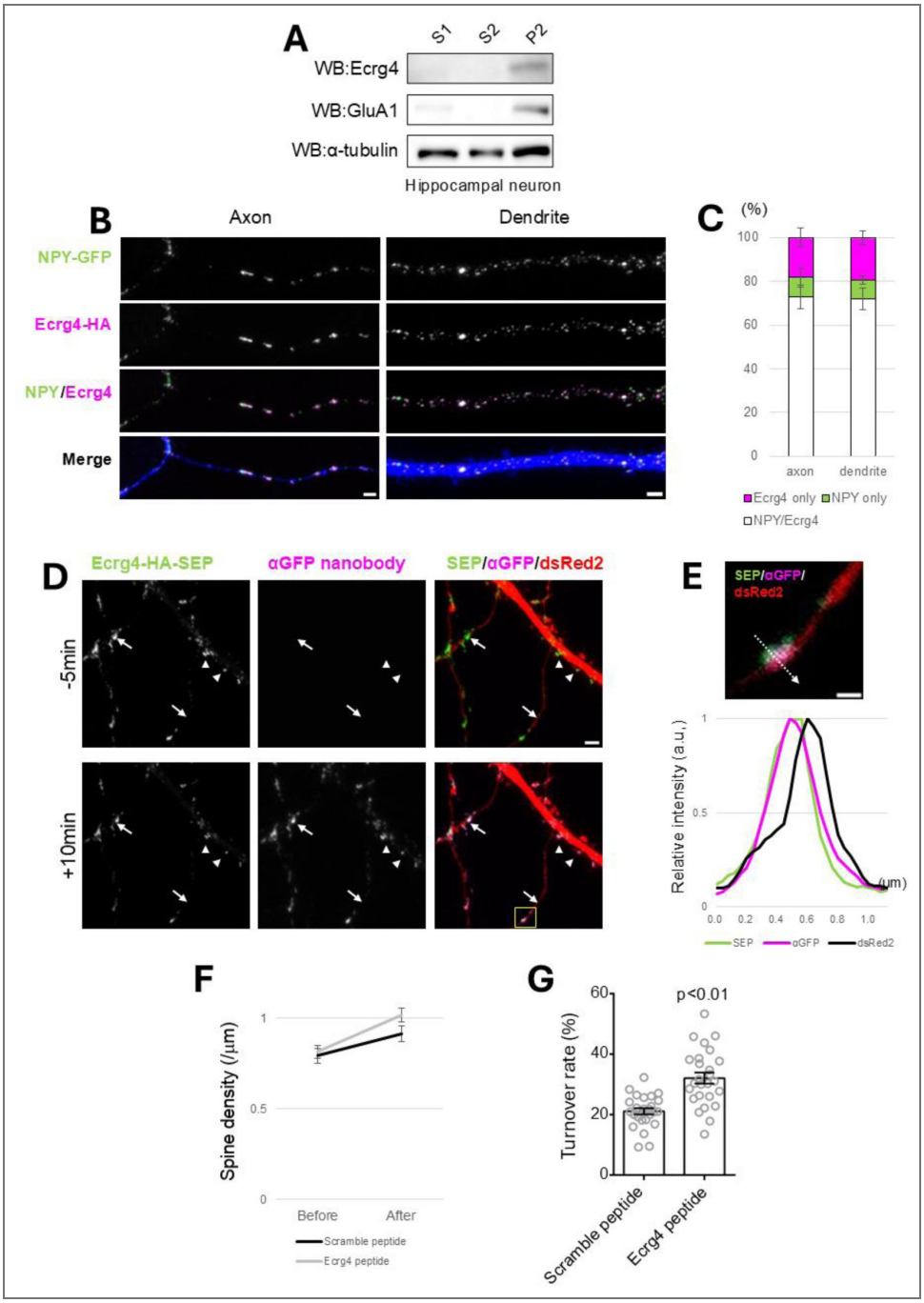

Supplementary Figure 9. Expression and distribution of Ecrg4 in cultured hippocampal neurons.

(A) Preferential localization of Ecrg4 protein in the membrane fraction. Immunoblotting of Ecrg4, GluA1AMPA-type glutamate receptor, and α-tubulin in the remaining fraction after removal of nuclei (S1), supernatant after centrifugation (S2), and resulting pellet (P2). (B) Images of an immunostained hippocampal neuron expressing HA-tagged Ecrg4 and NPY-GFP. The fluorescence signals were partially colocalized, suggesting Ecrg4 protein accumulation in dense-core vesicles. Bar = 2 μm. (C) Quantification of the overlap between puncta immunopositive for HA-tagged Ecrg4 and NPY-GFP. N = 4 cells from 1 dish. (D) Surface labeling with the anti-GFP nanobody revealing clusters of SEP-tagged Ecrg4 in dsRed2-positive axons (arrows) and dendrites (arrowheads). A nanobody was applied at time t = 0 min. Bar = 2 μm. (E) Enlarged image of a single Ecrg4 puncta in the axon, marked by a yellow square in (D), with the fluorescence intensity profile along the dashed arrow. Bar = 0.5 μm. (F) The spine density of cultured hippocampal neurons 24 hours after administration of either Ecrg4 peptides or scrambled peptides (n = 26 dendrites and 13 neurons for each condition). (G) Spine turnover rate of neurons treated with Ecrg4 peptides or scrambled peptides (n = 26 dendrites and 13 neurons for each condition).

Data availability

The original code for SIM image processing is available at *https://shigeookabe.github.io/download-page-SIM/* with a password of "simspineimage". Supplementary Tables 2 and 3 contain the data for differentially expressed genes (DEGs).

Acknowledgements

We thank Toru Takumi for the 15q11-13$^{dup/+}$ mice, Katsuhiko Tabuchi for Nlgn3$^{R451C/(y\ or\ R451C)}$ mice, Yoko Yamagata for CaMKIIα$^{K42R/K42R}$ mice, and Justin Taraska for the NPY tagged with GFP. This work was supported by Grants-in-Aid for Scientific Research (25H01038, 20H00481, 20H05894, 20H05895 to S.O.), the Japan Agency for Medical Research and Development (JP19gm1310003 to S.O., T. N., and Y. G., JP22jm0210097, JP25wm0625001h0003 to S.O., JP19dm0207071 to A. A.), the Naito Foundation, and the Uehara Memorial Foundation.

Additional information

Author contributions

Y.K. and S.O. conceived of the project and designed the methodology. Y.K. and Q.L. performed the experiments. R. S., A.A. and T.N. provided the animal resources and provided advice on analysis. Y.G. conducted the gene expression analysis. S.O. and Y.K. wrote the manuscript, with contributions from A.A., T.N., and Y.G.

Declarations of generative AI and AI-assisted technologies in the writing process

The authors utilized Grammarly (*https://app.grammarly.com/*) for editing the text. The authors take full responsibility for the contents of the manuscript.

Resource availability

The original code for SIM image processing is available at *https://shigeookabe.github.io/download-page-SIM/* with a password of “simspineimage”.

Funding

Funder	Grant reference number	Author
Ministry of Education, Culture, Sports, Science and Technology (MEXT)	25H01038	Shigeo Okabe
Ministry of Education, Culture, Sports, Science and Technology (MEXT)	20H00481	Shigeo Okabe
Ministry of Education, Culture, Sports, Science and Technology (MEXT)	20H05894	Shigeo Okabe
Ministry of Education, Culture, Sports, Science and Technology (MEXT)	20H05895	Shigeo Okabe
Japan Agency for Medical Research and Development (AMED)	JP19gm1310003	Shigeo Okabe Yasuhiro Go Takanobu Nakazawa Atsu Aiba
Japan Agency for Medical Research and Development (AMED)	JP22jm0210097	Shigeo Okabe
Japan Agency for Medical Research and Development (AMED)	JP25wm0625001h0003	Shigeo Okabe

Author ORCID iDs

Atsu Aiba: https://orcid.org/0000-0002-8192-0778
Shigeo Okabe: https://orcid.org/0000-0003-1216-8890

Additional files

Supplementary Table 1.

Supplementary Table 2.

Supplementary Table 3.

References

1. **Rochefort N.L.,** Konnerth A (2012) Dendritic spines: from structure to in vivo function. *EMBO Rep* **13**:699-708 https://doi.org/10.1038/EMBOR.2012.102 | PubMed
2. **Sala C.,** Segal M (2014) Dendritic spines: the locus of structural and functional plasticity. *Physiol. Rev* **94**:141-188 https://doi.org/10.1152/physrev.00012.2013 | PubMed
3. **Matsuzaki M.,** Ellis-Davies G.C.R., Nemoto T., Miyashita Y., Iino M., Kasai H (2001) Dendritic spine geometry is critical for AMPA receptor expression in hippocampal CA1 pyramidal neurons. *Nat. Neurosci* **4**:1086-1092 https://doi.org/10.1038/NN736 | PubMed
4. **Matsuzaki M.,** Honkura N., Ellis-Davies G.C.R., Kasai H (2004) Structural basis of long-term potentiation in single dendritic spines. *Nature* **429**:761-766 https://doi.org/10.1038/nature02617 | PubMed
5. **Nägerl U.V.,** Eberhorn N., Cambridge S.B., Bonhoeffer T (2004) Bidirectional activity-dependent morphological plasticity in hippocampal neurons. *Neuron* **44**:759-767 https://doi.org/10.1016/j.neuron.2004.11.016 | PubMed
6. **Zhou Q.,** Homma K.J., Poo M.M (2004) Shrinkage of dendritic spines associated with long-term depression of hippocampal synapses. *Neuron* **44**:749-757 https://doi.org/10.1016/j.neuron.2004.11.011 | PubMed
7. **Loewenstein Y.,** Kuras A., Rumpel S (2011) Multiplicative dynamics underlie the emergence of the log-normal distribution of spine sizes in the neocortex in vivo. *Journal of Neuroscience* **31**:9481-9488 https://doi.org/10.1523/JNEUROSCI.6130-10.2011 | PubMed
8. **Loewenstein Y.,** Yanover U., Rumpel S (2015) Predicting the dynamics of network connectivity in the neocortex. *Journal of Neuroscience* **35**:12535-12544 https://doi.org/10.1523/JNEUROSCI.2917-14.2015 | PubMed
9. **Statman A.,** Kaufman M., Minerbi A., Ziv N.E., Brenner N (2014) Synaptic size dynamics as an effectively stochastic process. *PLoS Comput. Biol* **10** https://doi.org/10.1371/JOURNAL.PCBI.1003846 | PubMed
10. **Hazan L.,** Ziv N.E (2020) Activity dependent and independent determinants of synaptic size diversity. *J. Neurosci* **40**:2828-2848 https://doi.org/10.1523/JNEUROSCI.2181-19.2020 | PubMed
11. **Tønnesen J.,** Katona G., Rózsa B., Nägerl U.V (2014) Spine neck plasticity regulates compartmentalization of synapses. *Nat. Neurosci* **17**:678-685 https://doi.org/10.1038/nn.3682 | PubMed
12. **Kashiwagi Y.,** Higashi T., Obashi K., Sato Y., Komiyama N.H., Grant S.G.N., Okabe S (2019) Computational geometry analysis of dendritic spines by structured illumination microscopy. *Nat. Commun* **10**:1285 https://doi.org/10.1038/s41467-019-09337-0 | PubMed
13. **Zaccard C.R.,** Shapiro L., Martin-de-Saavedra M.D., Pratt C., Myczek K., Song A., Forrest M.P., Penzes P (2020) Rapid 3D enhanced resolution microscopy reveals diversity in dendritic spinule dynamics, regulation, and function. *Neuron* **107**:522-537 https://doi.org/10.1016/j.neuron.2020.04.025 | PubMed
14. **Penzes P.,** Cahill M.E., Jones K.A., VanLeeuwen J.-E., Woolfrey K.M (2011) Dendritic spine pathology in neuropsychiatric disorders. *Nat. Neurosci* **14**:285-293 https://doi.org/10.1038/nn.2741 | PubMed

15. **Fromer M.,** Pocklington A.J., Kavanagh D.H., Williams H.J., Dwyer S., Gormley P., Georgieva L., Rees E., Palta P., Ruderfer D.M., *et al.* (2014) De novo mutations in schizophrenia implicate synaptic networks. *Nature* **506**:179-184 https://doi.org/10.1038/NATURE12929 | PubMed

16. **Rodriguez-Murillo L.,** Gogos J.A., Karayiorgou M (2012) The genetic architecture of schizophrenia: new mutations and emerging paradigms. *Annu. Rev. Med* **63**:63-80 https://doi.org/10.1146/ANNUREV-MED-072010-091100 | PubMed

17. **Gulsuner S.,** Walsh T., Watts A.C., Lee M.K., Thornton A.M., Casadei S., Rippey C., Shahin H., Nimgaonkar V.L., Go R.C.P., *et al.* (2013) Spatial and temporal mapping of de novo mutations in schizophrenia to a fetal prefrontal cortical network. *Cell* **154**:518-529 https://doi.org/10.1016/J.CELL.2013.06.049 | PubMed

18. **Bourgeron T** (2015) From the genetic architecture to synaptic plasticity in autism spectrum disorder. *Nat. Rev. Neurosci* **16**:551-563 https://doi.org/10.1038/NRN3992 | PubMed

19. **Terashima H.,** Minatohara K., Maruoka H., Okabe S (2022) Imaging neural circuit pathology of autism spectrum disorders: autism-associated genes, animal models and the application of in vivo two-photon imaging. *Microscopy (Oxf)* **71**:I81-I99 https://doi.org/10.1093/JMICRO/DFAB039 | PubMed

20. **Zieger H.L.,** Choquet D (2021) Nanoscale synapse organization and dysfunction in neurodevelopmental disorders. *Neurobiol. Dis* **158**:105453 https://doi.org/10.1016/J.NBD.2021.105453 | PubMed

21. **Yilmaz M.,** Yalcin E., Presumey J., Aw E., Ma M., Whelan C.W., Stevens B., McCarroll S.A., Carroll M.C (2021) Overexpression of schizophrenia susceptibility factor human complement C4A promotes excessive synaptic loss and behavioral changes in mice. *Nat. Neurosci* **24**:214-224 https://doi.org/10.1038/S41593-020-00763-8 | PubMed

22. **Obi-Nagata K.,** Suzuki N., Miyake R., MacDonald M.L., Fish K.N., Ozawa K., Nagahama K., Okimura T., Tanaka S., Kano M., *et al.* (2023) Distorted neurocomputation by a small number of extra-large spines in psychiatric disorders. *Sci. Adv* **9**:eade5973 https://doi.org/10.1126/SCIADV.ADE5973 | PubMed

23. **Mukai J.,** Dhilla A., Drew L.J., Stark K.L., Cao L., MacDermott A.B., Karayiorgou M., Gogos J.A (2008) Palmitoylation-dependent neurodevelopmental deficits in a mouse model of 22q11 microdeletion. *Nat. Neurosci* **11**:1302-1310 https://doi.org/10.1038/nn.2204 | PubMed

24. **Nakai N.,** Takumi T., Nakai J., Sato M (2018) Common defects of spine dynamics and circuit function in neurodevelopmental disorders: A systematic review of findings from in vivo optical imaging of mouse models. *Front. Neurosci* **12** https://doi.org/10.3389/FNINS.2018.00412 | PubMed

25. **Shcheglovitov A.,** Shcheglovitova O., Yazawa M., Portmann T., Shu R., Sebastiano V., Krawisz A., Froehlich W., Bernstein J.A., Hallmayer J.F., *et al.* (2013) SHANK3 and IGF1 restore synaptic deficits in neurons from 22q13 deletion syndrome patients. *Nature* **503**:267-271 https://doi.org/10.1038/NATURE12618 | PubMed

26. **Llamosas N.,** Arora V., Vij R., Kilinc M., Bijoch L., Rojas C., Reich A., Sridharan B.P., Willems E., Piper D.R., *et al.* (2020) SYNGAP1 controls the maturation of dendrites, synaptic function, and network activity in developing human neurons. *J. Neurosci* **40**:7980-7994 https://doi.org/10.1523/JNEUROSCI.1367-20.2020 | PubMed

27. **Yamamoto K.,** Kuriu T., Matsumura K., Nagayasu K., Tsurusaki Y., Miyake N., Yamamori H., Yasuda Y., Fujimoto M., Fujiwara M., *et al.* (2021) Multiple alterations in glutamatergic transmission and dopamine D2 receptor splicing in induced pluripotent stem cell-derived neurons from patients with familial schizophrenia. *Transl. Psychiatry* **11**:548 https://doi.org/10.1038/S41398-021-01676-1 | PubMed

28. **Wen Z.,** Nguyen H.N., Guo Z., Lalli M.A., Wang X., Su Y., Kim N.S., Yoon K.J., Shin J., Zhang C., *et al.* (2014) Synaptic dysregulation in a human iPS cell model of mental disorders. *Nature* **515**:414-418 https://doi.org/10.1038/NATURE13716 | PubMed

29. **Chisholm K.,** Lin A., Abu-Akel A., Wood S.J (2015) The association between autism and schizophrenia spectrum disorders: A review of eight alternate models of co-occurrence. *Neurosci. Biobehav. Rev* **55**:173-183 https://doi.org/10.1016/J.NEUBIOREV.2015.04.012 | PubMed

30. **De Crescenzo F.,** Postorino V., Siracusano M., Riccioni A., Armando M., Curatolo P., Mazzone L. (2019) Autistic symptoms in schizophrenia spectrum disorders: A systematic review and meta-analysis. *Front. Psychiatry* **10** https://doi.org/10.3389/FPSYT.2019.00078 | PubMed

31. **Nenadić I.,** Meller T., Evermann U., Schmitt S., Pfarr J.K., Abu-Akel A., Grezellschak S (2021) Subclinical schizotypal vs. autistic traits show overlapping and diametrically opposed facets in a non-clinical population. *Schizophr. Res* **231**:32-41 https://doi.org/10.1016/J.SCHRES.2021.02.018 | PubMed

32. **Crespi B.,** Badcock C (2008) Psychosis and autism as diametrical disorders of the social brain. *Behav. Brain Sci* **31**:241-261 https://doi.org/10.1017/S0140525X08004214 | PubMed

33. **Pratt J.,** Winchester C., Dawson N., Morris B (2012) Advancing schizophrenia drug discovery: optimizing rodent models to bridge the translational gap. *Nat. Rev. Drug Discov* **11**:560-570 https://doi.org/10.1038/NRD3649 | PubMed

34. **Isshiki M.,** Tanaka S., Kuriu T., Tabuchi K., Takumi T., Okabe S (2014) Enhanced synapse remodelling as a common phenotype in mouse models of autism. *Nat. Commun* **5**:4742 https://doi.org/10.1038/ncomms5742 | PubMed

35. **Lee E.,** Lee J., Kim E (2017) Excitation/inhibition imbalance in animal models of autism spectrum disorders. *Biol. Psychiatry* **81**:838-847 https://doi.org/10.1016/J.BIOPSYCH.2016.05.011 | PubMed

36. **Tabuchi K.,** Blundell J., Etherton M.R., Hammer R.E., Liu X., Powell C.M., Südhof T.C (2007) A neuroligin-3 mutation implicated in autism increases inhibitory synaptic transmission in mice. *Science* **318**:71-76 https://doi.org/10.1126/science.1146221 | PubMed

37. **Etherton M.,** Földy C., Sharma M., Tabuchi K., Liu X., Shamloo M., Malenka R.C., Südhof T.C (2011) Autism-linked neuroligin-3 R451C mutation differentially alters hippocampal and cortical synaptic function. *Proc. Natl. Acad. Sci. U. S. A* **108**:13764-13769 https://doi.org/10.1073/pnas.1111093108 | PubMed

38. **Komiyama N.H.,** Watabe A.M., Carlisle H.J., Porter K., Charlesworth P., Monti J., Strathdee D.J.C., O'Carroll C.M., Martin S.J., Morris R.G.M., *et al.* (2002) SynGAP regulates ERK/MAPK signaling, synaptic plasticity, and learning in the complex with postsynaptic density 95 and NMDA receptor. *The Journal of Neuroscience* **22**:9721-9732 https://doi.org/10.1523/jneurosci.22-22-09721.2002 | PubMed

39. **Matsumura K.,** Seiriki K., Okada S., Nagase M., Ayabe S., Yamada I., Furuse T., Shibuya H., Yasuda Y., Yamamori H., *et al.* (2020) Pathogenic POGZ mutation causes impaired cortical development and reversible autism-like phenotypes. *Nat. Commun* **11**:859 https://doi.org/10.1038/s41467-020-14697-z | PubMed

40. **Nakatani J.,** Tamada K., Hatanaka F., Ise S., Ohta H., Inoue K., Tomonaga S., Watanabe Y., Chung Y.J., Banerjee R., *et al.* (2009) Abnormal behavior in a chromosome- engineered mouse model for human 15q11-13 duplication seen in autism. *Cell* **137**:1235-1246 https://doi.org/10.1016/j.cell.2009.04.024 | PubMed

41. **Baba M.,** Yokoyama K., Seiriki K., Naka Y., Matsumura K., Kondo M., Yamamoto K., Hayashida M., Kasai A., Ago Y., *et al.* (2019) Psychiatric-disorder-related behavioral phenotypes and cortical hyperactivity in a mouse model of 3q29 deletion syndrome. *Neuropsychopharmacology* **44**:2125-2135 https://doi.org/10.1038/s41386-019-0441-5 | PubMed

42. **Saito R.,** Miyoshi C., Koebis M., Kushima I., Nakao K., Mori D., Ozaki N., Funato H., Yanagisawa M., Aiba A (2021) Two novel mouse models mimicking minor deletions in 22q11.2 deletion syndrome revealed the contribution of each deleted region to psychiatric disorders. *Mol. Brain* **14** https://doi.org/10.1186/S13041-021-00778-7 | PubMed

43. **Nagahama K.,** Sakoori K., Watanabe T., Kishi Y., Kawaji K., Koebis M., Nakao K., Gotoh Y., Aiba A., Uesaka N., *et al.* (2020) Setd1a insufficiency in mice attenuates excitatory synaptic function and recapitulates schizophrenia-related behavioral abnormalities. *Cell Rep* **32**:108126 https://doi.org/10.1016/J.CELREP.2020.108126 | PubMed

44. **Yamagata Y.,** Kobayashi S., Umeda T., Inoue A., Sakagami H., Fukaya M., Watanabe M., Hatanaka N., Totsuka M., Yagi T., *et al.* (2009) Kinase-dead knock-in mouse reveals an essential role of kinase activity of Ca^{2+}/calmodulin-dependent protein kinase IIα in dendritic spine enlargement, long-term

potentiation, and learning. *Journal of Neuroscience* **29**:7607-7618 https://doi.org/10.1523/JNEUROSCI.0707-09.2009 | PubMed

45. **Yamasaki N.,** Maekawa M., Kobayashi K., Kajii Y., Maeda J., Soma M., Takao K., Tanda K., Ohira K., Toyama K., *et al.* (2008) Alpha-CaMKII deficiency causes immature dentate gyrus, a novel candidate endophenotype of psychiatric disorders. *Mol. Brain* **1**:6 https://doi.org/10.1186/1756-6606-1-6 | PubMed

46. **Featherstone R.E.,** Shimada T., Crown L.M., Melnychenko O., Yi J., Matsumoto M., Tajinda K., Mihara T., Adachi M., Siegel S.J (2022) Calcium/calmodulin-dependent protein kinase IIα heterozygous knockout mice show electroencephalogram and behavioral changes characteristic of a subpopulation of schizophrenia and intellectual impairment. *Neuroscience* **499**:104-117 https://doi.org/10.1016/J.NEUROSCIENCE.2022.07.023 | PubMed

47. **Stephenson J.R.,** Wang X., Perfitt T.L., Parrish W.P., Shonesy B.C., Marks C.R., Mortlock D.P., Nakagawa T., Sutcliffe J.S., Colbran R.J (2017) A Novel Human CAMK2A Mutation Disrupts Dendritic Morphology and Synaptic Transmission, and Causes ASD-Related Behaviors. *J. Neurosci* **37**:2216-2233 https://doi.org/10.1523/JNEUROSCI.2068-16.2017 | PubMed

48. **Brown C.N.,** Cook S.G., Allen H.F., Crosby K.C., Singh T., Coultrap S.J., Bayer K.U (2021) Characterization of six CaMKIIα variants found in patients with schizophrenia. *iScience* **24** https://doi.org/10.1016/j.isci.2021.103184 | PubMed

49. **Qiu S.,** Lu Z., Levitt P (2014) MET receptor tyrosine kinase controls dendritic complexity, spine morphogenesis, and glutamatergic synapse maturation in the hippocampus. *J. Neurosci* **34**:16166-16179 https://doi.org/10.1523/JNEUROSCI.2580-14.2014 | PubMed

50. **Bloodgood B.L.,** Sharma N., Browne H.A., Trepman A.Z., Greenberg M.E (2013) The activity-dependent transcription factor NPAS4 regulates domain-specific inhibition. *Nature* **503**:121-125 https://doi.org/10.1038/nature12743 | PubMed

51. **Spiegel I.,** Mardinly A.R., Gabel H.W., Bazinet J.E., Couch C.H., Tzeng C.P., Harmin D.A., Greenberg M.E (2014) Npas4 regulates excitatory-inhibitory balance within neural circuits through cell-type-specific gene programs. *Cell* **157**:1216-1229 https://doi.org/10.1016/J.CELL.2014.03.058 | PubMed

52. **Zamboni V.,** Armentano M., Saró G., Ciraolo E., Ghigo A., Germena G., Umbach A., Valnegri P., Passafaro M., Carabelli V., *et al.* (2016) Disruption of ArhGAP15 results in hyperactive Rac1, affects the architecture and function of hippocampal inhibitory neurons and causes cognitive deficits. *Sci. Rep* **6** https://doi.org/10.1038/SREP34877 | PubMed

53. **Ba W.,** Selten M.M., van der Raadt J., van Veen H., Li L.L., Benevento M., Oudakker A.R., Lasabuda R.S.E., Letteboer S.J., Roepman R., *et al.* (2016) ARHGAP12 functions as a developmental brake on excitatory synapse function. *Cell Rep* **14**:1355-1368 https://doi.org/10.1016/J.CELREP.2016.01.037 | PubMed

54. **Nakatani Y.,** Kiyonari H., Kondo T (2019) Ecrg4 deficiency extends the replicative capacity of neural stem cells in a Foxg1-dependent manner. *Development* **146**:dev168120 https://doi.org/10.1242/DEV.168120 | PubMed

55. **Richter M.,** Lalli E., Ruggiero C (2023) Complex and pleiotropic signaling pathways regulated by the secreted protein augurin. *Cell Commun. Signal* **21**:69 https://doi.org/10.1186/S12964-023-01090-8 | PubMed

56. **Chen R.,** Liu Y., Djekidel M.N., Chen W., Bhattacherjee A., Chen Z., Scolnick E., Zhang Y (2022) Cell type-specific mechanism of Setd1a heterozygosity in schizophrenia pathogenesis. *Sci. Adv* **8**:1077 https://doi.org/10.1126/sciadv.abm1077 | PubMed

57. **Mukai J.,** Cannavò E., Crabtree G.W., Sun Z., Diamantopoulou A., Thakur P., Chang C.Y., Cai Y., Lomvardas S., Takata A., *et al.* (2019) Recapitulation and Reversal of Schizophrenia-Related Phenotypes in Setd1a-Deficient Mice. *Neuron* **104**:471-487.e12. https://doi.org/10.1016/j.neuron.2019.09.014 | PubMed

58. **MacDonald M.L.,** Alhassan J., Newman J.T., Richard M., Gu H., Kelly R.M., Sampson A.R., Fish K.N., Penzes P., Wills Z.P., *et al.* (2017) Selective loss of smaller spines in Schizophrenia. *American Journal of Psychiatry* **174**:586-594 https://doi.org/10.1176/APPI.AJP.2017.16070814 | PubMed

59. **Pfeiffer T.,** Poll S., Bancelin S., Angibaud J., Inavalli V.K., Keppler K., Mittag M., Fuhrmann M., Nägerl U.V (2018) Chronic 2P-STED imaging reveals high turnover of dendritic spines in the hippocampus in vivo. *eLife* **7** https://doi.org/10.7554/eLife.34700 | PubMed

60. **Attardo A.,** Fitzgerald J.E., Schnitzer M.J (2015) Impermanence of dendritic spines in live adult CA1 hippocampus. *Nature* **523**:592-596 https://doi.org/10.1038/nature14467 | PubMed

61. **Moriguchi T.,** Takeda S., Iwashita S., Enomoto K., Sawamura T., Koshimizu U., Kondo T (2018) Ecrg4 peptide is the ligand of multiple scavenger receptors. *Sci. Rep* **8** https://doi.org/10.1038/S41598-018-22440-4 | PubMed

62. **Okabe S.,** Kim H.D., Miwa A., Kuriu T., Okado H (1999) Continual remodeling of postsynaptic density and its regulation by synaptic activity. *Nat. Neurosci* **2**:804-811 https://doi.org/10.1038/12175 | PubMed

63. **Shin E.,** Kashiwagi Y., Kuriu T., Iwasaki H., Tanaka T., Koizumi H., Gleeson J.G., Okabe S (2013) Doublecortin-like kinase enhances dendritic remodelling and negatively regulates synapse maturation. *Nat. Commun* **4**:1440 https://doi.org/10.1038/ncomms2443 | PubMed

64. **Ooe N.,** Saito K., Mikami N., Nakatuka I., Kaneko H (2004) Identification of a novel basic helix-loop-helix-PAS factor, NXF, reveals a Sim2 competitive, positive regulatory role in dendritic-cytoskeleton modulator drebrin gene expression. *Mol. Cell. Biol.* **24**:608-616 https://doi.org/10.1128/MCB.24.2.608-616.2004 | PubMed

65. **Ball G.,** Demmerle J., Kaufmann R., Davis I., Dobbie I.M., Schermelleh L (2015) SIMcheck: a toolbox for successful super-resolution structured illumination microscopy. *Sci. Rep* **5**:15915 https://doi.org/10.1038/srep15915 | PubMed

66. **Love M.I.,** Huber W., Anders S (2014) Moderated estimation of fold change and dispersion for RNA-seq data with DESeq2. *Genome Biol* **15** https://doi.org/10.1186/S13059-014-0550-8 | PubMed

Peer reviews

Reviewer #1 (Public review):

Summary:

Kashiwagi et al. undertook a population analysis of dendritic spine nanostructure applied to the objective grouping of 8 mouse models of neuropsychiatric disorders. They report that spine morphology in cultured hippocampal neurons shows a higher similarity among schizophrenia mouse models (compared with autism spectrum disorder (ASD) mouse models) and identify an effect of Ecrg4 (encoding small secretory peptides) on spine dynamics and shape in these models.

Strengths:

The study developed a method for objectively comparing spine properties in primary hippocampal neuron cultures from 8 mouse models of psychiatric disorders at the population level using high-resolution structured illumination microscopy (SIM) imaging. This novel technique identified two distinct groups of mouse models according to the population-level spine properties: those with ASD-related gene mutations and those with schizophrenia-related gene mutations. Functional studies, including gene knockdown and overexpression experiments, identified an effect of Ecrg4 on the spine phenotype of the schizophrenia model mice.

Weaknesses:

The main weakness is that the study is wholly in vitro, using cultured hippocampal neurons. The authors present this as an advantage, however, arguing that spine morphology as measured in a reduced culture system can demonstrate direct effects of gene mutations on

neuronal phenotypes in the absence of indirect influences from nonneuronal cells or specific environments.

https://doi.org/10.7554/eLife.109083.2.sa2

Reviewer #2 (Public review):

Okabe and colleagues build on a super-resolution-based technique they have previously developed in cultured hippocampal neurons, improving the pipeline and using it to analyze spine nanostructure differences across 8 different mouse lines with mutations in autism or schizophrenia (Sz) risk genes/pathways. It is a worthy goal to try to use multiple models to examine potential convergent (or not) phenotypes, and the authors have made a good selection of models. They identify some key differences between the autism versus the Sz risk gene models, primarily that dendritic spines are smaller in Sz models and (mostly) larger in autism risk gene models. They then focus on three models (2 Sz - 22q11.2 deletion, Setd1a; 1 ASD - Nlgn3) for timelapse imaging of spine dynamics, and together with computational modelling provide a mechanistic rationale for the smaller spines in Sz risk models. Bulk RNA sequencing of all 8 model cultures identifies several differentially expressed genes which they go on to test in cultures, finding that ecgr4 is upregulated in several Sz models and its misexpression recapitulates spine dynamics changes seen in the Sz mutants, while knockdown rescues spine dynamics changes in the Sz mutants. Overall, these have the potential to be very interesting findings and useful for the field. My major concerns from the initial manuscript, especially regarding cherry picking and circularity have been addressed with revised analytical approaches. I have some remaining minor comments.

(1) The comparison between two wild-type samples versus wild-type-mutant samples is helpful - I think this could be added to the manuscript.

(2) For results of timelapse imaging - please spell out in the results section the direction of change (lines 270 - 277).

(3) Using linear mixed effect models for statistical analysis is a significant improvement. While a sample size (n) of mice = 3 is not ideal, I think given the multiple different mouse lines used and intensity of analysis, this is probably the best that can be done, although further validation in larger samples eventually is to be hoped for.

(4) The revised text is much improved, but I still think the authors should be upfront somewhere in the text that the schizophrenia-associated genes can only confer biased risk for schizophrenia (and that the clinical phenotype can also include autism). As I said before, I think this is the best we can do and I agree with their choices, but it is important not to overstate the link. The differences they see make it clear that these are still relevant distinctions.

https://doi.org/10.7554/eLife.109083.2.sa1

Author response:

The following is the authors' response to the original reviews.

> ***Public Reviews:***
>
> ***Reviewer #1 (Public review):***
>
> *Summary:*
>
> *Kashiwagi et al. undertook a population analysis of dendritic spine nanostructure applied to the objective grouping of 8 mouse models of neuropsychiatric disorders. They*

> *report that spine morphology in cultured hippocampal neurons shows a higher similarity among schizophrenia mouse models (compared with autism spectrum disorder (ASD) mouse models), and identify an effect of Ecrg4 (encoding small secretory peptides) on spine dynamics and shape in these models.*
>
> *Strengths:*
>
> *The study developed a method for objectively comparing spine properties in primary hippocampal neuron cultures from 8 mouse models of psychiatric disorders at the population level using high-resolution structured illumination microscopy (SIM) imaging. This novel technique identified two distinct groups of mouse models according to the population-level spine properties: those with ASD-related gene mutations and those with schizophreniarelated gene mutations. Functional studies, including gene knockdown and overexpression experiments, identified an effect of Ecrg4 on the spine phenotype of the schizophrenia model mice.*

We thank the reviewer for finding our strategy novel and useful for identifying molecules associated with the spine phenotype in schizophrenia-related mouse models.

> *Weaknesses:*
>
> *The main weakness is that the study is wholly in vitro, using cultured hippocampal neurons. The authors present this as an advantage, however, arguing that spine morphology as measured in a reduced culture system can demonstrate direct effects of gene mutations on neuronal phenotypes in the absence of indirect influences from non-neuronal cells or specific environments.*

We appreciate this reviewer's concern about the limitation of cultured hippocampal neurons in extracting disease-related spine phenotypes. While we fully recognize this limitation, we consider that this *in vitro* system has several advantages that contribute to translational research on mental disorders.

First, our culture system has been shown to support the development of spine morphology similar to that of the hippocampal CA1 excitatory synapse *in vivo*. High-resolution imaging techniques confirmed that the *in vitro* spine structure was highly preserved compared with *in vivo* preparations (Kashiwagi et al., Nature Communications, 2019). The present study used the same culture system and SIM imaging. Therefore, the difference we detected in samples derived from disease models is likely to reflect impairment of molecular mechanisms underlying native structural development *in vivo*.

Second, super-resolution imaging of thousands of spines in tissue preparations under precisely controlled conditions cannot be practically applied using currently available techniques. The advantage of our imaging and analytical pipeline is its reproducibility, which enabled us to compare the spine population data from eight different mouse models without normalization.

Third, a reduced culture system can demonstrate the direct effects of gene mutations on synapse phenotypes, independent of environmental influences. This property is highly advantageous for screening chemical compounds that rescue spine phenotypes. Neuronal firing patterns and receptor functions can also be easily controlled in a culture system. The difference in spine structure between ASD- and schizophrenia-related mouse models is valuable information to establish a drug screening system.

Fourth, establishing an *in vitro* system for evaluating synapse phenotypes could reduce the need for animal experiments. Researchers should be aware of the 3Rs principles. In the future, combined with differentiation techniques for human iPS cells, our *in vitro* approach

will enable the evaluation of disease-related spine phenotypes without the need for animal experiments. The effort to establish a reliable culture system should not be eliminated.

We modified our text to have a balanced discussion on both advantages and disadvantages of the *in vitro* culture system in the study of mental disorder mouse models, as follows:

"Finally, while the spine phenotype identified in the human postmortem brain undoubtedly resulted from complex interactions among genetic background, environmental influences, and regulation by non-neuronal cells, data from pure neuronal cultures are more likely to reflect the direct effects of schizophrenia-related gene mutations on synaptic functions. This property may be advantageous for identifying synaptic molecules that regulate synapse phenotypes in schizophrenia-related mouse models. However, the phenotype observed in the culture system requires confirmation using *in vivo* experiments of mouse models or human tissue samples. Efficient *in vitro* screening combined with reliable *in vivo* evaluation of synapses will facilitate translational research on mental disorders."

> *Another weakness is that CaMKIIαK42R/K42R mutant mice are presented as a schizophrenia model, the authors justifying this by saying that "CaMKII-related signaling pathway disruption has been implicated in the working memory deficits found in schizophrenia patients". Since mutations in CAMK2A cause autosomal dominant intellectual developmental disorder-53 (OMIM 617798) and autosomal recessive intellectual developmental disorder-63 (OMIM 618095), and mice carrying the CAMK2A E183V mutation exhibit ASD-related synaptic and behavioral phenotypes (PMID: 28130356), I think it's stretching credibility to refer to the CaMKIIαK42R/K42R mice as a schizophrenia model.*

We agree with this reviewer that CAMK2A mutations in humans are linked to multiple mental disorders, including developmental disorders, ASD, and schizophrenia. Association of gene mutations with the categories of mental disorders is not straightforward, as the symptoms of these disorders also overlap with each other. For the CaMKIIα K42R/K42R mutant, we considered the following points in its characterization as a model of mental disorder. Analysis of CaMKIIα +/- mice in Dr. Tsuyoshi Miyakawa's lab has provided evidence for the reduced CaMKIIα in schizophrenia-related phenotypes (Yamasaki et al., Mol Brain 2008; Frankland et al., Mol Brain Editorial 2008). It is also known that the CaMKIIα R8H mutation in the kinase domain is linked to schizophrenia (Brown et al., 2021). Both CaMKIIα R8H and CaMKIIα K42R mutations are located in the N-terminal domain and eliminate kinase activity. On the other hand, the representative CaMKIIα E183V mutation identified in ASD patients exhibits unique characteristics, including reduced kinase activity, decreased protein stability and expression levels, and disrupted interactions with ASD-associated proteins such as Shank3 (Stephenson et al., 2017). Importantly, reduced dendritic spines in neurons expressing CaMKIIα E183V is a property opposite to that of the CaMKIIα K42R/K42R mutant, which showed increased spine density (Koeberle et al. 2017).

References related to this discussion.

(1) Yamasaki et al., Mol Brain. 2008 DOI: 10.1186/1756-6606-1-6

(2) Frankland et al. Mol Brain. 2008 DOI: 10.1186/1756-6606-1-5

(3) Stephenson et al., J Neurosci. 2017 DOI: 10.1523/JNEUROSCI.2068-16.2017

(4) Koeberle et al. Sci Rep. 2017 DOI: 10.1038/s41598-017-13728-y

(5) Brown et al., iScience. 2021 DOI: 10.1016/j.isci.2021.103184

We fully agree with the reviewer that different CAMK2A mutations likely cause distinct phenotypes observed in the broad spectrum of mental disorders. In the revised manuscript,

we include a discussion of the relevant literature to categorize this mouse model appropriately.

"CaMKII-related signaling pathway disruption has been implicated in the working memory deficits found in schizophrenia patients [45,46]. CAMK2A mutations in humans are linked to multiple mental disorders, including developmental disorders, ASD, and schizophrenia [47]. The K42R mutation of CAMK2A does not correspond to any known human genetic variant, but the CAMK2A R8H mutation is linked to schizophrenia [48]. Both R8H and K42R mutations in the N-terminal domain of CaMKIIα eliminate kinase activity; these mutations may have a similar impact on human mental disorders."

> *Although the manuscript is largely well written, there are some instances of ambiguous/unspecific language. This extends to the title (Decoding Spine Nanostructure in Mental Disorders Reveals a Schizophrenia-1 Linked Role for Ecrg4), which gives no indication that the work was in vitro on cultured neurons derived from mouse models.*

We appreciate the reviewer for pointing out the lack of information about the experimental system in the title of this manuscript. According to the suggestion of the reviewer, we modified the title as "Decoding spine nanostructure in cultured neurons derived from mouse models of mental disorder reveals a schizophrenia-linked role for Ecrg4".

> ***Reviewer #2 (Public review):***
>
> *Okabe and colleagues build on a super-resolution-based technique that they have previously developed in cultured hippocampal neurons, improving the pipeline and using it to analyze spine nanostructure differences across 8 different mouse lines with mutations in autism or schizophrenia (Sz) risk genes/pathways. It is a worthy goal to try to use multiple models to examine potential convergent (or not) phenotypes, and the authors have made a good selection of models. They identify some key differences between the autism versus the Sz risk gene models, primarily that dendritic spines are smaller in Sz models and (mostly) larger in autism risk gene models. They then focus on three models (2 Sz - 22q11.2 deletion, Setd1a; 1 ASD - Nlgn3) for time-lapse imaging of spine dynamics, and together with computational modelling provide a mechanistic rationale for the smaller spines in Sz risk models. Bulk RNA sequencing of all 8 model cultures identifies several differentially expressed genes, which they go on to test in cultures, finding that ecgr4 is upregulated in several Sz models and its misexpression recapitulates spine dynamics changes seen in the Sz mutants, while knockdown rescues spine dynamics changes in the Sz mutants. Overall, these have the potential to be very interesting findings and useful for the field. However, I do have a number of major concerns.*

We thank the reviewer for evaluating our findings as potentially very interesting and useful.

> *(1) The main finding of spine nanostructure changes is done by carrying out a PCA on various structural parameters, creating spine density plots across PC1 and PC2, and then subtracting the WT density plot from the mutant. Then, spines in the areas with obvious differences only are analyzed, from which they derive the finding that, for example, spine sizes are smaller. However, this seems a circular approach. It is like first identifying where there might be a difference in the data, then only analyzing that part of the data. I welcome input from a statistician, but to me, this is at best unconventional and potentially misleading. I assume the overall means are not different (although this should be included), but could they look at the distribution of sizes and see if these are shifted?*

We appreciate the reviewer's concern regarding our analysis of spine population data. The intention of pre-selecting the areas showing differences between wild-type and mutant was

to make a direct comparison between two subareas (one is enriched with wild-type spines and the other is enriched with mutant spines) and clarify that the spines of schizophreniarelated mouse models were smaller than wild-type spines. Conventional methods of comparing the total spine population using simple size parameters are not useful for this purpose, as shown in Supplementary Figure 2.

To clarify the reviewer's concern, we revised the analysis of the spine population data for both Figure 3 and Figure 8.

Figure 3: We first divided the feature space projected onto PC1 and PC2 into four areas with distinct structural properties: (1) small and short, (2) small and long, (3) large and short, and (4) large and long. Next, we calculated the normalized spine counts in the four areas for both wild-type and mutant spines and obtained the relative ratio (mutant/wild-type) for each area. As we performed three independent SIM imaging experiments (in one, we imaged both wild type and mutant culture dishes prepared from the same pregnant mouse), there are three independent datasets from 8 mouse models.

We found that the spine ratio (mutant/wild-type) only in area 2 (small and long spines) differed significantly between genotypes. This result is shown in Fig. 3 and explained in the text. The spine ratios in areas 1 and 3 did not show a clear relationship to the genotypes, while the ratio in area 4 showed the opposite trend to that in area 2. The opposite trend between areas 2 and 4 indicates enrichment of both small and long spines in schizophrenia-related mouse models, consistent with our previous analysis.

Figure 8: In this analysis, we aimed to evaluate the rescue effect of Ecrg4 shRNA relative to that of control shRNA. If Ecrg4 shRNA is effective, the spine population enriched in the control shRNA condition should be reduced in the Ecrg4 shRNA condition. To confirm this point in the revised manuscript, we first defined areas in the projected PC1-PC2 plane showing either enrichment or depletion of spines in the control shRNA condition (spine numbers increasing or decreasing by more than 3 × SD). We next measured the difference in spine numbers between the control and Ecrg4 shRNA conditions in either enriched or depleted areas. The expectation is that Ecrg4 shRNA treatment reduces the extent of both enrichment and depletion. The effect was significant in both the 22qdel and Setd1a mouse models, as indicated by permutation tests. This analysis was explained in the revised manuscript.

> *(2) Despite extracting 64 parameters describing spine structure, only 5 of these seemed to be used for the PCA. It should be possible to use all parameters and show the same results. More information on PC1 and PC2 would be helpful, given that the rest of the paper is based on these - what features are they related to?*

We thank the reviewer for the advice on providing the rationale for parameter selection in PCA. We divided spines into 160-nm segments along their long axis, and the spine segments were used to calculate the 64 parameters, which include volume of each spine segment (20 segments), convex hull volume of each spine segment (20 segments), and convex hull ratio of each spine segment (20 segments). As most spines are shorter than 0.16 × 20 =3.2 μm, these segment-related parameters contain a large fraction of zero values, which affect the proper calculation of principal components. Therefore, we selected two parameters that reflect the principal structural features (length and volume), together with three other parameters that were mutually independent and also independent from the first two parameters (pairwise correlation coefficients < 0.3). These selection criteria were described in the original manuscript. We also confirmed that PCA using all 64 parameters yields a cross correlation map similar to that shown in Fig. 2B.

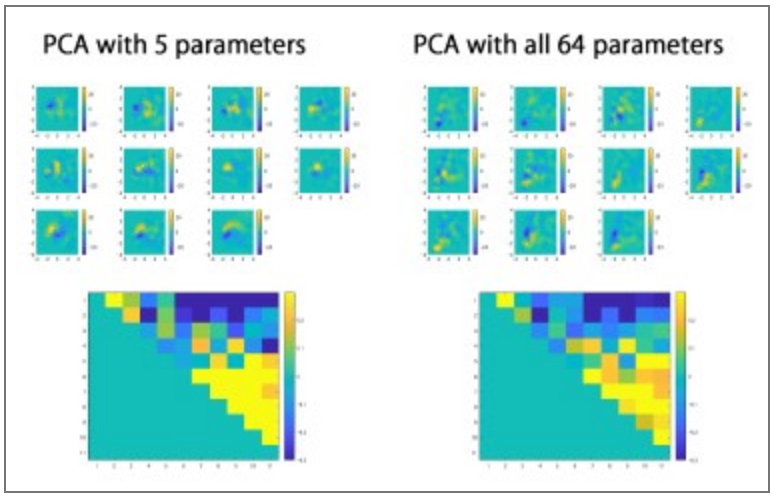

Author response image 1.

We provided additional information in the Materials and Methods section of the revised manuscript.

As described previously, the pattern of four areas with distinct spine structures (1. small and short, 2. small and long, 3. large and short, 4. large and long) supports the idea that the PC1PC2 plane reflects the relationship between spine volume and length (Fig. 3A and B).

> *These specific features could then be analyzed in the full dataset, without doing the cherry picking above.*

We provided the dataset for the relative enrichment of spine counts across four areas of the PC1-PC2 plane in Fig. 3A and B. This analysis provides a comprehensive view of spine population properties related to spine volume and length, without relying on a pre-set region of interest.

> *It would also be helpful to demonstrate whether PC1 and 2 differ across groups - for example, the authors could break their WT data into 2 subsets and repeat the analysis.*

We noticed differences in the pattern of spine distribution across the PC1-PC2 planes in each experiment. The subtraction of the distributional data between wild-type and mutant samples effectively cancels out such differences. In general, the difference between two wild-type samples is smaller than that between wild-type and mutant samples, as shown in Author response image 2.

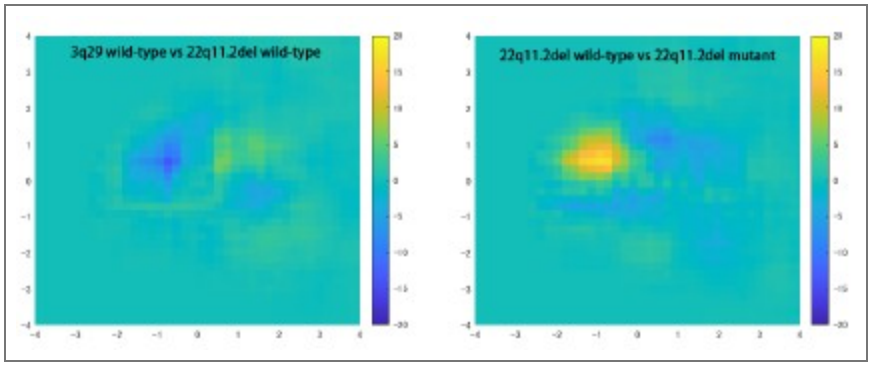

Author response image 2.

We added a description of variation across groups to the revised manuscript.

> *(3) Throughout the paper, the 'n' used for statistical analysis is often spine, which is not appropriate. At a minimum, cell should be used, but ideally a nested mixed model, which would take into account factors like cell, culture, and animal, would be preferable. Also, all of these factors should be listed, with sufficient independent cultures.*

We agree that nested mixed models are more appropriate for evaluating genotype effects in most of our datasets. We confirm that the results of statistical analysis using nested mixed models were consistent with our previous conclusions in most cases.

Figure 3: We performed three independent primary cultures of embryonic hippocampal tissue with genotypes of both wild-type and mutant from the same pregnant mice for each mouse model. In our new Figure 3, each data point represents an independent culture experiment, and group comparisons were performed using one-way ANOVA followed by Tukey's post hoc test. In this analysis, statistical analysis using neurons as units of 'n' is not possible, as the number of spines measured from a single neuron is insufficient to generate the density map shown in Figure 3. The statistical analysis was described in the revised text. The details of experimental conditions related to Figure 3 are provided in Supplementary Table 1.

Figure 5A-C: We analyzed spine turnover rate using a linear mixed-effects model with genotype as a fixed effect and plate, cell, and dendrite as nested random effects. In both 22q deletion model and Setd1a model, there were significant effects of genotype ($F(1,25) = 5.79$, $p = 0.024$ for 22q deletion model and $F(1,22) = 7.33$, $p = 0.013$ for Setd1a model). In contrast, Nlgn3 mutant neurons did not show a significant difference ($F(1,14) = 1.35$, $p = 0.26$). This analysis was described in the revised text.

Figure 5D-F: Spine lifetime was analyzed using a linear mixed-effects model accounting for the hierarchical structure of the data (spines nested within dendrites, cells, and culture plates). The analysis revealed a significant effect of genotype in both 22q deletion mutant and Setd1a mutant (22qdel mutant; $F(1,336) = 5.33$, $p=0.022$, Setd1a mutant; $F(1,282)=6.38$, $p=0.012$). The neurons of both mutants exhibited significantly longer spine lifetimes compared with wild-type neurons (22qdel mutant; ratio = 1.28, 95% CI 1.04–1.58, Setd1a mutant; ratio = 1.35, 95% CI 1.07–1.70). In contrast, Nlg3 mutation did not significantly alter spine lifetime (ratio = 0.86, 95% CI 0.61–1.22; $F(1,220)=0.69$, $p=0.41$). This analysis was described in the revised text.

Figure 5G-I: Spine volume trajectories were analyzed using linear mixed-effects models incorporating nested random effects (spine/dendrite/cell/culture plate) to account for the hierarchical structure of the data. In the 22q deletion model, newly formed spines were significantly smaller than those in wild-type neurons (genotype effect: $p < 0.001$). The spines in Setd1a mutant neurons also displayed significantly smaller volume than those in wild-type neurons ($p < 10^{-7}$). There were also differences in the temporal profiles of spine growth in these two mutants ($p < 0.001$). In contrast, newly formed spines in the Nlgn3 mutant neurons were significantly larger than those in wild-type neurons ($p < 10^{-4}$) with preserved time-course of spine growth. This analysis was described in the revised text.

Figure 5J-L: Similar analyses using linear mixed-effects models incorporating nested random effects (spine within dendrite within cell within culture plate) identified significantly smaller initial spine size in the 22q deletion model ($p < 10^{-6}$), while no significant differences in the initial spine volume were found for Setd1a mutants. The temporal trajectories of spine shrinkage before their loss were also not significantly altered in both 22qdel and Setd1a mutants. The Nlg3 mutant showed a significantly different time-course of spine shrinkage ($p < 0.05$), while the initial spine size was not altered. This analysis was described in the revised text.

Figure 7A overexpression dataset: We analyzed plate-averaged lifetime values using a linear mixed-effects model with treatment as a fixed effect. There exists a significant main effect of treatment ($F(3,8) = 4.59$, $p = 0.038$), with post hoc examination showing a significant increase in lifetime by Ecrg4 overexpression ($\beta = 0.49 \pm 0.16$ SE, $t(8) = 3.16$, $p = 0.013$). Figure 7A shRNA dataset: We also applied a linear mixed-effects model for plate-averaged lifetime values with treatment as a fixed effect. The analysis revealed no significant effect of treatment ($F(2,6) = 0.29$, $p = 0.76$).

The analyses of overexpression and shRNA datasets were described in the revised text.

Figure 8: As in Figure 3, we performed three independent primary cultures of embryonic hippocampal tissue with genotypes of both wild-type and mutant from the same pregnant mice for each mouse model. The culture plates were transfected with either a control shRNA or an Ecrg4 shRNA construct. Each data point represents an independent culture experiment, and the effect of Ecrg4 shRNA relative to that of control shRNA was evaluated using a permutation test. The data analysis was described in the revised text. The details of experimental conditions related to Figure 8 are provided in Supplementary Table 1.

> *(4) The authors should confirm that all mutants are also on the C57BL/6J background, and clarify whether control cultures are from littermates (this would be important). Also, are control versus mutant cultures done simultaneously? There can be significant batch effects with cultures.*

The mutant mice we used in this study are on C57BL/6J or C57BL/6N background. It is known that C57BL/6J or C57BL/6N mice exhibit distinct phenotypes across a range of physiological, biochemical, and behavioral systems. However, it is less likely that our analysis is affected by differences between C57BL/6J and C57BL/6N, as we compared wild-type and mutant littermates on the same genetic background. This experimental design can also reduce the batch effects with different culture preparations. This point was described in the revised text.

> *(5) The spine analysis uses cultures from 18-22 DIV - this is quite a large range. It would be worth checking whether age is a confounder or correlated with any parameters / principal components.*

We described in the method sections that culture samples were processed for imaging at 18-22 DIV. However, all the SIM imaging experiments for eight mutant mouse models were performed on samples fixed at DIV 19. The wide range of imaging experiments (DIV 18-22) includes test samples we used to optimize imaging conditions. In the revised manuscript, we specified the timing of SIM imaging.

> *(6) The computational modelling is interesting, but again, I am concerned about some circularity. Parameter optimization was used to identify the best fit model that replicated the spine turnover rates, so it is somewhat circular to say that this matched the observations when one of these is the turnover rate.*

We appreciate the reviewer's comment on some circularity of the argument. We agree that the turnover rate is already incorporated into the simulation model and is not an appropriate criterion for the evaluation. We modified the text accordingly.

> *It is more convincing for spine density and size, but why not go back and test whether parameter differences are actually seen - for example, it would be possible to extract the probability of nascent spine loss, etc.*

We thank the reviewer for giving this important suggestion. The probability of nascent spine loss is an important parameter, and we initially attempted to estimate it from the original data set. However, the upper limit of our time-lapse imaging is 24 h, which is insufficient to

distinguish stable and nascent spines clearly. The difficulty of extracting all the necessary parameters for spine remodeling is our motivation for starting this computational modelling.

> *More compelling would be to repeat the experiments and see if the model still fits the data. In the interpretation (line 314-318) it is stated that '... reduced spine maturation rate can account for the three key properties of schizophrenia-related spines...', which is interesting if true, but it has just been stated that the probability of spine destabilization is also higher in mutants (line 303) - the authors should test whether if the latter is set to be the same as controls whether all the findings are replicated.*

As suggested by the reviewer, we set the probability of spine destabilization equal across wild-type and mutant models and repeated the simulations. The results indicate that this modification has small effects on spine density (0.61 vs 0.62), spine turnover rate (0.22 vs 0.21), fraction of small spines (0.21 vs 0.20), and mean spine size (0.37 vs 0.36). We described this point in the revised manuscript.

> *(7) No validation for overexpression or knockdown is shown, although it is mentioned in the methods - please include.*

As suggested by the reviewer, we validated overexpression and knockdown. The results are summarized in Supplementary Figure 8.

Supplementary Figure 8A-C shows the immunocytochemistry of anti-Ecrg4, anti-Cip4, and anti-NPAS4 for the confirmation of overexpression of these molecules.

Supplementary Figure 8D-E shows the confirmation of the appropriate size of exogenously expressed Ecrg4, Cip4, and NPAS4 by immunoblotting. (previous Supplementary Figure 10F is now Supplementary Figure 8E).

Supplementary Figure 8F-H indicates the efficient knockdown of exogenously expressed Met-GFP, ARHGAP15-GFP, and Ecrg4-HA by respective shRNA constructs in COS-7 cells. (previous Supplementary Figure 10G is now Supplementary Figure 8H)

> *Also, for the knockdown, a scrambled shRNA control would be preferable.*

We used Stealth RNAi Negative Control Duplexes (Invitrogen) as the shRNA control in this study. To confirm that this RNAi sequence does not affect spine turnover, we performed timelapse imaging of neurons transfected with GFP alone or with GFP and the Stealth RNAi Negative Control. No detectable change in spine turnover was observed (Supplementary Figure 8I), indicating that this RNAi control sequence is suitable for our study.

> *(8) The finding regarding ecgr4 is interesting, but showing that some ecgr4 is expressed at boutons and spines and some in DCVs is not enough evidence to suggest that actively involved in the regulation of synapse formation and maturation (line 356).*

To reveal the active roles of Ecrg4 in spine regulation, we exogenously applied a synthetic Ecrg4 peptide to wild-type neurons and monitored both spine density and turnover rate after Ecrg4 application. The Ecrg4 application increased the spine turnover rate, whereas samples treated with the scrambled peptide did not. This result supports the active role of Ecrg4 in regulating spine turnover. The data were added as Supplementary Figures 9F and G.

> *(9) The same caveats that apply to the analysis also apply to the ecgr4 rescue. In addition, while for 22q the control shRNA mutant vs WT looks vaguely like Figure 2, setd1a looks completely different.*

We thank the reviewer for pointing out the apparent difference in the pattern of spine population data between Figure 2 and Figure 8. We performed SIM analysis using DiI-labeled neurons in Figure 2, whereas the data in Figure 8 are derived from GFP-expressing neurons.

The images of cell-surface labeling and cytoplasmic labeling cannot be analyzed in the same way, as it is necessary to adjust parameters in SIM image processing and PCA-based dimensional reduction. Consequently, the distribution of the spine population projected onto the PC1-PC2 plane differs between DiI-labeled neurons and GFP-expressing neurons. To facilitate the comparison of PCA analysis applied to GFP-expressing neurons, we replaced the weight matrix for GFP-expressing neurons with that previously calculated for the DiIlabeled neurons. This adjustment increased the similarity of the data distributions shown in Figures 2 and 8. The explanation for the different patterns in the spine population map between Figure 2 and Figure 8 was added to the revised text. The related explanation for the data processing was described in the Materials and Methods.

> *And if rescued, surely shRNA in the mutant should now resemble control in WT, so there shouldn't be big differences, but in fact, there are just as many differences as comparing mutant vs wild-type? Plus, for spine features, they only compare mutant rescue with mutant control, but this is not ideal - something more like a 2-way ANOVA is really needed. Maybe input from a statistician might be useful here?*

We appreciate the reviewer's important comment and agree that the analytical approach used in the original manuscript was not optimal. We therefore revised our analysis to examine whether the difference observed between wild-type and mutant neurons was reduced by suppression of Ecrg4 expression.

To this end, we first identified two regions in the PC1–PC2 plane where mutant spines were either enriched or depleted relative to wild-type neurons (Areas A and B). We then counted the number of spines located in Areas A and B in control shRNA-treated mutant neurons (normalized spine counts XA and XB). Next, we quantified spine counts in the same areas using data from Ecrg4-suppressed mutant neurons (normalized spine counts YA and YB). If XA > YA and XB < YB, suppression of Ecrg4 would indicate a shift toward rescue of the phenotype observed in control shRNA-treated mutant neurons. Indeed, the datasets were consistent with this shift in relative spine counts.

To determine whether these differences exceeded those expected from random variation in spine counts, we performed a permutation test. Specifically, spine identities were randomly shuffled between the two conditions while preserving the total number of spines in each dataset. The observed differences were then compared with the distribution obtained from the permuted datasets to assess statistical significance.

We found that all three culture replicates showed statistical significance in both areas A and B for both the 22qdel and Setd1a mutations. This analysis is described in the Result section.

> *(10) Although this is a study entirely focused on spine changes in mouse models for Sz, there is no discussion (or citation) of the various studies that have examined this in the literature. For example, for Setd1a, smaller spines or reduced spine densities have been described in various papers (Mukai et al, Neuron 2019; Chen et al, Sci Adv 2022; Nagahama et al, Cell Rep 2020).*

We appreciate the reviewer's suggestion to include a discussion of schizophrenia-related mouse models. We added more information related to the Setd1a mouse model to the Discussion section.

"Population-level spine properties were more homogeneous in schizophrenia models (those with gene mutations implicated in schizophrenia) than in the other 4 models studied, in part due to a shared tendency for smaller spines. This observation is consistent with previous studies on Setd1a mutant mice, which showed reduced spine width, decreased mushroomtype spines, and lower spine density in the prefrontal cortex [43,56,57]. In contrast to these findings, several previous studies reported reduced numbers of small spines in the postmortem cortical tissues of schizophrenia patients [22,58]. "

> *(11) There is a conceptual problem with the models if being used to differentiate autism risk from Sz risk genes. It is difficult to find good mouse models for Sz, so the choice of 22q11.2del and Setd1a haploinsufficiency is completely reasonable. However, these are both syndromic. 22qdel syndrome involves multiple issues, including hearing loss, delayed development, and learning disabilities, and is associated with autism (20% have autism, as compared to 25% with Sz). Similarly, Setd1a is also strongly associated with autism as well as Sz (and also involves global developmental delay and intellectual disability). While I think this is still the best we can do, and it is reasonable to say that these models show biased risk for these developmental disorders, it definitely can't be used as an explanation for the higher variability seen in the autism risk models.*

We appreciate the reviewer's suggestion for more careful consideration of the interpretation of phenotypes in mouse models, with regard to their relation to clinical phenotypes in human patients. According to the suggestion of the reviewer, we modified the relevant text as follows:

"The nanoscale features of dendritic spines in ASD-associated mouse models were more variable than those in schizophrenia-associated mouse models. This difference may be related to the broader clinical spectrum of ASD, which ranges from mild impairments in social skills to severe intellectual disability. The four ASD-associated mouse models examined in this study, Nlgn3$^{R451C/(y\ or\ R451C)}$, Syngap1$^{+/-}$, POGZ$^{Q1038R/+}$, and 15q11-13$^{dup/+}$, may represent subgroups with different levels of hippocampal dysfunction. Among the four ASD-associated mouse models, 15q11-13$^{dup/+}$ showed population-level spine properties closer to those of the schizophrenia models. To understand this similarity, further analysis of neural circuit changes in both ASD- and schizophrenia-associated mouse models will be necessary. Analysis of the relationships between rare genetic variants and synapse phenotypes in mouse models may contribute to their eventual categorization. This information should be useful to understand the underlying mechanisms of the broader clinical spectrum of ASD."

> *(12) I am not convinced that using dissociated cultures is 'more likely to reflect the direct impact of schizophrenia-related gene mutations on synaptic properties' - first, cultures do have non-neuronal cells, although here glial proliferation was arrested at 2 days, glia will be present with the protocol used (or if not, this needs demonstrating).*

In our culture system, the density of non-neuronal cells is low, and most neurons are not in direct contact with non-neuronal cells. We reported this method in Nat. Neurosci. 1999, where we utilized this culture system to visualize GFP-tagged PSD-95 in neurons using recombinant adenovirus. Because recombinant adenovirus shows higher infection efficiency in glial cells, it was essential for us to establish a culture condition that isolates neurons from glial cells.

> *Second, activity levels will affect spine size, and activity patterns are very abnormal in dissociated cultures, so it is very possible that spine changes may not translate into in vivo scenarios. Overall, it is a weakness that the dissociated culture system has been used, which is not to say that it is not useful, and from a technical and practical perspective, there are good justifications.*

We appreciate the reviewer's comment on the advantages and disadvantages of using an *in vitro*

culture system. This comment aligns with the first reviewer's. We modified our text to have a balanced discussion on the role of the *in vitro* culture system in the study of mental disorder mouse models as follows:

"Finally, while the spine phenotype identified in the human postmortem brain undoubtedly resulted from complex interactions among genetic background, environmental influences, and regulation by non-neuronal cells, data from pure neuronal cultures are more likely to reflect the direct effects of schizophrenia-related gene mutations on synaptic functions. This property may be advantageous for identifying synaptic molecules that regulate synapse phenotypes in schizophrenia-related mouse models. However, the phenotype observed in the culture system requires confirmation using *in vivo* experiments of mouse models or human tissue samples. Efficient *in vitro* screening combined with reliable *in vivo* evaluation of synapses will facilitate translational research on mental disorders."

> *(13) As a minor comment, the spine time-lapse imaging is a strength of the paper. I wonder about the interpretation of Figure 5. For example, the results in Figure 5G and J look as if they may be more that the spines grow to a smaller size and start from a smaller size, rather than necessarily the rate of growth.*

We thank the reviewer for the insightful comment. In the revised manuscript, we analyze the time-lapse data using linear mixed-effects models incorporating nested random effects (spine/dendrite/cell/culture plate). This analysis suggested the difference in the initial size of spines. This point is described in the revised manuscript as follows:

"Schizophrenia-associated mouse models showed higher similarity in spine morphology, driven by reduced size and growth of nascent spines."

"We further compared the initial increase in spine volume between genotypes (Figure 5G-I). Linear mixed-effects models incorporating nested random effects revealed significantly smaller initial spine volumes in both 22q11.2$^{del/+}$ and Setd1a$^{+/-}$ models (genotype effect: $p < 0.001$ for 22q11.2$^{del/+}$ and $p < 10^{-7}$ for Setd1a$^{+/-}$). The spines in both mutants also displayed a significant reduction in spine volume increase ($p < 0.001$). In contrast, newly formed spines in the Nlgn3$^{R451C/(y\ or\ R451C)}$ neurons were significantly larger than those in wild-type neurons ($p < 10^{-4}$) with preserved time-course of spine growth."

We tested whether the initial size difference in spines can be incorporated into the computational simulation. However, due to the large variability in the initial spine size, it was difficult to perform parameter optimization in the model with additional factors. Therefore, we did not further pursue this possibility in this revision. This point is described in the revised text.

> ***Recommendations for the authors:***
>
> ***Reviewer #1 (Recommendations for the authors):***
>
> *The manuscript would be strengthened if the following issues were adequately addressed:*
>
> *(1) It would be helpful to know more about the in/ex vivo dendritic spine phenotype of the mouse models of neuropsychiatric disorders, to allow readers to judge whether and how the in vitro spine phenotype in hippocampal neuronal cultures overlaps with/replicates the spine phenotype within the mouse brain.*

We appreciate this comment, but our currently available data is insufficient to specify the difference between *in vitro* and *in vivo* spine phenotypes. Our previous study, published in Nature. Comm. (2019), provided data showing that the overall distribution of spine size is similar between *in vivo* and *in vitro* conditions in the mouse hippocampus.

> *(2) Although the manuscript is largely well written, there are instances of ambiguous language, particularly when describing the spine phenotypes. For example, we are told that "ASD mouse models showed a tendency of decreasing spine subpopulation with small volumes." This description and other examples should be expressed more clearly.*

Following the reviewer's suggestions, we revised the text to improve clarity. We modified the sentence "ASD mouse models showed a tendency of decreasing spine subpopulation with small volumes" to "ASD-related mouse models showed an opposite spine phenotype."To avoid possible confusion for readers, we have revised several sentences in the text to clarify the intended meaning.

> *Also, I question whether the word "decoding", meaning to convert (a coded message) into intelligible language, is the most appropriate for the title and abstract.*

The original meaning of the word "decoding" is the conversion of a coded message into an intelligible form; however, in this study, we use the term in a broader sense, referring to the extraction of latent population-level properties of dendritic spines from multidimensional structural parameters. We believe this usage is consistent with its common use in neuroscience and systems biology, where "decoding" often refers to inferring underlying biological states or information from complex datasets.

> *(3) The authors should reconsider whether CaMKIIaK42R/K42R mice should be described as a schizophrenia model, when mutations in CAMK2A are known to cause autosomal dominant intellectual developmental disorder-53 (OMIM 617798) and autosomal recessive intellectual developmental disorder-63 (OMIM 618095), and mice carrying the CAMK2A E183V mutation exhibit ASD-related synaptic and behavioral phenotypes (PMID: 28130356).*

We provided a detailed answer to this question in the previous part of the rebuttal.

> *(4) The title doesn't adequately summarise the contents of the manuscript. It should mention mice/mouse models and cultured neurons.*

We also responded to this request in the previous part of the rebuttal.

> ***Reviewer #2 (Recommendations for the authors):***
>
> *(1) Please provide a supplementary table with all DEGs. Also, DEGs are listed if present in 'more than 2' models - does this mean they had to be in 3 or more? Please clarify.*

According to the reviewer's suggestion, we added data on DEGs shared by >2 mouse models in Supplementary Figure 7. We also added Supplementary Tables 2 and 3 for all DEGs. The phrase "in more than 2 models" means "in 3 or 4 models".

> *(2) There are several references to 'schizophrenia mouse models' - it is worth rephrasing this to make clear that these are not mice with schizophrenia.*

We replaced the expression "schizophrenia (or ASD) mouse models" with "schizophrenia (or ASD)-associated mouse models" or similar appropriate wording throughout the manuscript.

> *(3) Line 66: 'a recent...' - 2014 is not really recent.*

We removed the word "recent" from the sentence.

> *(4) Figure S1: The legend says A-D, but they are not on the figure. Also, make clear whether this data is only WT data - it seems to be from disorder models, with 4 colors for each model - please clarify.*

We changed the sentence from "shown as A to D" to "shown as A to C". The datasets in Supplementary Figure 1 are wild-type only. Each graph uses four colors to represent wildtype data from four imaging datasets obtained from different mouse models. Graphs A to C correspond to spine length, surface area, and volume, respectively.

> *(5) Methods, line 680-4: More detail here would be helpful.*

We added more explanation for the generation of subtraction maps.

> *(6) Line 193: Make it clear this is hippocampal in the main text.*

We added "cultures of embryonic hippocampi" to the text.

> *(7) Figure 5, D-F: Make clear that these are transient spines (as per main text)*

We added "Lifetimes of transient spines" to both the main text and figure legend.

> *(8) Figure 6B: More detail is needed; no idea what this is - no axis label. D - also not clear what numbers on the y-axis mean. E - color scale??*

We added details to the figure legend, the axis labels for Figures 6B and 6D, and the color scale for Figure 6E.

> *(9) Supplementary Figure 9 - not clear what matrices are actually showing, nor what the scale refers to - is this the number of shared DEGs? If so, please make it clearer.*

The matrices show the shared DEG numbers, as shown in their titles. The scale indicates DEG numbers. We added the explanation of the color code to the figure legend.

> *(10) Please make clear in the main text that ecgr4 affected the turnover rate. It would be good to measure other parameters as well.*

We added the phrase "a significant increase in spine turnover rate by Ecrg4 overexpression" to the main text.

> *(11) Figure 7: Suggest to label C on images as well, so obvious which is GFP/anti-HA overlay (and respective colors) and which is anti-HA staining.*

We added the labels with respective colors to Figure 7.

> *(12) Ecgr4 is a precursor protein that is cleaved to produce several hormone-like peptides. Where is the HA tag - so which cleavage products will it label? Any antibodies that work in immunocytochem?*

HA tag was attached to the C-terminal domain. We predict that anti-HA binds to four cleavage products (the full-length Ecrg4, Augurin, Argilin, and Δ16). Among several commercially available antibodies, only the SIGMA product could detect cells expressing Ecrg4-HA by immunocytochemistry.

> *(13) Supplementary Figure 10: Synaptosome would be a good addition.*

We isolated the fraction of synaptosomes using Syn-PER™ Synaptic Protein Extraction Reagent in Supplementary Figure 9A. We added this explanation to the Materials and Methods section.

https://doi.org/10.7554/eLife.109083.2.sa0